GDANSK UNIVERSITY OF TECHNOLOGY
Faculty of Electronics,
Telecommunications and Informatics

Marek Zmuda

Analysis and Design of Coupling Structures for High Speed Chip-to-Chip Data Transmission Monitoring

PhD Dissertation

Supervisors:

Associate Professor Stanisław Szczepański
Faculty of Electronics,
Telecommunications and Informatics
Gdansk University of Technology

Professor Sławomir Kozieł
Engineering Optimization & Modeling Center
School of Science and Engineering
Reykjavik University

Gdansk, 2013

I dedicate this work
to my wife Małgosia
and daughter Julka

It is my pleasure to thank many people
who contributed to the creation of this dissertation.

First of all, I would like to show my gratitude to my supervisors:
Associate Professor Stanisław Szczepański and Professor Sławomir Kozieł.
I am grateful for their guidance, valuable remarks, continuous support
and assistance in preparing the final version of the dissertation.
Without many hours of discussions, the support and the warm atmosphere
it would be much harder, if not impossible for me to finish this work.

Herewith I have to thank Professor Michał Mrozowski,
the head of the Microwave and Antenna Engineering Department,
the management of BUMAR Elektronika and RADMOR Company
for providing the equipment which was used for measurements and experiments.

Most of all I would like to thank my wife Małgosia
for her patience and continued support, especially in diffucult moments
and my daughter Julka for her everyday smile
that was for me a source of strength and inspiration.

Marek Zmuda

Contents

Symbols

Symbol	Description
a_i	Power wave propagated into i-th port
A	Amplitude
b	Substrate ground planes spacing
b_i	Power wave propagated out of i-th port
B	Bandwidth
B_c	Channel bandwidth
B_s	Signal bandwidth
c	Speed of light
	$c = 2.9979 \cdot 10^8$ m/s
C	Capacitance
C_e	Coupled stripes even mode total capacitance
C_f	External edge component of strip capacitance
C'_f	Internal edge component of strip capacitance
C_{ga}	Capacitance component between stripes for odd mode in air
C_{gd}	Capacitance component between stripes for odd mode in dielectric
C_{e1}	Coupled strips even mode capacitance for vacuum
C_o	Coupled strips odd mode capacitance
C_{o1}	Coupled strips odd mode capacitance for vacuum
C_p	Central component of strip capacitance
d	Distance
D	Directivity
D	Electric flux density
E	Electric field density
f	Frequency
f_0	Operating frequency
f_c	Cut-off frequency
f_{max}	Maximum frequency
F^{-1}	Inverse Fourier transform
G	Conductance
h	Height
$h(t)$	Impulse response
$H_{eq}(f)$	Equalizer transfer function
$H_{ch}(f)$	Channel transfer function
i	Current

Symbol	Description
I	Isolation
I	Complex amplitude of current wave
I_0	Current amplitude
I_{in}	Input current
j	Imaginary unit
	$j = \sqrt{-1}$
J	Power loss ratio
k_0	Free space propagation constant
l	Length
l_C	Coupler's branch length
l_{max}	Maximal length
L	Inductance
M	Coupling factor
$M_{i,j}$	Coupling factor for i-th and j-th ports
M_L	Transmission line self coupling factor
M_{diff}	Coupling factor for differential signal
n	Number of elements
N_{err}	Number of error bits
N_{bits}	Total number of bits
P	Power
P_i	Power of wave in i-th port
$P(t)$	Clock signal
P_{in}	Input power
P_{out}	Output power
q	Filling factor
R	Resistance
R_c	Transmission rate
R_{cmax}	Maximal transmission rate
R_s	Conductor resistance
R_g	Transmitter output resistance
R_L	Load resistance
s	Complex frequency
s	Distance between two lines
$s(t)$	Time domain signal representation
s_C	Distance between coupler's strips
s_P	Thickness of passivation layer
$\mathbf{S}$	Scattering matrix
$\mathbf{S_{Zx}}$	Scattering matrix normalized to Z_x impedance
S_{ij}	Element of scattering matrix
t	Time
t_i	Time of i-th transition
$\tan\delta$	Loss tangent
t_s	Time of signal sampling
T	Thickness
T_i	Ideal transition timing for i-th transition
T_n	Impulse edge duration
T_s	Impulse duration
v	Voltage
v_s	Sampled voltage

Symbol	Description
V^+	Voltage wave coming to the port
V^-	Voltage wave coming out of the port
V	Complex amplitude of voltage wave
V_0	Voltage amplitude
V_d	Differential voltage
V'_d	Voltage proportional to differential voltage
V_F	Forwarded voltage wave
V_g	Generator step voltage
V_i	Incident voltage
V_s	Voltage step
V_{in}	Input voltage
V_{prop}	Propagation velocity
V_R	Reflected voltage wave
w	Width
w_{eff}	Effective width
w_C	Width of coupler's branch
z	Coordinate position
Δz	Infinitesimal segment of transmission line
Z_0	Characteristic impedance
Z_{0e}	Characteristic impedance for even mode
Z_{0o}	Characteristic impedance for odd mode
Z_{0ei}	Characteristic impedance for even mode of i-th coupling section
Z_{0oi}	Characteristic impedance for odd mode of i-th coupling section
Z_g	Transmitter output impedance
Z_{in}	Input impedance
Z_n	Reference impedance
Z_L	Load impedance
Z_{DUT}	Impedance of device under test
α	Attenuation
α_c	Conductor attenuation
α_d	Dielectric attenuation
α_r	Radiated attenuation
β	Phase constant
Θ	Phase constant
Θ_i	Time offset for i-th transition
η_0	Free space impedance $\eta_0 \simeq 120\pi\ \Omega$
ϕ	Phase constant
$\phi(t)$	Phase offset
Φ_i	Time offset for i-th signal transition
ϵ	Dielectric permittivity
ϵ_0	Vacuum dielectric permittivity $\epsilon_0 = 8.85 \cdot 10^{-12}$ F/m
ϵ_r	Relative dielectric permittivity
ϵ_{eff}	Effective dielectric permittivity
ϵ_{effe}	Effective dielectric permittivity for even mode
ϵ_{effo}	Effective dielectric permittivity for odd mode
γ	Propagation constant
Γ	Reflection coefficient

Symbol	Description
Γ_L	Load reflection coefficient
λ	Wavelength
λ_0	Wavelength for vacuum
μ	Magnetic permeability
μ_0	Vacuum magnetic permeability $\mu_0 = 4\pi \cdot 10^{-7}$ H/m
σ	Conductivity
τ_d	Propagation time
ω	Angular frequency

List of abbreviations

Abbreviation	Description
AC	Alternating Current
ACCI	AC Coupled Interconnection
ADS	Agilent Advanced Design System
AM	Amplitude Modulation
AMP	Amplifier
ARPA	Advanced Research Project Agency Network
ATA	Advanced Technology Attachments
BER	Bit Error Rate
CAD	Computer-Aided Design
CDR	Clock Data Recovery
CLK	Clock signal
CMOS	Complementary MOS
CPU	Central Processor Unit
DARPA	Defense Advanced Research Projects Agency
DC	Direct Current
DCD	Duty Cycle Distortion
DDJ	Data Dependent Jitter
DJ	Deterministic Jitter
DUT	Device Under Test
DVI	Digital Visual Interface
EDA	Electronic Design Automation
EMC	Electromagnetic Compatibility
EMI	Electromagnetic Interference
ESD	Electrostatic Sensitive Device
FEXT	Far End Cross Talk
FM	Frequency Modulation
FWD	Forward
HDMI	High-Definition Multimedia Interface
HFSS	High Frequency Structural Simulator
IBIS	Input/Output Buffer Information Specification
IC	Integrated Circuit
IN	Input
I/O	Input/Output
IP	Internet Protocol
ISI	Inter Symbol Interference

Abbreviation	Description
JDEC	Joint Electron Device Engineering Council
LCM	Low Common Mode
LTE	Long Term Evolution
MCM	Multi-Chip Module
MMIC	Monolithic Microwave Integrated Circuit
MOS	Metal Oxide Semiconductor
NEXT	Near End Cross Talk
OUT	Output
PC	Personal Computer
PCB	Printed Circuit Board
PCIe	Peripheral Component Interconnect Express
PJ	Periodic Jitter
PWM	Pulse Width Modulation
REV	Reverse
RF	Radio Frequency
RFIC	Radio Frequency Integrated Circuit
RJ	Random Jitter
Rx	Receiver
SAS	Serial Attached SCSI
SATA	Serial ATA
SCSI	Small Computer System Interface
SI	Signal Integrity
SNR	Signal to Noise Ratio
SoC	System on Chip
TCP	Transmission Control Protocol
TDR	Time Domain Reflectometry
TDT	Time Domain Transmissometry
TEM	Transverse Electromagnetic
TJ	Total Jitter
Tx	Transmitter
UI	Unit Interval
UMTS	Universal Mobile Telecommunication System
USB	Universal Serial Bus
VCO	Voltage Controlled Oscillator
VNA	Vector Network Analyzer
VLSI	Very Large Scale of Integration
VoD	Video on Demand

Chapter 1

Introduction

1.1 Historical background of high speed data interconnections

In 1939, John Vincent Atanasoff created the first design of a computer machine [1]. This big milestone proved to be extremely important for the development of future data processing systems. The research that led to this invention has been inspired by the needs of industry and military. Two years later, the development tracks of computers and transmission systems coincided. It was the first time when a computer was used to transmit and receive the data over telegraph using the punch cards. From this moment, computers began to be used in other industries [2]. The invention of the transistor by John Bardeen, Walter Houser Brattain, and William Bradford Shockley (Bell Telephone Labs) in 1948 started a new era in the microelectronic circuits development [3, 4]. In 1961, Robert Noyce (Firchild Semiconductor) developed the first integrated circuit (IC). This invention was a quantum leap in miniaturization of electronic devices as amplifiers and microprocessors and allowed to reduce the amount of power consumed by electronic equipment. The race to develop the manufacturing technology for producing IC on a massive scale has began [5, 6]. The technical possibilities given by IC technology allowed designing the devices of increasing complexity, which exchanged more data with surrounding subsystems. In 1965 Gordon Earle Moore observed that the number of transistors on single integrated circuit increases exponentially (doubles approximately every year) [7]. After over a half of a century, Moore's Law is still valid [8]. The age of Very Large Scale Integration (VLSI) circuits began in 1970s caused a change in approach to IC design [9]. The electronic systems became more complex and it quickly became apparent that combining of several chips into larger systems is inevitable [10, 11]. The impact of electrical characteristics of interconnections on the entire system working conditions began to be significant [12, 13, 14, 15, 16].

The amount and speed of data exchanged between systems grew rapidly which greatly accelerated the development of high speed interconnect technology [17, 18, 19, 20, 21]. The IC technology development was accompanied by Computer-Aided Design (CAD) tools [22]. Combining several circuits caused a significant increase of Printed Circuit Board (PCB) complexity. Over the years, the number of copper layers in PCBs systematically increased (from 1 to 16) in general purpose electronic devices like telephones, clocks and computers [23]. This situation triggered the start of research on CAD tools for automated PCB path routing [24, 25, 26]. Today the CAD software became an important piece of market [27, 28, 29, 30, 31, 32, 33, 34]. Due to the growth of transmission rate in interconnections on PCB, the signal integrity issues are more and more important [35]. This situation urges for research and development of the techniques of high speed interconnections to ensure the required bandwidth, electromagnetic compatibility (EMC) and ease of manufacturing with desired transmission quality [36, 37, 38, 39, 40].

We can observe a new trend present in the global society, i.e. the need to be connected. The new style demand to be available every time and everywhere [41]. Additionally, the growth of demands for new broadband services like Video On Demand (VoD), video conferencing, high quality TV, still increase the required bandwidth. This tendency allows us to expect that this situation will not change during the next decades [42]. The amount of devices produced every day reached unprecedented levels [43]. Popularity and accessibility of new multimedia devices like smart phones, tablets and ultrabooks let us to suppose that - in the near future - the importance of manufacturing cost reduction will become crucial. Assuming that the price of a product is at the level acceptable by a customer, potential savings on materials, technology and manufacturing process directly increase the profit for the manufacturer. The mentioned factors indicate that research on high speed interconnections and manufacturing cost optimization still is and will be important over the coming years.

1.2 Parallel to serial transmission migration

The need to develop high speed data systems has been around for many decades [44]. With the increasing amount of data that were exchanged for short and long distances, it was found that increasing the speed of data transmission will reduce the operating costs for many sectors of the economy and thus improve the quality of data transfers. For long distance systems (e.g. transatlantic connections), the only reasonable technique is serial transmission, where the data are sent with single transmission path bit by bit. This approach is justified by economical aspects: only one transmission channel is required to conduct communication between two distant points. There is no need to transmit the clock signal from transmitter to receiver directly. The clock signal CLK is reproduced on the receiver side from the received data stream [45]. It should be noted that one of the main problems of serial transmission is that with the increase of the transmission rate R_c, as well the bandwidth of the signal B_s transmitted by

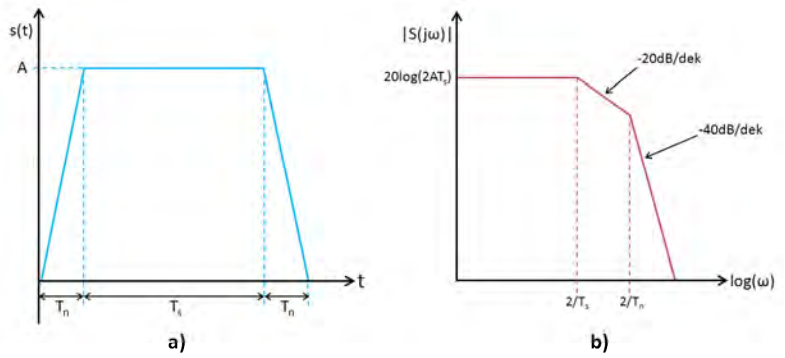

Figure 1.1: The time domain impulse representation $s(t)$ (a) and its spectrum (b) [46]

the medium ($B_s \sim R_c$) inevitably increases. Let us assume that transmission is based on sending the impulses $s(t)$ (of amplitude A, time duration T_s[s] and time of rising edge T_n[s]) from the transmitter to the receiver and one bit of data is represented by one impulse (Fig. 1.1a). The data bit rate for this link is $R_c = 1/(T_s + 2T_n)$[bit/s]. If we assume that only the components of the transmitted signal corresponding to angular frequencies lower than $2/T_n$ are essential for communication (Fig. 1.1b), the considerations conducted in [46] allow us to determine the maximum frequency f_{max}[Hz] which determines the highest element of digital signal spectrum:

$$f_{max} = \frac{1}{\pi T_n} \tag{1.1}$$

With increasing the signal bandwidth, the parasitic phenomena associated with the signal transmission become significant [47]. It is precisely the limit of maximum transmission rate for the assumed Bit Error Rate (BER) for the considered transmission distance.

The situation is different for short distance transmission systems (e.g. internal PC interconnections). For this type of connections, the price of the transmission medium is not critical. That is why for some applications it is reasonable to consider the use the parallel transmission architecture. This solution assumes that the transmission is conducted with n transmission channels. The data in the transmitter is divided into portions and each portion is sent by separate transmission channel. In the receiver, the merge of data from each channel is performed. The most important advantage of this technique is that for the transmission rate R_c the bandwidth of signals transmitted by each transmission channel B_s is lower than for serial transmission ($B_s \sim R_c/n$) (Fig. 1.2). This feature allows us to increase the effective data rate with maintaining low signal bandwidth per single channel. This results in significantly higher quality of transmission than for serial transmission scenario at the same data rate.

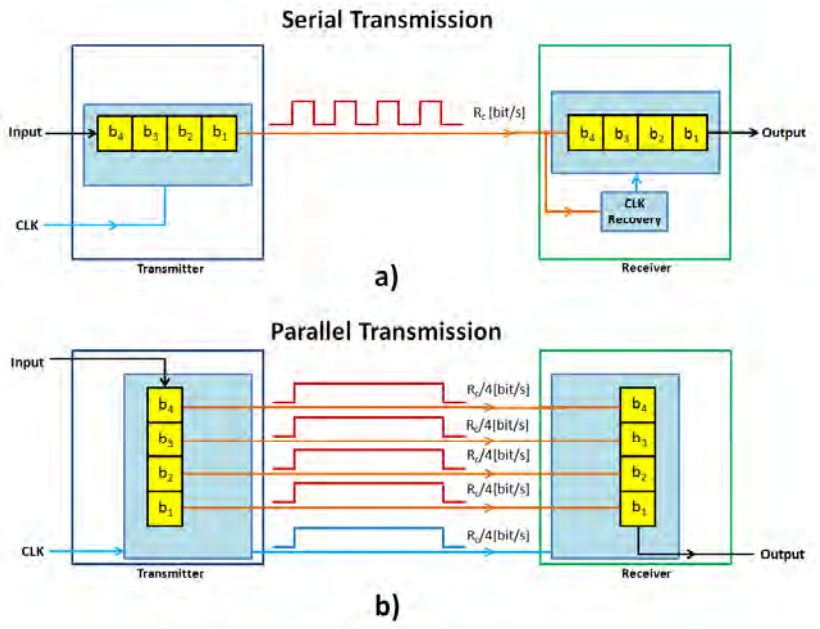

Figure 1.2: The serial (a) and parallel ($n = 4$) (b) organization of data transmission.

The parallel model requires significant investments in terms of transmission synchronization between the channels. This issue becomes significantly more important for relatively high transmission rates when f_{max} for a single channel is close to capabilities of the transmission line. It is necessary to keep the lines for each channel on similar routes and adjust the in lengths (Fig. 1.4). For parallel transmission, the clock signal (CLK) distribution is also required. The knowledge about CLK signal in receiver is necessary to put together symbols received from each channel. In practice, with the increase of the transmission speed, the variations in physical characteristics, such as the line impedance, signal load, and trace, routing causes skew (Fig. 1.3) among the signals in the parallel bus, which has to be accommodated in the design [48]. The skews are different for each transmission channel. With the increasing number of parallel channels or increasing the data rate, the problem of collecting data in the receiver becomes more troublesome. From the economic point of view, the parallel transmission is not optimal either. The parallel IC requires the larger number of I/O pins in the package which significantly increases the cost.

Constantly increasing requirements on transmission rate rather quickly led to a situation when adding subsegment in parallel channels is not sufficient. The limits regarding channel multiplication have been achieved. Additional channels have taken unacceptable amount of space on Printed Circuit Boards (PCB).

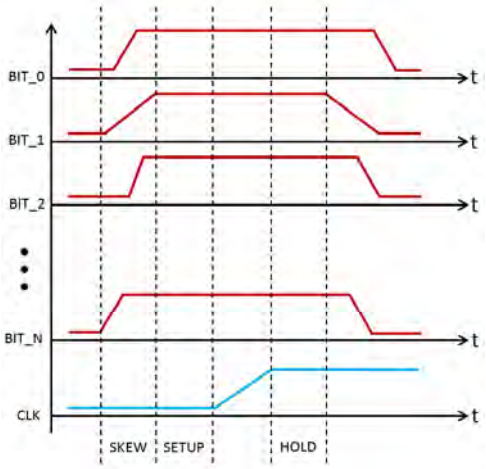

Figure 1.3: The skew across a wide parallel bus [48]

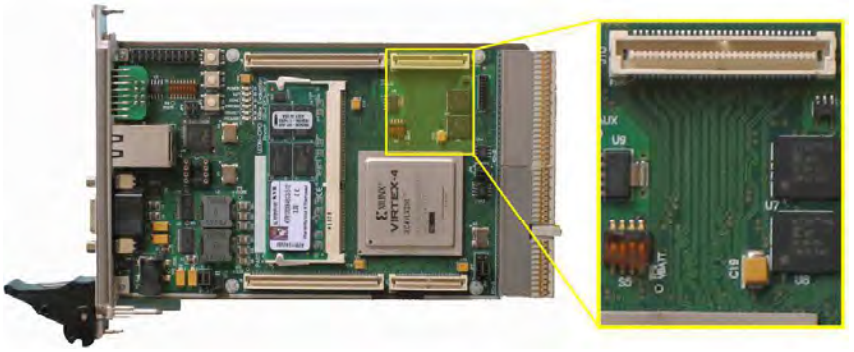

Figure 1.4: High speed interconnection with lines length compensation (Pender Development Board GR-CPCI-XC4V based on Xilinx Virtex 4 FPGA) (*source: www.pender.ch*)

On the other hand differential signaling used in modern serial interconnections has higher immunity to external interferences [49]. Serial buses are significantly more complex because of extended bus management layer. Today's IC technology allows implementing very complex logic circuitry for serial transmission, which is much cheaper than adding more pins for the parallel case. The concept of self-clocking serial transmission allows us to easily resolve all the problems related to ability to work at different data rates. The problem of this type is backward compatibility, which is typical for many general purpose systems (e.g. PCIe) [50]. In the light of before mentioned reasons, the return to serial transmission seems to be necessary and inevitable.

The parallel-to-serial transmission model migration in high speed data interconnections requires a new approach to system debugging and measurement [51]. The monitoring of high speed serial transmission operating in the extremely high frequency bands, which uses data clock recovery technology, puts the new challenges for the measurement systems designers. Additionally, still continuing miniaturization trend joined with product manufacturing cost reduction trend at each step of the product development,which drives the main threads present in the modern industry. For the last several years it has been observed the strong trend of shortening the product development cycle to save money and reduce the time-to-market. This approach forces the development of new system debugging and measurement techniques. For these reasons, taking into account economical and technical aspects, the elimination of unnecessary connectors used only for the system measurements and diagnosis purposes is highly desirable [52]. Additionally, the development of new real-time, easy to use high speed data interconnections on PCB debug techniques can significantly decrease the final product development cost and shorten time to market [53].

1.3 Scope, claims and goals of this work

This work presents the new contact-less probing technique which can be applied for high speed chip to chip serial transmission monitoring on PCB [54, 53]. It was assumed that the monitored interconnection uses differential signaling which is the most popular in modern systems (e.g. PCIe, HDMI, Serial ATA, SAS, Gigabit Ethernet, USB 3.0). The proposed technology eliminates the necessity of using dedicated measurement connectors and adding any test points on PCB. This approach can significantly speed-up the system debug process and shorten the product development cycle process by decreasing the number of prototypes. The described contact-less methodology uses the differential signal coupler [52, 55, 56, 57] which is overlaied on PCB with monitored transmission line. The coupler delivers the probed signal from the transmission line to the next block of the measurement system. The dissertation is based on two thesis:

Thesis 1:

It is possible to realize the proximity coupler which enables decoupling of the differential signal transmitted in the pair of coupled microstrip lines

Thesis 2:

It is possible to use the developed coupling structure to contact-less high speed data transmission monitoring between chips on Printed Circuit Board (PCB).

The main goal of this work is to propose, develop and perform the practical proof of concept of the proximity coupler which enables the high speed serial data transmission monitoring, for chip-to-chip PCB interconnections with differential signaling. The term, data transmission monitoring, is defined as possibility to recover data transmitted in the line under test based on the signal decoupled from the line under the test using the coupler.

As a criterion to define the impact of the probing coupler on the main transmission line under the test, the influence of the coupler on the transmission line scattering parameters was taken. The set of parameters which are considered as a metric is transmission line match, transmission line self coupling and total transmission line loss.

1.4 Chapters outline

The dissertation is written in accordance to the following structure. Chapter 1 presents a high level background of the modern high speed data transmission trends. The importance of serial transmission technology in chip-to-chip high speed PCB interconnections is described. The thesis and the main goals are defined and the scope of the original work is specified.

In Chapter 2, the main technologies associated with the high speed data transmission which are significant from the main working thread point of view were presented, including architectures of the modern serial data transmission systems for chip-to-chip interconnections, the PCB transmission-line-related issues, major measurement and debug technologies which can be applied for high speed serial interconnections development. Additionally, the important phenomena related to high speed transmission on PCB are emphasized. Finally, the most important design, measurement and debug trends are highlighted.

Chapter 3 describes the microstrip coupled line directional coupler technology. The most important parameters, coupler description, design and analysis conventions are presented. This section contains the first theoretical description of differential signal coupler proposed by the author. The proposed concept of the coupler is compared to other architectures of couplers for differential signal decoupling which have been described in the literature. Finally, the most important techniques of coupler parameter's improvement that can be applied for coupled line microstrip couplers are introduced.

Chapter 4 contains simulations and measurements which verify the correctness of the proposed differential signal coupler concept, as well as the proposed design methodology, and suitability of the differential signal coupler for monitored signal probing in high speed data chip-to-chip interconnection without disturbing transmission in the monitored line.

In Chapter 5, the final reworks are formulated, and the features of the proposed solution are summarized. The possible ways of the proposed technology development are highlighted. The original contributions of the dissertation are specified.

Chapter 2

High Speed Serial Data Transmission Technologies

2.1 Modern serial transmission system architecture

The overview of the most important advantages of serial transmission systems was presented in Chapter 1. It was mentioned that obvious benefits such as minimization the area occupied by the interconnection, reduction of the number of pins in the packages, ease of backward compatibility and possibility of communication with higher rate are detached at the expense of increasing the complexity of the transmitter and the receiver. The typical architecture of the modern embedded clock serial system is shown on Fig. 2.1 [58]. The transmitter (Tx) sends the serial data stream. The Clock Data Recovery subsystem (CDR) at the receiver side generates the clock signal for the receiver (Rx) based on the received data stream. The recovered clock signal is used for final data recovery operation which is based on the received signal detection. The connection between the transmitter and the receiver is composed using only one transmission line. This approach causes that signal line routing is much easier than in the systems in which the clock signal is transmitted from transmitter to receiver separately. The compatibility between the phase of the clock signal generated on the receiver side and the current processed data stream is provided by CDR, so that the presented embedded clock serial system is not susceptible to propagation delays. The block diagram of the CDR is shown on Fig. 2.2. The CDR subsystem consist of a phase detector, a loop filter and a Voltage Controlled Oscillator (VCO). The phase of the generated clock signal CLK is compared with the phase of the input data signal in phase detector. The phase detector output signal is taken to the low-pass loop filter and the drives VCO. The quality of the generated clock signal strongly depends on VCO parameters. The parameters of the loop filter has significant impact on dynamic properties of CDR. The characteristic of the loop filter determine how fast the CDR circuit locks at start-up, how wide is the range of immunity to data signal frequency (loop bandwidth)

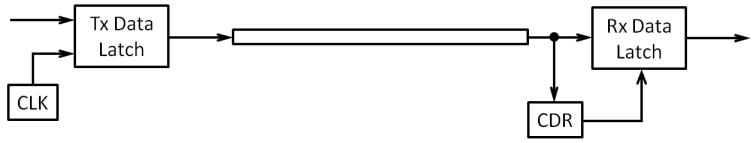

Figure 2.1: Architecture of modern embedded clock serial system [58]

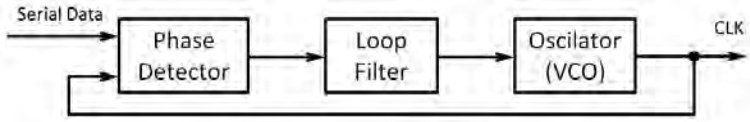

Figure 2.2: Block diagram of an analog Clock Data Recovery (CDR) circuit [58]

and how quickly CDR reacts to the phase deviations. Many modern transmission systems use spread clock to meet the strict Electromagnetic Compatibility (EMC) requirements. The spread clock technology is based on the clock signal modulation with relatively low deviation (about 0.5% of clock frequency). This operation allows for reducing the peak emissions by spreading the emitted energy over a wider frequency band. The CDR circuit is able to track the actual data signal frequency and to recover the clock signal locally instead of the clock frequency deviation on the transmitter side. This requirement is met by using the line coding [58]. The example of a commonly used (PCI Express, Serial ATA, SAS, Gigabit Ethernet, DVI, HDMI, USB 3.0) linear coding is 8b/10b scheme (each 8 bits of the data are transmitted as 10 bit entity which is called symbol).

The embedded clock serial systems has specific requirements for the transmitted signals. The number of symbols which are presented in the transmission line at the high level should be approximately equal to the number of low level symbols from statistical point of view. The transmission of a long sequence of symbols presented in the transmission line at the same level would lead to the situation when the CDR circuit is not able to recover the clock signal correctly.

One of the most important transmission quality metrics from end-to-end point of view is Bit Error Rate (BER). This parameter is defined as quotient of number of errors N_{err} to total number of transfered bits N_{bits} [58] as:

$$BER = \frac{N_{err}}{N_{bits}} \tag{2.1}$$

The PCIe standard for 2.5Gbit/s link requires BER no worse than 10^{-12} [59]. The practical measurements BER is based on sending data from transmitter to receiver and check the correctness of the data in the receiver. A bit error ratio test is only possible if the data content of the signal coming from the device under test is deterministic and known beforehand. The number of bits transfered during the test must be adequate to the expected BER level. Table 2.1 presents the mean time between errors as a function of BER. As we can observe, the BER

BER	1Gbit/s	2.5Gbit/s	5Gbit/s	10Gbit/s	40Gbit/s
10^{-6}	1ms	400us	200us	100us	25us
10^{-7}	10ms	4ms	2ms	1ms	250us
10^{-8}	100ms	40ms	20ms	10ms	2.5ms
10^{-9}	1s	400ms	200ms	100ms	25ms
10^{-10}	10s	4s	2s	1s	250ms
10^{-11}	1.66min	40s	20s	10s	2.5s
10^{-12}	16.67min	6.67min	3.33min	1.67min	25s
10^{-13}	2.78h	1.11h	33.3min	16.67min	4.17min
10^{-14}	1.16d	11.1h	5.56h	2.78h	41.67min
10^{-15}	11.57d	4.63d	2.31d	1.16d	6.94h
10^{-16}	3.86mo	1.54mo	23.15d	11.57d	2.89d
10^{-17}	3.17y	1.27y	7.72mo	3.86mo	28.93d
10^{-18}	31.7y	12.7y	6.34y	3.17y	9.64m

Table 2.1: Mean time between errors as a function of BER [58] (d - days, mo - months, y - years)

measurement in the system with low BER and low transmission rate is a time consumption process.

To evaluate the system performance, an eye diagram can be used which is constructed by slicing the time domain signal waveform into sections that are a small number of symbols in length and overlaying them [60]. The example eye diagram is shown on Fig. 2.3. The unit interval (UI) is defined as the time duration of a single symbol. The width of a typical eye diagram is 2UI. The eye width and height at the receiver side are the key metrics to evaluate the link performance. The eye height determines the link resistance to noises. The width is useful to satisfy the setup and hold requirements. The eye diagram can be used for BER estimation [60]:

$$\mathrm{BER}(t_s, v_s) = \lim_{N\to\infty} \frac{N_{err}(t_s, v_s)}{N_{bits}} \tag{2.2}$$

where (t_s, v_s) represents the relative voltages and times when signal is sampled, N_{err} is the number of the error bits received, N_{bits} is number of the bits transmitted. We can observe that BER depends on the sampling time and the trigger voltage level. The optimal situation is to sample at the central point of eye diagram.

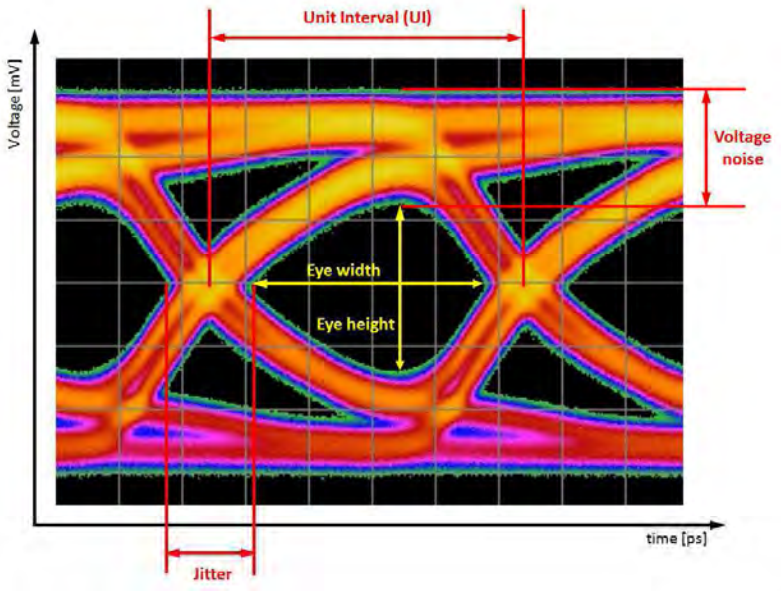

Figure 2.3: Eye diagram

2.2 Transmission lines

The transmission line is a simple electrical structure which is used for communication between electrical components such as microprocessors, memory, chipset, peripheral devices in high speed digital systems. The ideal transmission line does not introduce any signal distortion and attenuation to the guided signal. In practice, the ideal transmission lines does not exist. Moreover, the phenomena which cause signal degradation can not be neglected. Designing a successful bus for high speed data rate transmission requires understanding and taking into account non ideal parameters of transmission lines [60, 61, 62, 63, 64]. The transmission rate which is available with error probability close to zero strongly depends on the transmission channel bandwidth. This maximum available transmission rate can be estimated using the Shannon's equation [65]:

$$R_{cmax} = B_c \cdot \log_2(1 + \mathrm{SNR}) \tag{2.3}$$

where R_{cmax} is the maximal available transmission rate [bit/s], B_c is the channel's bandwidth [Hz] and SNR is the signal-to-noise ratio [dB].

The limits of the usefulness of the classical circuit theory related to transmission lines must be determined by the electrical size of the circuit. The electrical size is understood as a relation between geometrical dimensions of the circuit and the wavelength. The circuit theory is useful for cases in which the wavelength

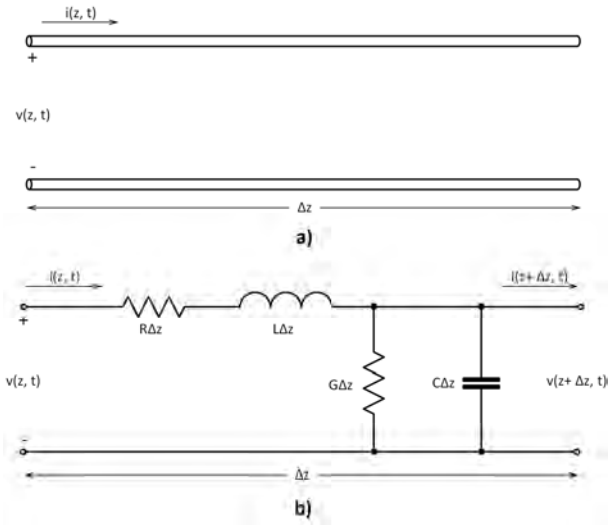

Figure 2.4: Voltage and current definitions (a) and equivalent circuit for an incremental length for transmission line (b) [66]

λ is much larger than circuit dimension ($\lambda > 10 \cdot l_{max}$, where l_{max} is the largest dimension of circuit) [66]. If the wavelength is comparable or smaller than the circuit, the laws of classical circuit theory ceases to be valid and the transmission line theory should be applied. The transmission line theory takes into account that voltages and currents can vary in magnitude and phase over circuit's length. In this approach a short pieces of two wire transmission line Δz can be modeled by lumped-element circuit shown in Fig. 2.4 [66]. The Kirchoff's laws allow us to describe voltages and currents in equivalent circuit (Fig. 2.4b). We can write as follow:

$$v(z,t) - R\Delta z i(z,t) - L\Delta z \frac{\partial i(z,t)}{\partial t} - v(z+\Delta z,t) = 0 \tag{2.4}$$

$$i(z,t) - G\Delta z v(z+\Delta z,t) - C\Delta z \frac{\partial v(z+\Delta z,t)}{\partial t} - i(z+\Delta z,t) = 0 \tag{2.5}$$

After dividing by Δz and assuming that $\Delta z \to 0$ the equations has we obtain telegrapher equations:

$$\frac{\partial v(z,t)}{\partial z} = -Ri(z,t) - L\frac{\partial i(z,t)}{\partial t} \tag{2.6}$$

$$\frac{\partial i(z,t)}{\partial z} = -Gv(z,t) - C\frac{\partial v(z,t)}{\partial t} \tag{2.7}$$

For the sinusoidal steady-state condition, with cosine-based phasor we can simplify equations above:

$$\frac{dV(z)}{dz} = -(R + j\omega L)I(z) \tag{2.8}$$

$$\frac{dI(z)}{dz} = -(G + j\omega C)V(z) \tag{2.9}$$

The equations (2.6) and (2.7) can be solved simultaneously to given wave equations for $V(z)$ and $I(z)$ [66] as:

$$\frac{d^2V(z)}{dz^2} - \gamma^2 V(z) = 0 \tag{2.10}$$

$$\frac{d^2I(z)}{dz^2} - \gamma^2 I(z) = 0 \tag{2.11}$$

where γ is the complex propagation constant which is a function of frequency given as:

$$\gamma = \alpha + j\beta = \sqrt{(R + j\omega L)(G + j\omega C)} \tag{2.12}$$

Traveling wave solution of (2.11) and (2.10) can be found as:

$$V(z) = {V_0}^+ e^{-\gamma z} + {V_0}^- e^{\gamma z} \tag{2.13}$$

$$I(z) = {I_0}^+ e^{-\gamma z} + {I_0}^- e^{\gamma z} \tag{2.14}$$

where the $e^{-\gamma z}$ term represents wave propagation in the $+z$ direction and the $e^{\gamma z}$ term represents wave propagation in the $-z$ direction. Applying the equation(2.8) to the voltage of (2.13) gives the current on the line:

$$I(z) = \frac{\gamma}{R + j\omega L}[{V_0}^+ e^{-\gamma z} - {V_0}^- e^{\gamma z}] \tag{2.15}$$

In general, the telegrapher's equations can be successfully applied to any transmission media which [67]:

- has at least two conductors, insulated from each other,
- has a uniform cross section along the entire length of the structure,

- with a cross-sectional geometry small compared to the wavelength of the signals conveyed,
- a length long compared to the spacing between the conductors

Comparing (2.15) with (2.14) shows that characteristic impedance $Z_0[\Omega]$ can be defined as:

$$Z_0 = \frac{R + j\omega L}{\gamma} = \sqrt{\frac{R + j\omega L}{G + j\omega C}} \tag{2.16}$$

For many practical cases when losses are very small, we can assume that $R = G = 0$ and the propagation constant γ is then given by:

$$\gamma = \alpha + j\beta = j\omega\sqrt{LC}, \tag{2.17}$$

$$\beta = \omega\sqrt{LC}, \qquad \alpha = 0 \tag{2.18}$$

The characteristic impedance $Z_0[\Omega]$ is reduced to:

$$Z_0 = \sqrt{\frac{L}{C}} \tag{2.19}$$

The characteristic impedance for a specific type of line is a function of the conductor size, the conductors spacing, conductor geometry and dielectric permittivity constant ϵ of the insulating material used between the conductors [68]. The dielectric permittivity ϵ for izotrope materials is a scalar and it is defined as the ration of electric flux density D and the electric field density E [69]. The dielectric constant is closely related to the velocity of wave in the material:

$$\epsilon = \frac{1}{{V_{prop}}^2} \tag{2.20}$$

The wavelength λ in transmission line is:

$$\lambda = \frac{2\pi}{\beta} = \frac{2\pi}{\omega\sqrt{LC}} \tag{2.21}$$

Transferring maximum power from the transmitter to the receiver requires impedance matching in the planes transmitter-line and line-receiver (Fig. 2.5). Correct impedance matching is of fundamental importance to reduce the amplitude and phase error and improve signal-to-noise ratio (SNR) of the system. In general, the transmitter output impedance Z_g and transmission line load

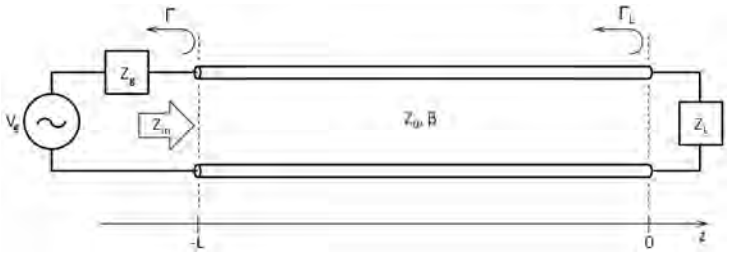

Figure 2.5: Transmission line with load and generator [66]

impedance Z_L (receiver input impedance) can be conjugated. Let us consider lossless transmission line with the transmitter and the receiver ($\gamma = j\beta$). The loaded input impedance $Z_{in}[\Omega]$ can be determined as the load impedance $Z_L[\Omega]$ transformation through transmission line by the distance L as follows [66]:

$$Z_{in} = Z_0 \frac{1 + \Gamma_L e^{-2j\beta L}}{1 - \Gamma_L e^{-2j\beta L}} = Z_0 \frac{Z_L + jZ_0 \tan(\beta L)}{Z_0 + jZ_L \tan(\beta L)} \tag{2.22}$$

where Γ_L is the reflection coefficient of the load:

$$\Gamma_L = \frac{Z_L - Z_0}{Z_L + Z_0} \tag{2.23}$$

The power delivered to the load is:

$$P = \frac{1}{2}\mathrm{Re}\{V_{in} I_{in}^*\} = \frac{1}{2}|V_{in}|^2 \mathrm{Re}\{\frac{1}{Z_{in}}\} = \frac{1}{2}|V_g|^2 |\frac{Z_{in}}{Z_{in} + Z_g}|^2 \mathrm{Re}\{\frac{1}{Z_{in}}\} \tag{2.24}$$

The same discussion can be conducted for transmitter-line matching conditions.

2.3 PCB technology

The printed circuit boards technology allows us to realize connections which transfer signals from integrated circuits (IC) and provide power supply to all components on the board. The complexity of the layout and the number of layers used for a particular design strongly depend on the device complexity, the number of ICs placed on-board and connections between them. The traces are realized on a dielectric substrate. The signals between layers are transfered by vertical metalized holes - vias (Fig. 2.6). The substrate type selection strongly depends on a particular application. The most important criteria to consider during PCB substrate selection are [70]:

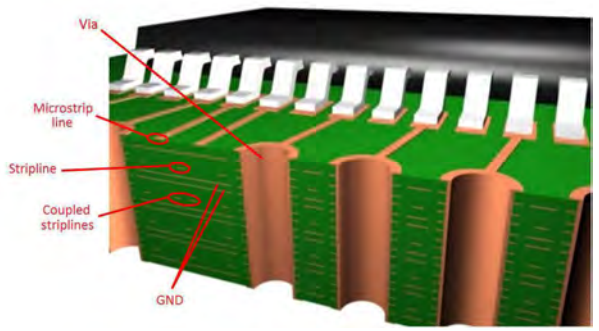

Figure 2.6: The structure of multilayer PCB

- cost
- space limitations
- electrical characteristic
- mechanical characteristic
- availability
- reliability and maintainability
- weight versus flexibility

The most important from types of transmission lines PCB technology point of view are the microstrip, striplines and coupled lines.

The physical construction of the microstrip line is shown on Fig. 2.7a. The wavelength for the microstrip line is given by equation:

$$\lambda = \frac{\lambda_0}{\sqrt{\epsilon_{eff}}} \tag{2.25}$$

where ϵ_{eff} is the effective dielectric permittivity of substrate. The effective permittivity parameter is introduced to take into account the effect of electromagnetic field distribution: partially in the substrate and partially in the air. The effective dielectric constant depends on the substrate dielectric permittivity, physical dimensions of the microstrip line and free space wavelength. The value of ϵ_{eff} is grater than 1 and smaller than the substrate dielectric permittivity ϵ_r. ϵ_{eff} can be calculated as:

$$\epsilon_{eff} = \frac{\epsilon_r + 1}{2} + \frac{\epsilon_r - 1}{2} \frac{1}{\sqrt{1 + 12h/w}} \tag{2.26}$$

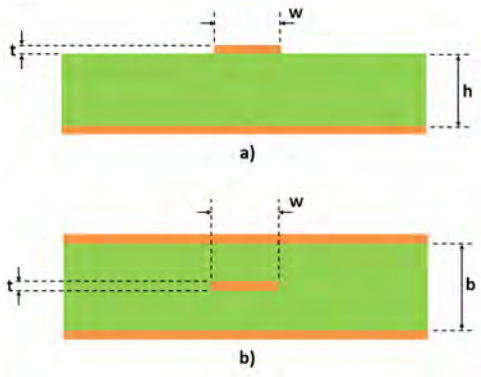

Figure 2.7: Planar transmission lines (a) microstrip line, (b) strip line

The electromagnetic waves guided in the microstrip line are close to but not purely TEM. This is caused by the divided medium: substrate and air. The microstrip is dispersive - the wave velocity varies with frequency. The effect of this relationship is effective dielectric constant and characteristic impedance dependency of frequency. The dispersion in microstrip exists for all frequencies but can be ignored for frequencies lower than f_c [GHz] [71]:

$$f_c = 0.3\sqrt{\frac{Z_0}{h(\epsilon - 1)}} \tag{2.27}$$

where h is a substrate height in [mm]. The complete microstrip line design methodology based on [72, 73] is described in Appendix A.

For most microstrip lines, conductor losses α_c[dB/unit length] significantly exceeded dielectrical losses α_d[dB/unit length]. However, this relationship can not be true for some microwave integrated circuits (silicon or gallium arsenide substrate) [71]. Additionally, for microstrip lines, the radiation loss should be considered. The nature of this phenomena is related to the guided power radiation to air. The radiation losses are pronounced for low dielectric constant substrates ($\epsilon_r < 5$). This type of substrates are commonly used for cost reduction or to avoid extremely low mechanical tolerance. For lines with high dielectric constant substrates, the majority of the electromagnetic field is concentrated in the substrate. For matched microstrip line, radiation loss α_r[dB/unit length] can be calculated as shown in [74]:

$$\alpha_r = 60\left(\frac{2\pi h}{\lambda}\right)^2\left[1.0 - \frac{\epsilon_{eff} - 1}{2\sqrt{\epsilon_{eff}}}\log\left(\frac{\sqrt{\epsilon_{eff}} + 1}{\epsilon_{eff} - 1}\right)\right] \tag{2.28}$$

The most common defects in microstrip manufacturing process are scratches and bumps in the metal surface which can increase conductor losses. Frequently

occurring deviations of the width of the strip result in impedance mismatches in the circuit.

The stripline is chronologically the earliest planar transmission line (Fig. 2.7b). This type of transmission line is composed of the strip conductor centered between two ground planes. The space between strip conductor and ground planes is filled by dielectric or semiconductor. The physical construction assures good electromagnetic shielding. The strip line guides TEM (Transverse Electromagnetic) waves. However, it is necessary to provide vertical symmetry. Failure to comply with this condition can cause the coupling of wave-guide type modes bounded by the ground planes and the side walls. For dielectric and semiconductor medium, the maximum operating frequency f_{max}[GHz] which is determined by the appearance of higher order waveguide mode of H-type can be calculated as follow [71]:

$$f_{max} = \frac{300}{\sqrt{\epsilon_r}[2w + \frac{\pi b}{2}]} \tag{2.29}$$

where ϵ_r is a relative dielectric constant of the substrate medium, w is the width of strip [mm], b is the ground planes spacing [mm].

The wavelength in transmission line can be calculated as below:

$$\lambda = \frac{\lambda_0}{\sqrt{\epsilon_r}} \tag{2.30}$$

where λ_0 is the free-space wavelength. The full microstrip line design methodology based on [75] is described in Appendix B. The characteristic impedance of stripline strongly depends on coefficient center conductor width to substrate thickness and substrate permittivity. This property causes that the precision of manufacturing circuits with low substrate thickness is of almost importance. The conductor losses α_c[dB/unit length] dominate over dielectric losses α_d[dB/unit length] for tanδ less than 0.001 for f=10GHz and less than 0.003 for f=1GHz [71]. The most typical defects in the stripline manufacturing process is vertical symmetry disturbance, change of the width of the central strip and small air gaps surrounding the central strip. These factors can cause coupling of the wave-guide type modes, impedance mismatches and increase of crosstalk.

The coupled microstrips and striplines are often used in practical realizations of PCBs for high speed interconnections (Fig. 2.6). These configurations are commonly used to implement the differential signaling for signal transmission. The transmission through a pair of coupled striplines of microstrip lines is particularly advantageous from EMC point of view: the lower immunity for the interferences, lower level of EM field emission and minimal ground plane current (for ideal case the current in ground plane is zero). A more detailed description of differential signaling is included in Section 2.6. The synthesis methods for coupled microstrip and striplines are described in Appendix C and Appendix D respectively.

Figure 2.8: Two port network

It should be noted that microstrip technology is often used for other applications than interconnections. One of them is microstrip antenna technology [76, 77, 78, 79, 80, 81, 82, 83].

2.4 Transmission line measurements

There are numerous discussions on advantages and disadvantages of the time and frequency domain measurements of high speed data interconnections [84, 85]. Many effects which are specific for lossy transmission lines can be easily measured in the frequency domain. The Vector Network Analyzer (VNA), which operates in frequency domain is able to operate with constant, relatively high SNR in entire frequency range. For Time Domain Reflectometry (TDR) the SNR drops with frequency [86]. On the other hand, it is often believed that the above facts are not relevant when typical transmission lines for digital signals transmission are considered [87]. The argument to make measurements in the time domain is that the final system analysis of interconnection is performed in time domain. Additionally, the time domain measurement could be more advantageous because frequency domain measurements suffers from inaccurate low frequency analysis. This argument for high speed data circuits with which uses 8b10b coding for DC balancing is debatable. The next section presents an overview of VNA and TDR measurements.

2.4.1 Frequency domain measurements

The behavior of linear, time invariant system (Fig. 2.8) can be completely characterized by analyzing the output response of system which is an effect of the known input signal stimuli [66]. The incident and reflected waves are calculated as follow:

$$v(z) = v(z)^{+}e^{-\gamma z} + v(z)^{-}e^{\gamma z} \tag{2.31}$$

$$i(z) = \frac{v(z)^{+}e^{-\gamma z}}{Z_0} - \frac{v(z)^{-}e^{\gamma z}}{Z_0} \tag{2.32}$$

$$P(z) = \frac{[v(z)^+ e^{-\gamma z}]^2}{Z_0} + \frac{[v(z)^- e^{\gamma z}]^2}{Z_0} \tag{2.33}$$

where factors $v(z)^+$, $i(z)^+$ are traveling in the $+z$ direction and factors $v(z)^-$, $i(z)^-$ are traveling in the $-z$ direction, $P(z)$ is a power on the network. The voltage at the port can be calculated by taking $z = 0$. Let us assume that $v(z = 0) = v_i$ and $i(z = 0) = i_i$. For this case v^+ and v^- can be written as:

$$v^+ = \frac{1}{2}(v_i + Ri_i) \tag{2.34}$$

$$v^- = \frac{1}{2}(v_i - Ri_i) \tag{2.35}$$

where R is a port resistance.

The power P_{in} entering the port and P_{out} rejected from the port can be calculated as:

$$P_{in} = \frac{(v^+)^2}{R} \tag{2.36}$$

$$P_{out} = \frac{(v^-)^2}{R} \tag{2.37}$$

Based on the above relations, we can define a new type of terms which specify the power of the wave propagating into i-th port and out of i-th port. They can be described as:

$$a_i = \frac{v(z)^+}{\sqrt{R}} = \sqrt{P_{in}} \tag{2.38}$$

$$b_i = \frac{v(z)^-}{\sqrt{R}} = \sqrt{P_{out}} \tag{2.39}$$

The equations presented above are known as scattering coefficients. Now we can define the S-parameters which describes the behavior of linear, time invariant system:

$$S_{ij} = \frac{b_i}{a_j} = \sqrt{\frac{P_{out,i}}{P_{in,j}}} \tag{2.40}$$

The scattering matrix $\mathbf{S}$ is the most common form of network parameters used in high-speed digital design [60]. In general, the scattering parameters are complex

numbers which includes information about phase shift from i-th and j-th port [66]. The behavior of the network depends on frequency. To characterize behavior of the multi-port circuit in the specified frequency range, it is necessary to prepare **S** parameters matrices for each specific frequencies from the considered frequency range. If the **S** parameters matrices are prepared for a sufficiently fine mesh of frequencies (in comparison to the rate of **S** parameter changes in frequency), the **S** parameters can be interpolated between the two matrices. The impulse response of the circuit can be calculated as follow [60]:

$$h(t) = F^{-1}\mathbf{S}(\omega) \tag{2.41}$$

where $F^{-1}(x)$ is an inverse Fourier transform.

Let us consider the two port network presented in Fig. 2.8 [66]. The behavior of this circuit can be described by four S_{ij} parameters as:

$$\begin{bmatrix} b_1 \\ b_2 \end{bmatrix} = \begin{bmatrix} S_{11} & S_{12} \\ S_{21} & S_{22} \end{bmatrix} \begin{bmatrix} a_1 \\ a_2 \end{bmatrix} \tag{2.42}$$

The parameters S_{11} and S_{22} are referred to as reflection or return loss coefficients. The values of S_{11} and S_{22} describe the network impedance match for the i-th port. The parameters S_{12} and S_{21} determine how much of a signal is passed from port 2 to 1 and from port 1 to 2.

The **S** parameters matrix can be measured using Vector Network Analyzer (VNA). The general block diagram of a VNA is presented in Fig. 2.9. The internal source sweeps harmonic signal which is taken to the DUT input. The generated signal is decoupled and measured as the reference. The signals transfered and rejected from DUT are decoupled by a directional coupler and measured. To realize simultaneous two port measurement, the direction of transmitting and receiving test signal must be switched (FWD and REV modes).

In practice, the measured transmission line, package or element is very often located on the surrounding fixture implemented on a PCB. The VNA ports can not be connected directly to the element which is an object of the measurement. The only option is to connect VNA to available connectors on the fixture. To perform an accurate measurement under such conditions, it is necessary to take into account additional part of the circuit introduced by the unwanted part of the fixture. If we are able to measure **S** parameters of additional structure, we can determine **S** parameters of measured object by using de-embedding technique [60]. Another solution is based on a special type of the VNA calibration with additional part of fixture.

S parameters are referenced to the VNA port impedance, which in most cases is 50Ω. To re-normalize $\mathbf{S_{Z1}}$ parameters from impedance Z_{n1} to $\mathbf{S_{Z2}}$ from Z_{n2}, the equation presented below can be used [60]:

$$Z_{n1}(\mathbf{I} + \mathbf{S_{Z1}})(\mathbf{I} - \mathbf{S_{Z1}})^{-1} = Z_{n2}(\mathbf{I} + \mathbf{S_{Z2}})(\mathbf{I} - \mathbf{S_{Z2}})^{-1} \tag{2.43}$$

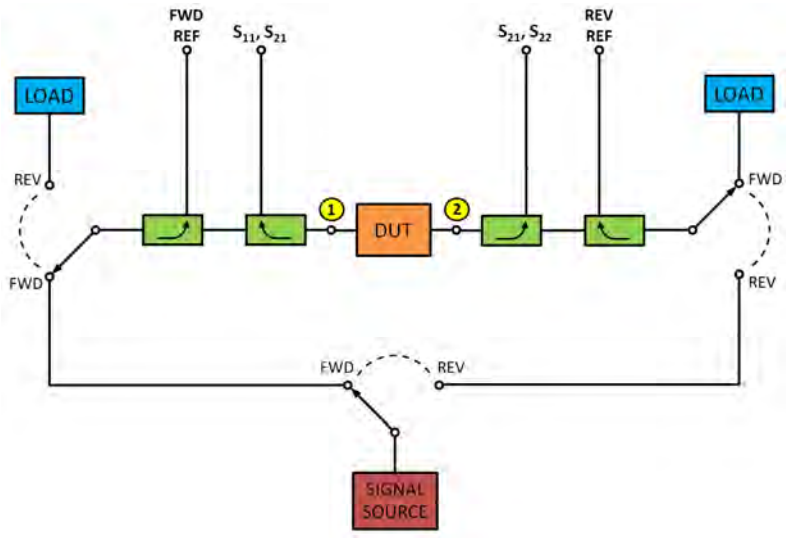

Figure 2.9: 2-Port Vector Network Analyzer (VNA) block diagram

2.4.2 Time Domain Reflectometry (TDR)

Time Domain Reflectometry (TDR) is a measurement technique which is based on observation of the reflected waveform to determine propagation delay and impedance profile along the transmission line. It is possible to estimate the inductances and capacitances presented by the various sections (e.g. via) [60]. The TDR measurement environment is presented on Fig. 2.10a. The voltage step V_g is generated at the input of measurement setup. The step signal is propagated through the $Z_0 = 50\Omega$ measurement cables to DUT. Under the influence of local impedance changes during propagation in DUT, some parts of generated reference signal are reflected. The oscilloscope is used to observe the voltage V_R at point A.

The Time Domain Reflectometry is suitable for locating transmission line faults very accurately and determine the physical nature of the failure by evaluating the impedance changes [58]. This is particularly attractive for diagnosing multilayer PCBs. The measurement bandwidth strongly depends on the test step signal rise time and the oscilloscope bandwidth. The resolution defined as the ability to differentiate the two separated discontinuities equals to the half rise time of the test step signal. TDR measurements are frequently used for package, connectors and multi chip modules modeling. Based on the results of the measurements it is possible to create a SPICE or IBIS model [88]. The guidelines for using TDR for extracting package lumped parameters was standardized by Joint Electron Device Engineering Council (JDEC).

The TDR technique can be used for differential lines. The modification of the measurement method based on the method of test step signal generation.

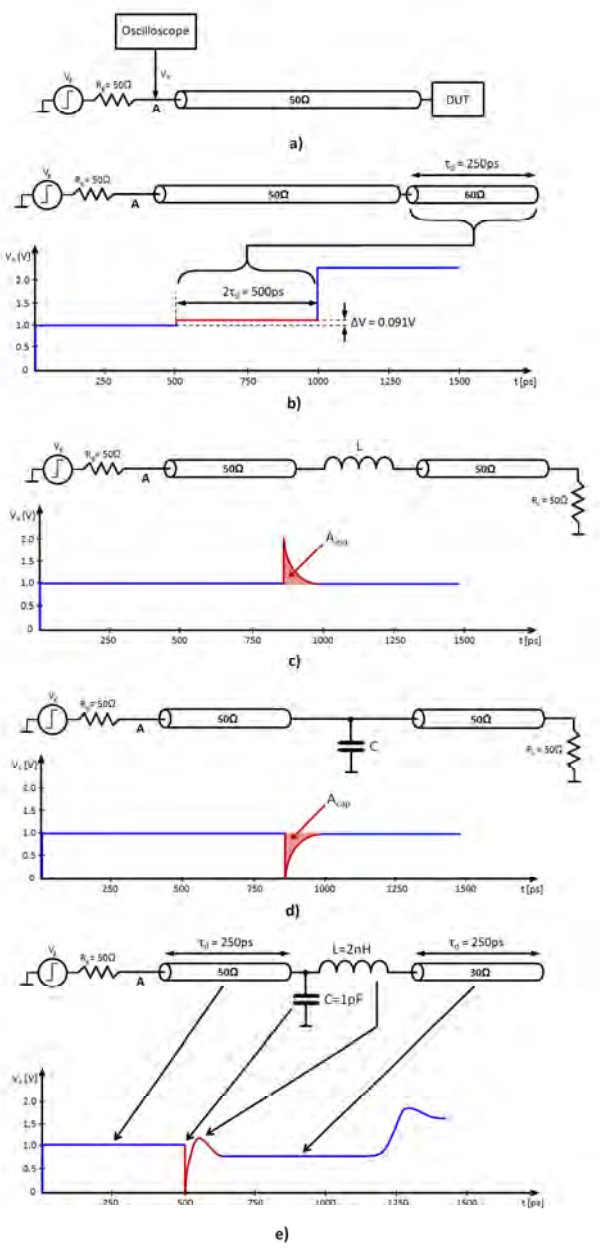

Figure 2.10: Time Domain Reflectometry (TDR). (a) measurement methodology, (b) impedance mismatch, (c) serial inductance, (d) parallel capacitance, (e) combination of elements presented above [60]

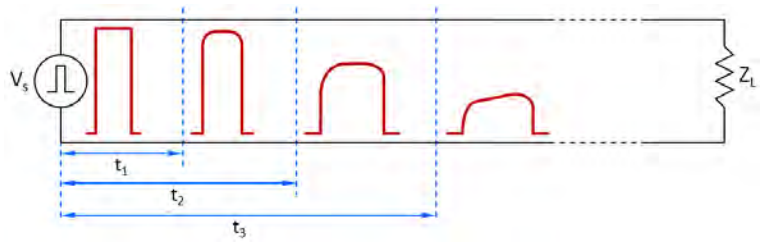

Figure 2.11: Rectangular pulse propagation through non-ideal transmission line

For differential lines, two step signals of the same amplitude and opposite phase are generated for each line. Using differential TDR achieves better accuracy for coupled structures because of more controlled electromagnetic field interaction in comparison with single-ended TDR measurement mode [88].

2.5 Digital signals propagation in transmission lines

The limited bandwidth of the transmission line, interferences from the external sources or impedance mismatch can significantly degrade the serial transmission performance. This section presents an overview of phenomena which take place during high speed transmission through transmission lines on PCB.

Inter Symbol Interferences (ISI)

The Shannon's equation presented in Section 2.2 describes the upper limit for the transmission rate R_{cmax} which can not be exceeded for specific bandwidth B_c and SNR. Unfortunately, the transmission lines used in PCB technology have low-pass characteristics which determine the available bandwidth. The signal components sustain different phase delay and attenuation which depends on the component's frequency [60]. This features of the real, lossy transmission line result in significant distortion the rectangular signal transmission through the line at its far end, as well as its time parameters, which is important for detecting problems on the receiver side (Fig. 2.11). The signal distortions introduced by the transmission lines can be divided into amplitude and phase ones. The transmission line attenuation causes reduction of the amplitude of the transmitted signal. Moreover, the value of attenuation strongly depends on frequency. The phase distortions can be defined as propagation velocity dependence on frequency. Under real working condition, when the string of impulses is transmitted and the information is contained in the amplitude or the slop time, the signal distortion can cause serious detection problems on the receiver side. By extending the time of each pulse, we can observe that adjacent pulses overlap (Fig. 2.12) [87]. The transmission line attenuation and phase characteristic can be easily measured with VNA as S_{12} and S_{21} scattering parameters. When the impulse is propagated through the transmission line, its shape is deformed.

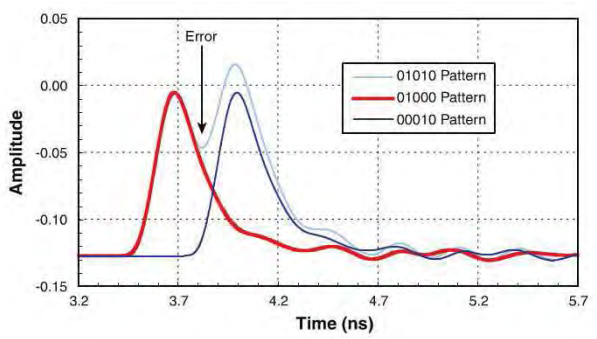

Figure 2.12: Large ISI-Induced Bit Error [87]

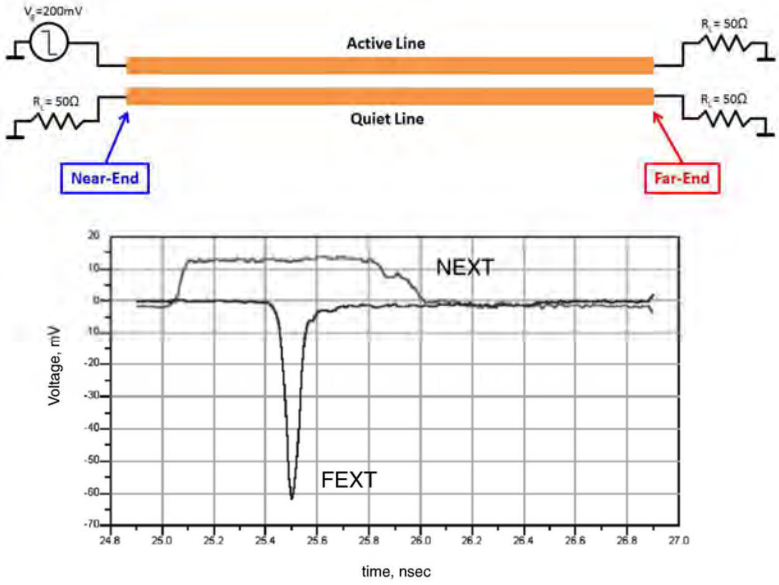

Figure 2.13: Example NEXT and FEXT for 200mV, 50ps rise time signal [86]

Crosstalks

The crosstalk is any phenomenon which causes that the signal transmitted on the channel creates an undesired effect in another channel [89, 90, 91, 92]. In the age of miniaturization, crosstalk plays an important role in the design process and determines the entire system performance. From the circuit theory point of view, crosstalk is caused by mutual inductances and capacitances between conductors [60]. The example single-ended lines (active and quiet) configuration

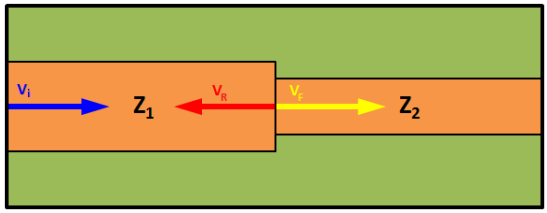

Figure 2.14: Signal reflection caused by impedance discontinuity

is presented on Fig. 2.13. The crosstalk voltage is observed at the two ends of the quiet lines. We can observe that the noise voltage has different pattern on each end. The noise present on the near-end is named Near-End Cross Talk (NEXT) and the noise present on the far end is named Far-End Cross Talk (FEXT). To reduce NEXT, the only way is to increase the physical distance between the traces. FEXT minimization can be achieved in three ways: decreasing the coupling length, increasing the signal rise time and moving the coupled traces apart. The auxiliary parameters which allow determining the specific type of crosstalk (defined as signal decoupled from one line to another from i-th port to j-th port) can be easily measured with VNA in frequency domain as S_{ij} elements. For many years, substantial research effort has been devoted to develop new techniques of crosstalk minimization [93, 94] in order to increase the transmission performance.

Reflections

To assure the optimal propagation conditions in transmission line, the transmission line impedance must be instantaneous through entire length [86]. When the signal transmitted in the transmission line will come across the impedance disturbance, some part of its energy will be reflected from discontinuity and the remaining part of the signal will be forwarded but in a distorted form. The amount of signal which is reflected on impedance discontinuities can be calculated from equation:

$$\Gamma = \frac{V_R}{V_i} = \frac{Z_2 - Z_1}{Z_2 + Z_1} \tag{2.44}$$

$$V_i + V_R = V_F \tag{2.45}$$

where V_R is the reflected voltage, V_i is the incident voltage, Γ is the reflection coefficient, V_F is the voltage which is transfered through interconnection, Z_1 and Z_2 represents the impedances of transmission lines (Fig. 2.14). In practice, the transmission line impedance discontinuities are often introduced by via, corners, branches, pads, gaps and crossovers. The transmission line discontinuities can be easily measured and localized with Time Domain Reflectometry (TDR) technique which is described in Section 2.4.2 and analyzed using simulation [95]. Due to

the reflections in the line caused by the local discontinuity, one often has to deal with reflections at the beginning or at the end of the lines caused by the source or the load mismatch. In general, the impedances are complex values. Apart from resistive components of impedance there can be present capacitive and/or inductive components which can cause some phase shift of reflected signal [86]. It is important to note that during real working conditions, the source and the load impedances can vary due to the current signal level. To avoid this inconvenience, are applied in practical systems, single ended, common mode drivers called low-common mode (LCM) drivers which are able to maintain constant impedance at all times [87].

Jitter

Jitter is a term which describes the timing uncertainties in digital transmission system. Generally, it is defined as instantaneous unintentional deviation in the ideal timing between symbols. In essence, jitter occurs whenever the transition to the next symbol state occurs earlier or later than the end of the exact symbol time interval [58]. The definition of jitter can be specific for a particular technology. As a result, in many cases, the specific definition of jitter and jitter measurement technology is contained in the standard. The phase fluctuations with relatively low frequency (lower than 10Hz) is commonly named wonder. The jitter control is considered to be the most important issue in modern multi-gigabit transmission systems.

The Fig. 2.15 presents the clock oscillation effect named phase noise. It is defined as phase offset $\phi(t)$ which continually shifts the timing of clock signal $p(t)$ [58]:

$$s(t) = p(t + \phi(t)) \tag{2.46}$$

For digital systems, the variability in the signal slope transition time is named phase jitter (Fig. 2.16). The jitter for digital signal can be defined as:

$$t_i = T_i - \Phi_i \tag{2.47}$$

where the t_i is the time of i-th transition, T_i is an ideal transition timing for i-th transition and Φ_i is the time offset for i-th transition.

We can decompose the total jitter (TJ) which is observed during measurement process into specific elements due to the nature of their formation. The most general devision is the random (RJ) and deterministic jitter (DJ). The random jitter is unpredictable (in contrast to deterministic jitter) and is caused by physical noise processes. The spectrum of RJ is flat, without impulses (insteed of deterministic jitter DJ). The periodic jitter (PJ) is a part of deterministic jitter. PJ is repetitive with specific frequency which is caused by the nature of the sources: electromagnetic interference periodic signal sources as oscillators or switching power supplies. The data dependent jitter (DDJ) divided on duty cycle distortion (DCD) and inter-symbol interferences (ISI) is correlated with the data

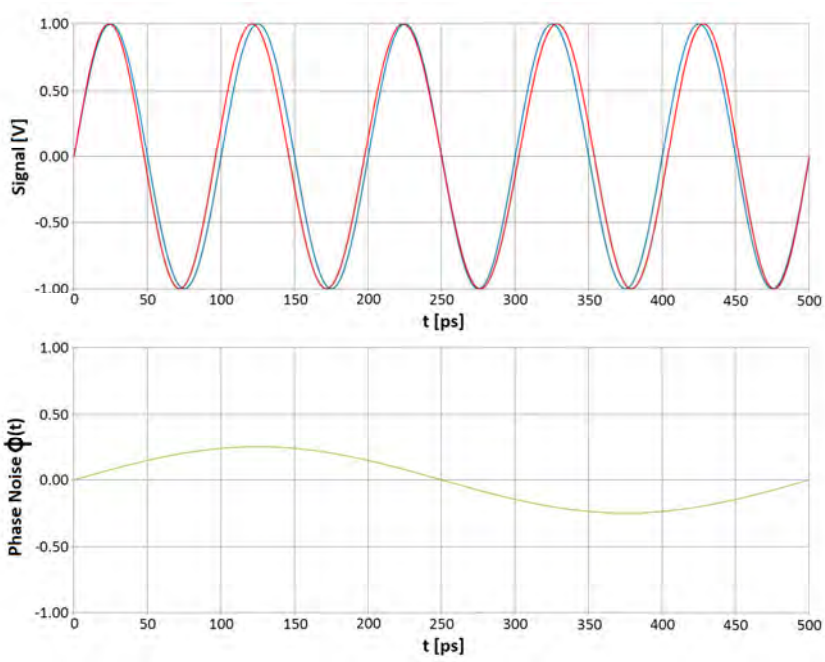

Figure 2.15: The effect of phase noise on an analog signal. Clean 10GHz sinusoidal clock signal (blue), clock signal with phase noise (red), 2GHz sinusoidal phase noise (green)

pattern. In real systems we can observe the total jitter which is a sum of the components described above.

The jitter in transmission systems has three main sources: additive noise, communication channel bandwidth limitations and oscillator phase noise. The noise, by adding to the useful signal, disturbs the point in time when the value of received signal on receiver side exceeds the decision threshold. The limited bandwidth of the transmission line causes attenuation of some components in frequency domain of the received signal. This phenomena results in distortion of the rising and falling edges of the transmitted signal. The phase noise of the crystal oscillator used for the reference clock signal generation causes the fluctuation of rising and falling position in the transmitter.

Signal Integrity

25 years ago, PCB designers considered signal traces as totally passive elements which, as long as they are connected to the correct pins, had no negative impact on circuit performance [96]. In recent years, this simplification has become increasingly inadequate. It is necessary to consider the parasitic elements of traces and interaction between the neighboring traces. Now, the circuit suscep-

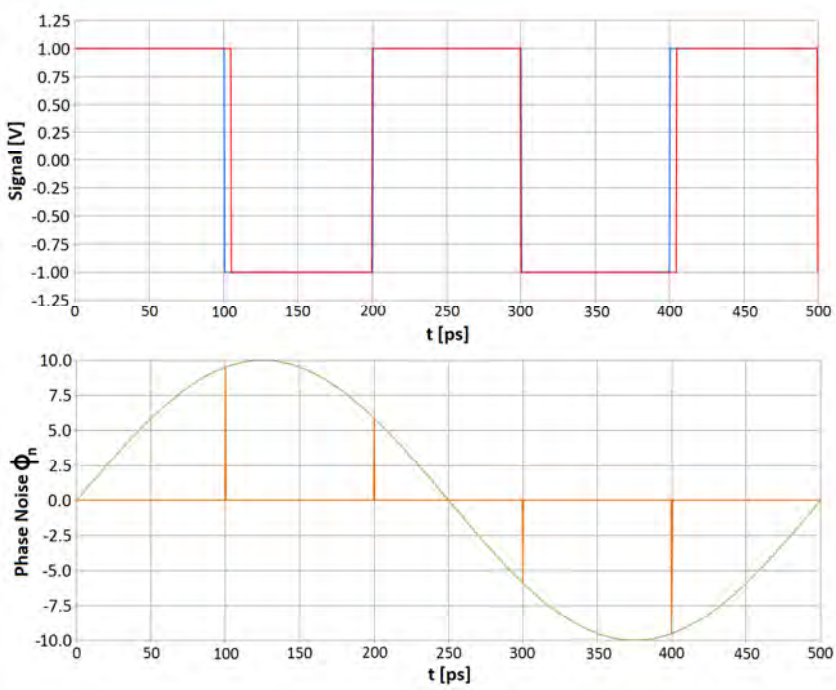

Figure 2.16: The effect of phase jitter on a digital signal. Clean 10GHz rectangular clock signal (blue), clock signal with phase jitter (red), sinusoidal phase jitter(green) sampled at the time of clock slope transition (orange)

tibility to external interferences is of growing significance. The need to analyze the parasitic elements of interconnections, transmitters and receivers, forced IC manufacturers to create models which contains the parasitic elements of the IC I/O ports. In modern devices, many subsystems are running on the same PCB. It is necessary to take into account some general rules which will ensure that coexistence is possible. The most important factor is the correct routing on PCB. Otherwise, it is necessary to consider the parameters of components that are connected at the end of the trace. This task may not be easy for contain complex systems on a chip (SoC). For this purpose, a special modeling standard was created: Input/Output Buffer Information Specification (IBIS). The models of I/O buffers are available for clients without necessity of exposing intellectual property included in the IC [97]. Using IBIS models it is possible to simulate timing and voltage margins dependencies in a credible way.

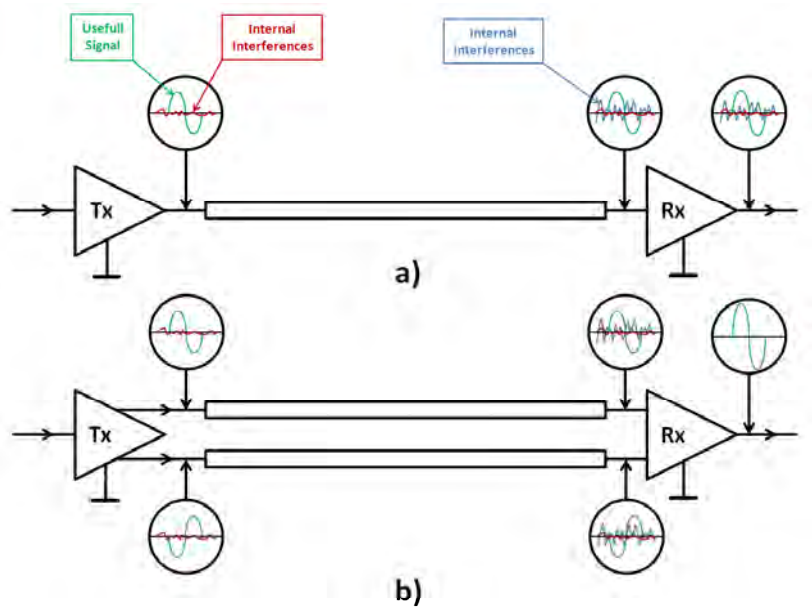

Figure 2.17: Block diagram of system with (a) single-ended and (b) differential signaling

2.6 Classical methods of high speed data transmission improvement

Over the years, some universal techniques which allow eliminating or at least reducing the scale of the phenomena that degrade performance of the high speed interconnections on PCB have been developed. The most important of them are highlighted below.

Single-Ended and Differential Signaling

We can distinguish two methods of signaling in high speed data circuits: single-ended and differential. The single-ended driver has one output port. Similarly, the receiver has one input port. The driver and the receiver use common ground which is used as a reference for the input and the output ports (Fig. 2.17). Using ground as a reference for signaling in modern, complex, multilayer PCBs is confusing. The long and complex shape of traces with multiple vias causes that the ground as the reference potential varies and depends on the position on PCB [98]. The single-ended systems are susceptible to noise. External interferences penetrate into transmission channel and are present in the signal at receiver.

The system with differential signaling has two ports separated from the power and the ground connections. The ground plane current related to differential signal transmission is close to zero (equals zero for the ideal case) which improves the circuit's EMC capabilities and improves detection conditions in the receiver by increasing the SNR. This methodology assures that signal detection does not depend on the ground potential variation due to a position on PCB. Transmitted signal is referenced from the one port to the other. The signal is guided through two coupled lines. Differential signaling can achieve high data rates and low susceptibility to noise. Some internal (e.g. from driver's supply circuit) and external interferences coupled by the transmission line (e.g. radiation from another components on the PCB) are canceled out in the receiver as shown in Fig. 2.17b [87, 60]. The fields radiated by each line are of opposite polarity which significantly reduces the far field electromagnetic radiation. These improvements are redeemed by the necessity of using two transmission lines and using two (instead of one for single-ended configuration) pins in the transmitter and the receiver. The main drowbacks of differential signaling is the need of using additional conducting trace and more complicated implementation than for a single line. The advantages of differential signaling mentioned before become so important that currently differential signaling is the dominant solution in most commercial high speed data systems (as PCIe 3.0, HDMI, SATA 3.0, USB 3.0).

Equalization

The equalization technique is used to improve the received signal quality for the correct clock and data recovery, which results in lowering BER. The technique is based on a concept of high frequency components compensation which are attenuated in channel more that low frequency components the transmitted signal. This behavior is caused by low pass characteristic of the transmission line [60]. As a result, we can observe that eye diagram on the receiver's side is significantly more closed. Due to this, the receiver will not be able to recover the clock and data correctly. There are two types of equalization. The first one is realized on the transmitter side and the other on the receiver side. Both of them use a band-pass filter which realizes the transfer function [60]:

$$H_{eq}(f) = H_{ch}^{-1}(f) \tag{2.48}$$

where $H_{ch}(f)$ is a channel transfer function and $H_{eq}(f)$ is equalizer transfer function. The transmitter technique which is based on amplification of high frequency components can cause EMI and crosstalk problems [99]. Additional disadvantage, which is associated with equalization on the transmitter side, is that no channel characteristic information is present in the transmitter. The receiver must send information to transmitter which is used for equalization tuning. Another option is to attenuate the low frequency components but this operation decreases the total transmitting signal power and SNR in the receiver as well. The received signal is conditioned to obtain minimal BER. The equalization process can be easily tuned in an adaptive way. Modern equalizers are realized either as analog

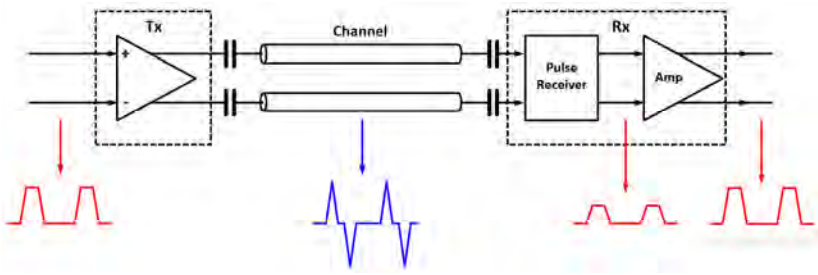

Figure 2.18: AC Coupled Interconnection (ACCI) architecture [103]

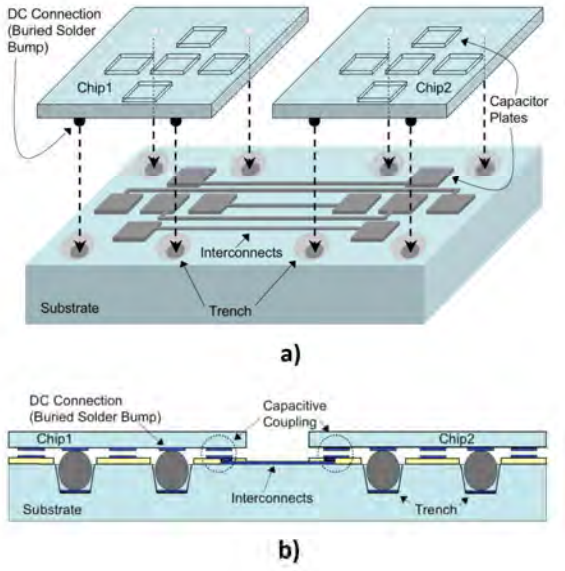

Figure 2.19: ACCI physical structure: (a) 3D view, (b) cross sectional view [104]

(passive or active) or digital systems. The implementation strongly depends on specific application. The equalization techniques are currently a very active field of research [100, 101, 102].

AC Coupled Interconnect (ACCI)

AC Coupled Interconnect (ACCI) is a rapidly growing trend in chip-to-chip, high speed interconnections. The architecture of ACCI interconnection is shown in Fig. 2.18. The concept is based on the assumption that for high speed signal transmission DC connection is not required. This approach is justified because modern high speed circuits uses line coding (like 8b10b) with DC balancing. The

DC components are removed by coupling capacitors. ACCI concept has some significant advantages. One of them is that drivers consume much less power because only dynamic power is used [104]. The coupling capacitors can be implemented as a structure between chips which are connected or chip and PCB (Fig. 2.19). Though this solution it is possible to create miniaturized, reliable and cost saving interconnections which are resistant to thermal fluctuation and mechanical vibrations. It is possible to create chips with significantly more densely connected points than with classical buried bumps technology [105]. The buried solder bumps are needed only in case of DC supply transfer to chip being necessity [103]. The ACCI eliminates the need of using additional decoupling capacitors for ESD protection. By increasing coupling capacitances, the SNR grows, which results in better BER. On the other hand, the increasing capacitance, the ISI grows as well. This relation shows that the coupling capacitance value should be set as a compromise between the optimal SNR and ISI levels [105].

The most significant disadvantage related to ACCI is relative high level of return loss caused by coupling capacitors. This defect can be fixed by implementing coupling coils instead of capacitors. This implementation does not require precise control of coupled elements alignment and spacing, which is very important from practical point of view [106]. Using the coupled coils introduces significant losses that can not be neglected. Additionally, it is required to take into account the parasitic capacitance between coupled inductors. The coupled coils constitute a restriction on the maximal available transmission rate. The practical implementation of inductive coupling interconnection is presented in [107].

The special type of proximity varied high-speed interconnection is presented in [108, 106] (Fig. 2.20). The main concept is based on differential loaded transmission line coupling. The important feature of this solution is that electromagnetic field is in close proximity of the coupling pairs. This results in good signal integrity property and small crosstalk level to the neighboring lines. The new measurement results for 12Gb/s contact less interconnection with coupled circuit power supply was presented [109]. The data signal was transmitted in frequency band 3.4-9.0GHz and power supply was delivered on 13.56MHz. The research on this technology allows to expect that this trend will grow rapidly to meet the demands of still growing transmission rates requirements and a trend to minimize the total device size and cost.

The differential signal coupler configuration presented in Chapter 3 may be used in some cases of ACCI technology implementation. A negligible impact on the transmission line (which was proved by simulations and measurements in Chapter 4) makes the proposed construction attractive to consider ACCI multi slave implementations. Its possible application case is described in Section 4.7.

The AC Coupled Interconnection seems to be the mainstream of researches in the interconnect technology for the next years [105]. The relative interconnection length for chip-to-chip stacking technology is significantly shorter than for classical techniques. This feature allows us to minimize parasitic components introduced by interconnection which has reflection in available channel bandwidth [106, 109].

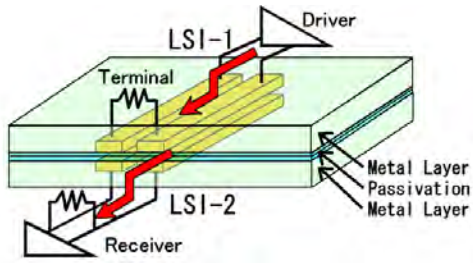

Figure 2.20: Basic idea of the chip-stacking technology utilizing transmission line coupling [106]

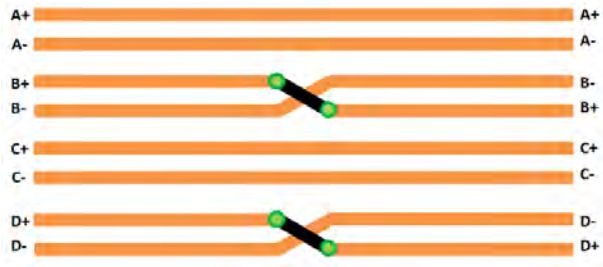

Figure 2.21: FEXT cancellation for differential transmission line

Routing

Some high speed data interconnection improvements can be achieved by suitable tracks routing on the PCB. Beyond the classical tactics, based on keeping safe distances between sensitive circuit area, a designer can take advantage of some sophisticated routing techniques which can results in the signal integrity parameters improvement. One of them is to used crosstalk cancellation in differential transmission lines [110]. The technique basis on interleaving the differential transmission line in the half of its length (Fig. 2.21). Thus, the FEXT which is added to both lines through entire length is equal and can be canceled out in the receiver.

Another technique is to minimize the negative effects of the bends impact on the differential transmission line. The difference of length for each line used for differential signaling causes the phase delay in a single line during signal propagation [111]. The most common cause of the length imbalance are bends. These differences in transmission line length for pair should be compensated to minimize the harmful impact on a link performance. This goal can be achieved by proper routing of coupled transmission lines where the path is optimized to obtain the equal lengths of both lines.

An important issue which should be considered during high speed data circuits PCB is the capacitance of bends in the transmission lines. Those parasitic

elements introduced by the layout can be compensated by additional capacitances [112].

The modern Electronic Design Automation (EDA) tools have implemented special design rules which automatically signalize the incorrect paths which can cause problems with signal integrity [113].

2.7 High speed data links debugging and measurement

The process of debugging the modern high speed data links have never been so important. This situation drives the researchers to looking for new techniques [114, 115, 116]. The prototype and production model signal integrity debug process must result in finding the real root cause. Some problems are visible only during special signal sequences. This cases necessary requires real-time debugging techniques [97]. At extremely high speed transmission rates masking the problem does not bring the desired result. The issues associated with launching the new system results in a situation where more and more designers take their projects in compliance with generally accepted standards and investigate the compliance of design with standards. The widely available tools to verify compatibility with the common industrial standards can significantly speed up the design and the launching process. Considering the measurement environment which is used for reliable analog signals observation, it is required to achieve the sufficient bandwidth of the connectors and the measurement system which should be three times wider than the measured signal bandwidth. The most crucial element of the system is connector which, besides of limited bandwidth, can significantly affect the measured transmission. The modern oscilloscope probe is shown in Fig. 2.22. We can observe that to achieve a good signal fidelity, the significant part of signal conditioning is performed very close to the measurement connector. The location of this debug connector must be considered during the PCB design process. The latest technology uses socket-less probes. This method does not require any connectors on board. The probe has direct contact with PCB which has special measurement pads - access points (Fig. 2.23). Due to the small layout overhead, ease of use in the development and production testing, this technology is the most close in meeting the future needs.

Based on the facts described in Section 2.6 related to the proximity data transmission technologies and the new debug trends presented above (connector-less probing) the author expects the rapid development of new contact-less diagnostic technologies [52, 54] such as decoupling the signal from the transmission lines with proximity couplers [55, 56]. The implementation of the proposed technology for diagnostic and debug purposes may significantly decrease the total device cost (by eliminating dedicated measurement connectors) and simplify the PCB layout design (the measurement pads are omitted). The design methodology of differential signal coupler structure for transmission monitoring is presented in Chapter 3. The simulation results and measurements performed for real chip-to-chip transmission monitoring use cases are presented in Chapter 4.

Figure 2.22: Modern oscilloscope probe. (1) a circuit that controls the probe and communicates with oscilloscope, (2) 50Ω coaxial cable, (3) a probe amplifier which acquires a signal from the device under test to the buffer which drives 50Ω line, (4) attachment for the two small coaxial cables to differential signal measurement, (5) the probe tip which is the point of contact between the circuit under test and the probe [97]

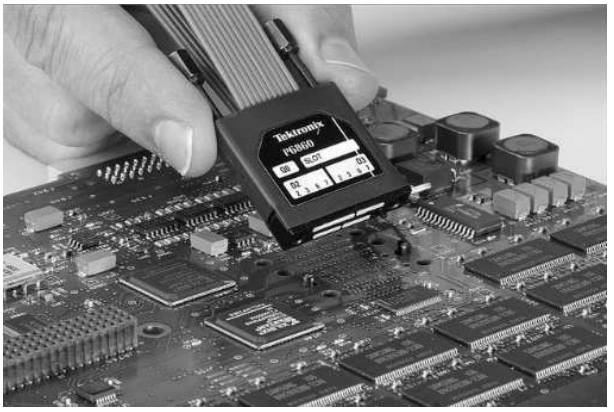

Figure 2.23: Connector-less probe [97]

2.8 Design trends

Based on observation of modern electronic devices market we can assume that the speed of data links will steadily grow. The rapid development of mobile devices market begins to enforce the very strong device's cost optimization trends [58]. In long term perspective we can expect that these facts can change the high speed data circuit architecture, PCB and IC manufacturing process, methods of quality maintenance. The one such revolution in the past was parallel to serial link migration and resignation of signal distribution for clock recovery at the receiver directly from data stream. The new concepts which are considered as potential solutions which could be implemented in high speed data links are researched. One of them is Feed-Forward Clock Correction technique described in [117].

From the physical structures point of view, we can expect a rapid development of capacitive, inductive and transmission line coupled vertical stacking interconnections between high speed chips (e.g. CPU and memory for mobile embedded devices) [108, 107, 104]. The measurement technology is drifting toward socket-less probing, which corresponds to the need for low-cost and reliable testing.

Chapter 3

Analysis and Design of Microstrip Directional Couplers

3.1 Directional coupler

The coupler is a 4-port, passive, reciprocal device used for decoupling defined amount of power from the transmission line to another circuit [66]. A directional coupler is a specific type of device which decouples the power transmitted only in one direction. The first directional coupler based on quarter-wave-long two-wire configuration was designed in 1922 [118]. In 1940s and 1950s the significant progress was achieved in the field of planar coupler development. This area is still an active field of research [119, 120, 121]. For a coupler, each port has a specific name: for the main transmission path Input and Through, Coupled and Isolated (Fig. 3.1). When all ports are matched, the directional coupler can be described by the **S** matrix as follows [66]:

$$\mathbf{S} = \begin{bmatrix} 0 & S_{12} & S_{13} & S_{14} \\ S_{12} & 0 & S_{23} & S_{24} \\ S_{13} & S_{23} & 0 & S_{34} \\ S_{14} & S_{24} & S_{34} & 0 \end{bmatrix} \tag{3.1}$$

For an ideal directional coupler the parameters $S_{14} = S_{23} = 0$ (this condition ensures that there is no decoupled signal in the isolated port). Based on this fact, we can conclude [66, 122]:

$$|S_{12}|^2 + |S_{13}|^2 = 1 \tag{3.2}$$

$$|S_{12}|^2 + |S_{24}|^2 = 1 \tag{3.3}$$

$$|S_{13}|^2 + |S_{34}|^2 = 1 \tag{3.4}$$

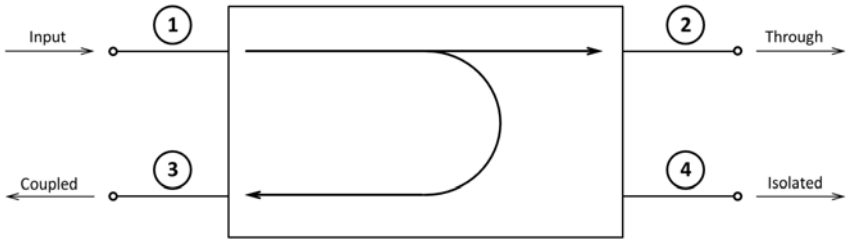

Figure 3.1: Directional coupler

$$|S_{24}|^2 + |S_{34}|^2 = 1 \tag{3.5}$$

The considerations conducted above allow us to state that $|S_{13}| = |S_{24}|$ and $|S_{12}| = |S_{34}|$. To determine the phase relationships let us assume that $S_{12} = S_{34} = \alpha$, $S_{13} = \beta e^{j\theta}$ and $S_{24} = \beta e^{j\phi}$. α and β are real, θ and ϕ are the phase constants. Using the above assumptions, the following relationships can be written [118]:

$$S_{12}^* S_{13} + S_{24}^* S_{34} = 0 \tag{3.6}$$

$$\theta + \phi = \pi \pm 2n\pi \tag{3.7}$$

By considering ϕ and θ relations, we can distinguish two types of directional couplers: symmetrical (for $\theta = \phi = \pi/2$) and anti-symmetrical (for $\theta = \pi$ and $\phi = \pi$) [66]. For symmetrical couplers, the terms with amplitude β are in phase, anti-symmetrical couplers has terms with β amplitude are chosen to be 180° apart. The $\mathbf{S}$ has a form:

$$\mathbf{S} = \begin{bmatrix} 0 & \alpha & j\beta & 0 \\ \alpha & 0 & 0 & j\beta \\ j\beta & 0 & 0 & \alpha \\ 0 & j\beta & \alpha & 0 \end{bmatrix} \qquad \text{when } \theta = \phi = \pi/2 \tag{3.8}$$

$$\mathbf{S} = \begin{bmatrix} 0 & \alpha & \beta & 0 \\ \alpha & 0 & 0 & -\beta \\ \beta & 0 & 0 & \alpha \\ 0 & -\beta & \alpha & 0 \end{bmatrix} \qquad \text{when } \theta = 0 \text{ and } \phi = \pi \tag{3.9}$$

There are three main parameters which describe the real directional coupler: coupling M, directivity D and isolation I [66]. The coupling ratio M in [dB] describes the incident power fed into the input port (1) to the coupled port (3)

when all ports are terminated with match load (Fig. 3.1). The definition of M is:

$$M = 10\log\frac{P_1}{P_3} = -20\log\beta \tag{3.10}$$

where P_i is a power of the wave in the i-th port. The directivity D in [dB] is calculated as the ratio of power at the coupled port (3) and the isolated port (4) with all ports terminated with match load. The definition of D is:

$$D = 10\log\frac{P_3}{P_4} = 20\log\frac{\beta}{|S_{14}|} \tag{3.11}$$

The applications which uses directional couplers usually requires high directivity (35dB or grater) [118]. The isolation I [dB] is the ratio of power at the isolated port (4) to available power at the input port (1). The definition of I is:

$$I = 10\log\frac{P_1}{P_4} = -20\log|S_{14}| \tag{3.12}$$

The isolation equals to a sum of directivity and coupling factor [118] as follow:

$$I = D + M \tag{3.13}$$

The coupler's match is defined as a reflection coefficient of the input (1) or the through (2) port while the other ports are terminated with matched loads [71].

3.1.1 Coupled Line Directional Couplers

The directional coupler consisting of two transmission lines is based on the phenomenon of electromagnetic field interaction between two closely spaced lines. If we assume the TEM type of propagation in the transmission lines, the coupling can be determined by the effective capacitances between the conductors and each conductor and the ground plane and the velocity of propagation in transmission line [66]. If coupling structure is symmetrical, the simplified method of analysis can be used. Let us consider the four-port circuit presented on Fig. 3.2. The relationship between incident and reflected voltage waves can be expressed as:

$$\begin{bmatrix} V_1^- \\ V_2^- \\ V_3^- \\ V_4^- \end{bmatrix} = \begin{bmatrix} S_{11} & S_{12} & S_{13} & S_{14} \\ S_{12} & S_{22} & S_{23} & S_{24} \\ S_{13} & S_{23} & S_{33} & S_{34} \\ S_{14} & S_{24} & S_{34} & S_{44} \end{bmatrix} \begin{bmatrix} \begin{bmatrix} V_1^+ \\ V_2^+ \\ V_3^+ \\ V_4^+ \end{bmatrix} \end{bmatrix} \tag{3.14}$$

where V_i^+ is a voltage wave which comes to i-th port and V_i^- is a voltage wave which comes from the i-th port. Assuming that the circuit under consideration is passive and symmetric, we can observe the following relations [71]:

$$S_{21} = S_{12}, S_{31} = S_{13}, S_{41} = S_{14}, S_{32} = S_{23}, S_{42} = S_{24}, S_{43} = S_{34} \tag{3.15}$$

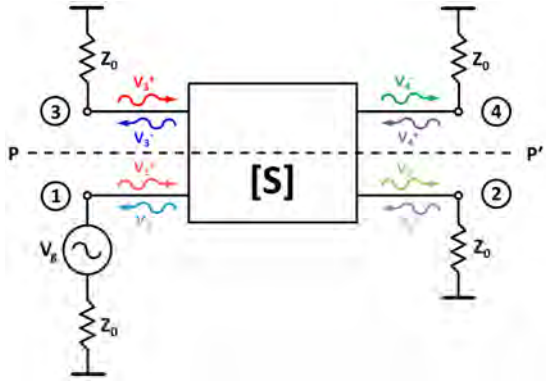

Figure 3.2: A four-port symmetrical network. PP' is a plane of symmetry [118]

$$S_{33} = S_{11}, S_{44} = S_{22}, S_{34} = S_{12}, S_{23} = S_{14} \tag{3.16}$$

Using the relations observed above, we can simplify **S** as follows [118]:

$$\mathbf{S} = \begin{bmatrix} S_{11} & S_{21} & S_{31} & S_{41} \\ S_{21} & S_{22} & S_{41} & S_{42} \\ S_{31} & S_{41} & S_{11} & S_{21} \\ S_{41} & S_{42} & S_{21} & S_{22} \end{bmatrix} = \begin{bmatrix} \mathbf{S_A} & \mathbf{S_B} \\ \mathbf{S_B} & \mathbf{S_A} \end{bmatrix} \tag{3.17}$$

Taking advantage of symmetry, we can analyze the circuit presented above using analysis for even and odd mode excitations (Fig. 3.3) [118]. The scattering matrix for the structure which allows us to analyze the coupler's behavior for any excitation can be determined on the basis of scattering matrices appointed for an even and an odd mode. The circuit analysis for the even mode is presented in Fig. 3.3a. The relationship between the incident and the reflected voltage waves can be expressed:

$$\begin{bmatrix} V_{1e}^- \\ V_{2e}^- \\ V_{1e}^- \\ V_{2e}^- \end{bmatrix} = \begin{bmatrix} \mathbf{S_A} & \mathbf{S_B} \\ \mathbf{S_B} & \mathbf{S_A} \end{bmatrix} \begin{bmatrix} V_{1e}^+ \\ V_{2e}^+ \\ V_{1e}^+ \\ V_{2e}^+ \end{bmatrix} \tag{3.18}$$

which can be simplified as:

$$\begin{bmatrix} V_{1e}^- \\ V_{2e}^- \end{bmatrix} = (\mathbf{S_A} + \mathbf{S_B}) \begin{bmatrix} V_{1e}^+ \\ V_{2e}^+ \end{bmatrix} \tag{3.19}$$

Similar considerations can be carried out for the odd mode excitation (Fig. 3.3b). The relationship between incident and reflected voltage waves for each port can be expressed as:

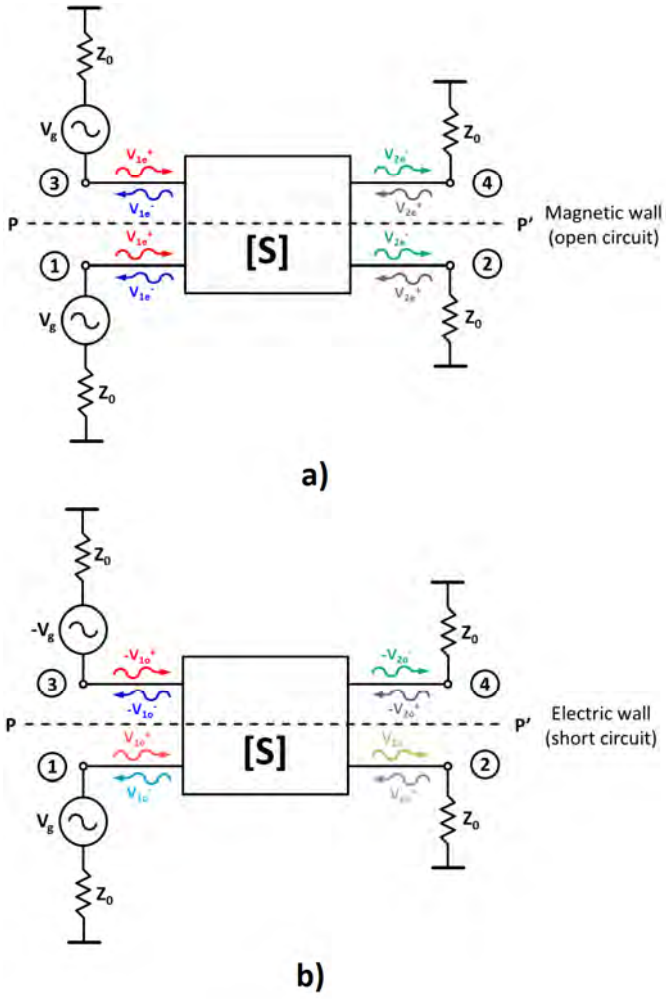

Figure 3.3: A four-port symmetrical network excited by (a) even-mode, (b) odd-mode sources [118]

$$\begin{bmatrix} V_{1o}^{-} \\ V_{2o}^{-} \\ -V_{1o}^{-} \\ -V_{2o}^{-} \end{bmatrix} = \begin{bmatrix} \mathbf{S_A} & \mathbf{S_B} \\ \mathbf{S_B} & \mathbf{S_A} \end{bmatrix} \begin{bmatrix} V_{1o}^{+} \\ V_{2o}^{+} \\ -V_{1o}^{+} \\ -V_{2o}^{+} \end{bmatrix} \tag{3.20}$$

Simplifying we obtain:

$$\begin{bmatrix} V_{1o}^{-} \\ V_{2o}^{-} \end{bmatrix} = (\mathbf{S_A} - \mathbf{S_B}) \begin{bmatrix} V_{1o}^{+} \\ V_{2o}^{+} \end{bmatrix} \tag{3.21}$$

The equation (3.19) can be written as:

$$\begin{bmatrix} V_{1e}^{-} \\ V_{2e}^{-} \end{bmatrix} = \mathbf{S_e} \begin{bmatrix} V_{1e}^{+} \\ V_{2e}^{+} \end{bmatrix} \tag{3.22}$$

where

$$\mathbf{S_e} = \mathbf{S_A} + \mathbf{S_B} \tag{3.23}$$

Similarly, the equation (3.21) can be written as:

$$\begin{bmatrix} V_{1o}^{-} \\ V_{2o}^{-} \end{bmatrix} = \mathbf{S_o} \begin{bmatrix} V_{1o}^{+} \\ V_{2o}^{+} \end{bmatrix} \tag{3.24}$$

where

$$\mathbf{S_o} = \mathbf{S_A} - \mathbf{S_B} \tag{3.25}$$

From (3.23) and (3.25) we can obtain [118]:

$$\mathbf{S_A} = \frac{\mathbf{S_e} + \mathbf{S_o}}{2} \tag{3.26}$$

$$\mathbf{S_B} = \frac{\mathbf{S_e} - \mathbf{S_o}}{2} \tag{3.27}$$

An example of the even and the odd mode excitations for microstrip coupled lines with equivalent inter-strip capacitances model is presented in Fig. 3.4. For even mode, the field is distributed symmetrically and there is no current flow between the stripes. The symmetry allows us to introduce a magnetic wall (Fig. 3.4a). The capacitance of either line to ground for even mode excitation is [66]:

$$C_e = C_{11} = C_{22} \tag{3.28}$$

Assuming that both strips have the same geometrical dimensions, we can calculate the characteristic impedance of the microstrip coupled lines for the even mode excitation:

$$Z_{0e} = \sqrt{\frac{L}{C_e}} = \frac{\sqrt{LC_e}}{C_e} = \frac{1}{V_{prop}C_e} \tag{3.29}$$

where V_{prop} is a velocity of wave propagation in the line. Similarly, for the odd mode excitation, the electrical wall can be introduced (Fig. 3.4b). Using this

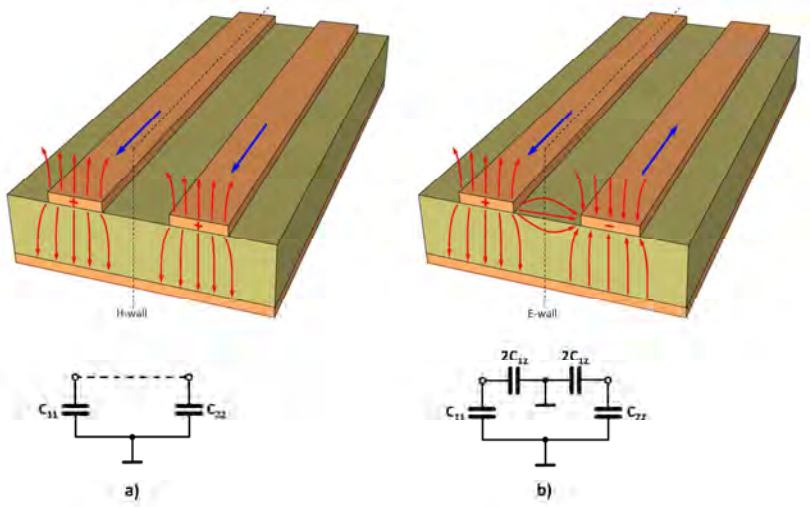

Figure 3.4: The even (a) and the odd (b) mode of the coupled microstrip line excitation

simplification, we can determine the effective capacitance between either strip and the ground:

$$C_o = C_{11} + 2C_{12} = C_{22} + 2C_{12} \tag{3.30}$$

The characteristic impedance of the microstrip coupled lines for the odd mode is [66]:

$$Z_{0o} = \frac{1}{V_{prop} C_o} \tag{3.31}$$

Any excitation of the coupled transmission lines can be considered as a superposition of the appropriate amplitudes of the even and the odd modes [118].

The method described above can not be used for asymmetrical coupler analysis directly. Let us consider two coupled microstrip lines spaced by a distance s which widths are w_1 and w_2 respectively (Fig. 3.6a). The mutual capacitance between coupled microstrip lines for this example is the same as for the equivalent configuration of symmetrical coupled lines presented in Fig. 3.6b where each line has width $(w_1 + w_2)/2$ [118]. Using this relationship, the results for mutual capacitance obtained for the two symmetrical coupled lines when each of them has width $(w_1 + w_2)/2$ can be applied for asymmetrical coupled lines where widths are w_1 and w_2 respectively. Self capacitance of the line w_1 presented in Fig. 3.6a in the presence of the line w_2 is the same as if line w_2 had the same width as w_2 [118]. Using this assumption we can calculate self capacitance of the line w_1 for configuration from Fig. 3.6a using the method of analysis of symmetrical cou-

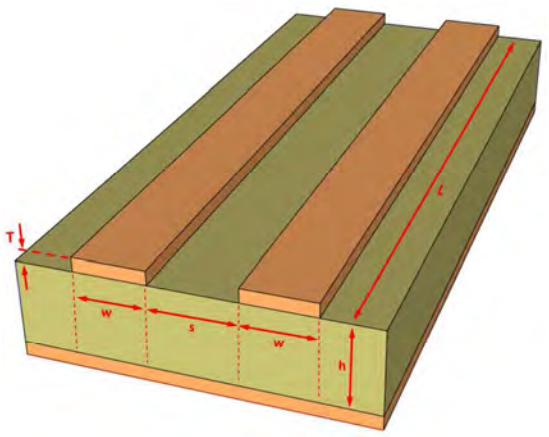

Figure 3.5: Coupled microstrip lines

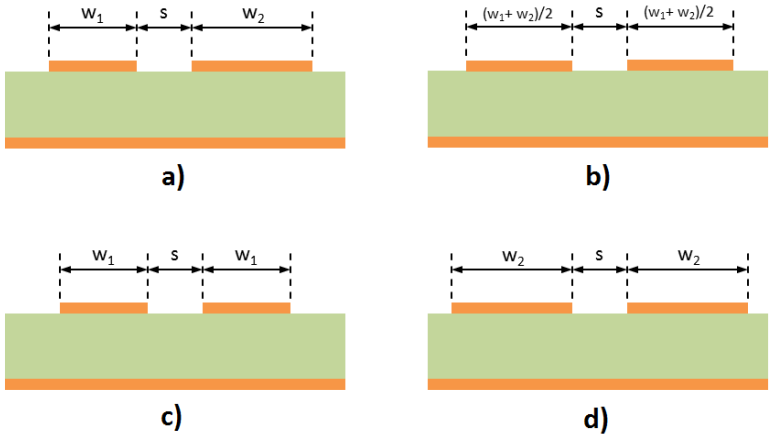

Figure 3.6: (a) Asymmetrical coupled lines of width w_1 and w_2, (b) symmetrical coupled lines of width $(w_1 + w_2)/2$, (c) symmetrical coupled lines of width w_1, (d) symmetrical coupled lines of width w_2 [118]

pled lines presented on Fig. 3.6c. Likewise, we can calculate self capacitance for the line w_2 from Fig. 3.6a using an equivalent symmetrical structure presented on Fig. 3.6d

We can determine four main threads in research related to coupled lines: development of CAD tools, full wave analysis to enhance components design, searching for new structures and configurations of couplers, and searching for new applications [118]. The purposes underlaying these activities are coupler's performance parameters improvement (bandwidth, directivity), lowering fabrica-

tion cost, size and cost optimization. It is important to note that the new very interesting properties of coupled lines can be obtained with using ferrite materials. The research has been carried in this area for many years [123, 124, 125].

3.1.2 Microstrip Coupler Design

The microstrip coupler design is based on determination of the geometrical dimensions of the coupling structure which allows us to achieve the desired coupling M[dB]. The geometrical structure of the coupled lines with its key dimensions is presented in Fig. 3.5. The even and the odd mode impedances for the coupled microstrip lines are equal [126]:

$$Z_{oe} = Z_0 \sqrt{\frac{1 + 10^{(M/20)}}{1 - 10^{(M/20)}}} \tag{3.32}$$

$$Z_{oo} = Z_0 \sqrt{\frac{1 - 10^{(M/20)}}{1 + 10^{(M/20)}}} \tag{3.33}$$

where Z_0 is the assumed characteristic impedance. The distance between two coupled microstrip lines s can be calculated using the following equation:

$$s/h = \frac{2}{\pi} \cosh^{-1}(X) \tag{3.34}$$

$$X = \frac{\cosh\left[\frac{\pi}{2}\left(\frac{w}{h}\right)'_{so}\right] + \cosh\left[\frac{\pi}{2}\left(\frac{w}{h}\right)_{se}\right] - 2}{\cosh\left[\frac{\pi}{2}\left(\frac{w}{h}\right)'_{so}\right] - \cosh\left[\frac{\pi}{2}\left(\frac{w}{h}\right)_{se}\right]} \tag{3.35}$$

where h is a PCB substrate height, $(w/h)_{se}$ and $(w/h)_{so}$ are auxiliary parameters for the even and odd modes, respectively. The $(w/h)'_{so}$ is expressed as a sum of $(w/h)_{so}$ and $(w/h)_{se}$ with constant factors:

$$\left(\frac{w}{h}\right)'_{so} = 0.78\left(\frac{w}{h}\right)_{so} + 0.1\left(\frac{w}{h}\right)_{se} \tag{3.36}$$

Auxiliary parameters $(w/h)_{se}$ and $(w/h)_{so}$ are calculated by changing auxiliary parameter P to $(Z_{0o}/2)$ for $(w/h)_{so}$ and $(Z_{0e}/2)$ for $(w/h)_{se}$ in equation:

$$(w/h)_{se,so} = \frac{8\sqrt{\left[e^{\frac{P}{42.4}\sqrt{(\epsilon_r+1)}} - 1\right]\frac{7+(4/\epsilon_r)}{11} + \frac{1+(1/\epsilon_r)}{0.81}}}{\left[e^{\frac{P}{42.4}\sqrt{(\epsilon_r+1)}} - 1\right]} \tag{3.37}$$

where ϵ_r is a dielectric constant of substrate. Finally, the (w/h) ratio can be specified as:

$$(w/h) = \frac{1}{\pi}\cosh^{-1}(m) - \frac{1}{2}\left(\frac{s}{h}\right) \tag{3.38}$$

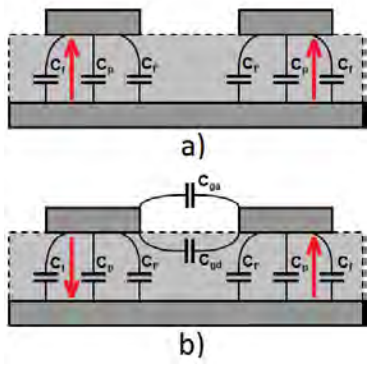

Figure 3.7: Capacitance distribution in the coupled lines for even (a) and odd (b) excitations

$$m = \frac{\cosh\left[\frac{\pi}{2}\left(\frac{w}{h}\right)_{se}\right](g+1)+g-1}{2} \tag{3.39}$$

$$g = \cosh\left[\frac{\pi}{2}\left(\frac{s}{h}\right)\right] \tag{3.40}$$

The coupler length l_C which ensures a desired value of the coupling factor at the operating frequency f_0, is equal to a quarter wavelength λ in the substrate:

$$l_C = \frac{\lambda}{4} = \frac{c}{4f\sqrt{\epsilon_{eff}}} \tag{3.41}$$

The total effective dielectric permittivity ϵ_{eff} can be calculated on the basis of an effective permittivity for even ϵ_{effe} and odd ϵ_{effo} modes:

$$\epsilon_{eff} = \left[\frac{\sqrt{\epsilon_{effe}}+\sqrt{\epsilon_{effo}}}{2}\right]^2 \tag{3.42}$$

The ϵ_{effe} and ϵ_{effo} parameters strongly depend on capacitances between conducting stripes and a ground plane, and the conductive stripes mutually (Fig. 3.7). The way of calculating permitivities for both modes with full capacitance calculations is shown below:

$$\epsilon_{effe} = \frac{C_e}{C_{e1}} \tag{3.43}$$

$$\epsilon_{effo} = \frac{C_o}{C_{o1}} \tag{3.44}$$

where C_e, C_o are total capacitances for each mode and C_{o1}, C_{e1} are similar capacitances but with air as a substrate. The total capacitance for the even (Fig. 3.7a) and odd (Fig. 3.7b) mode is a sum of these three factors:

$$C_e = C_p + C_f + C'_f \tag{3.45}$$

$$C_p = \epsilon_0 \epsilon_r \frac{w}{h} \tag{3.46}$$

where ϵ_0 is a dielectric permittivity of vacuum. The element C_f can be calculated as follow:

$$C_f = \frac{\sqrt{\epsilon_{seff}}}{2cZ_0} - \frac{C_p}{2} \tag{3.47}$$

where c is the speed of light. Permittivity ϵ_{seff} is:

$$\epsilon_{seff} = \frac{\epsilon_r + 1}{2} - \frac{\epsilon_r - 1}{2} F(w/h) \tag{3.48}$$

$$F(w/h) = \begin{cases} (1 + 12h/w)^{-1/2} + 0.041(1 - w/h)^2 & \text{for } (w/h) \leq 1 \\ (1 + 12h/w)^{-1/2} & \text{for } (w/h) > 1 \end{cases} \tag{3.49}$$

$$C'_f = \frac{C_f}{1 + E(\frac{h}{s})\tanh(\frac{10h}{s})} \left(\frac{\epsilon_r}{\epsilon_{seff}} \right)^{1/4} \tag{3.50}$$

$$E = e^{-0.1e^{\left(2.33 - 1.5\frac{w}{h}\right)}} \tag{3.51}$$

Similar considerations can be carried out for the odd mode (Fig3.7b). For this case, the inter-strip capacitance must be added:

$$C_o = C_p + C_f + C_{ga} + C_{gd} \tag{3.52}$$

$$C_{ga} = \epsilon_0 \frac{K(k')}{K(k)} \tag{3.53}$$

$$\frac{K(k')}{K(k)} = \begin{cases} \frac{1}{\pi} ln \left[2\frac{1+\sqrt{k'}}{1-\sqrt{k'}} \right] & \text{for } 0 \leq k^2 \leq 0.5 \\ \frac{\pi}{ln\left[2\frac{1+\sqrt{k'}}{1-\sqrt{k'}}\right]} & \text{for } 0.5 \leq k^2 \leq 1 \end{cases} \tag{3.54}$$

$$k = \frac{\left(\frac{s}{h}\right)}{\left(\frac{s}{h}\right) + \left(\frac{2w}{h}\right)} \tag{3.55}$$

$$k' = \sqrt{1 - k^2} \tag{3.56}$$

$$C_{gd} = \frac{\epsilon_0 \epsilon_r}{\pi} \ln(U) + 0.65 C_f Y \tag{3.57}$$

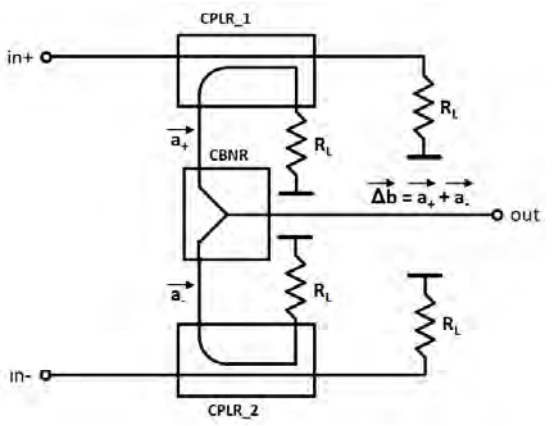

Figure 3.8: Broadband high frequency differential coupler [127]

$$U = coth\left(\frac{\pi}{4}\frac{s}{h}\right) \tag{3.58}$$

$$Y = \frac{0.02}{\left(\frac{s}{h}\right)}\sqrt{\epsilon_r} + \left(1 - \frac{1}{\epsilon_r^2}\right) \tag{3.59}$$

The relationship between C_e, C_{e1} and C_o, C_{o1} can be described by the following equations:

$$C_{e1} = \frac{1}{c^2 C_e Z_{oe}^2} \tag{3.60}$$

$$C_{o1} = \frac{1}{c^2 C_o Z_{oo}^2} \tag{3.61}$$

3.2 Differential signal coupler

The differential signal coupler is a device which is used for differential signal decoupling from the pair of lines which works with differential signaling. The basic concept of a wide-band differential coupler which converts the decoupled differential signal to an unbalanced one is presented in [127]. The device architecture basis on the use of two identical couplers (CPLR_1, CPLR_2) and a power combiner (CBNR) (Fig. 3.8). The single coupler CPLR_1 decouples signal a_+ from the input port in+. Similarly, the coupler CPLR_2 decouples signal a_- from the input in-. The signals decoupling by both couplers are summed by CBNR. The combiner's produces a signal $\Delta b = a_+ + a_-$. The high bandwidth of all components and high coupler's directivity make it possible to obtain a differential coupling factor and high common mode rejection ratio [127].

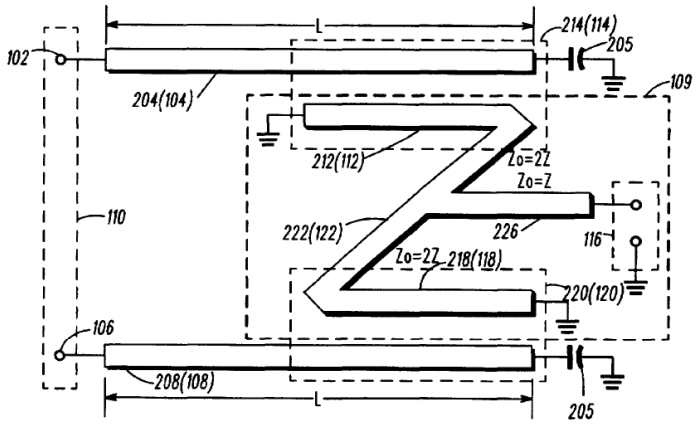

Figure 3.9: Differential signal to unbalanced port converter [128]

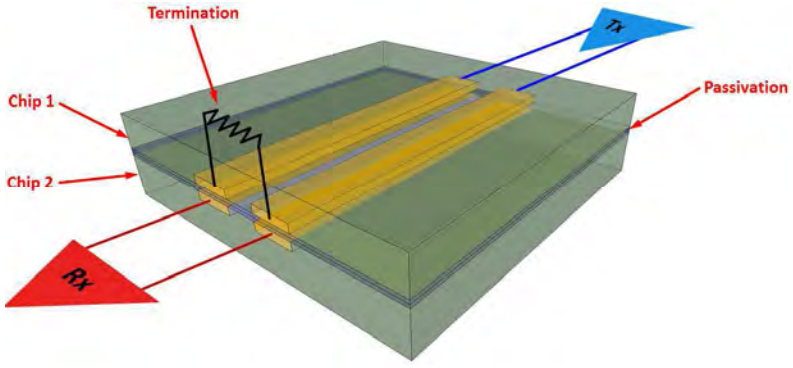

Figure 3.10: Concept of the chip-stacking technology utilizing transmission line couplling [108]

The interesting implementation of the coupler used for differential to single ended port conversion was invented and patented by Motorola Inc. (Fig. 3.9 US Patent No. 5,777,527) [128]. The presented device is composed of two resonators (204 and 208) which are loaded by shunting capacitors (205). The differential signal is applied to a differential port (110) between the resonators. The signals from the resonators are decoupled by the directional couplers (212 and 218) and delivered to the unbalanced output (116) by the phase shifting network (222, 226). It is important to notice that the considered solution assumes that the coupler is placed behind the transmission lines. Due to this, direct decoupling of the differential signal from the pair of the coupled microstrip lines is not possible.

Another concept of a differential signal coupler which is applied for chip-stacking technology to obtain very high bandwidth of differential chip-to-chip communication is presented in [108] (Fig. 3.10). The technology assumes contactless interconnection from the transmitter Tx to the receiver Rx utilizing inductive and capacitive coupling to achieve high yield, low cost, high performance and reliability in 3D integration. Each chip has exposed a pair of transmission lines on the edge plane of the cover terminated with the matched load. The first chip (Tx) is imposed on the second (Rx) in such a way that the transmission lines overlaps. The transmission lines from the two chips has no direct contact. They are separated by a thin passivation layer. The two pairs of transmission lines forms a proximity differential signal coupler which transfers the signal from the first chip to the second one. The sample test structure measured in [108] has dimensions as follow: single line width w=20μm, distance between two lines in single chip s=20μm. The lines in each chip are separated by s_P=6.6μm passivation layer. The authors [108] obtained the 20Gb/s transmission rate.

The main reason that encouraged the author to consider the possibility of creating a new type of a differential signal coupler design was the need of contactless transmission in the pair coupled microstrip lines realized in PCB technology monitoring [55]. The main aim of the new design was the ability to overlay the coupling structure on the monitored transmission line and decouple the small part of the signal which will be sufficient to monitored data stream recovery without disturbing transmission in the monitored line. Taking into account the conditions considered above, the use of known configurations was not possible.

3.2.1 Differential signal coupler for data transmission monitoring

This section describes the new concept of a differential signal coupler for contactless data transmission monitoring in coupled microstrip lines proposed and developed by the author [55, 56, 57]. The main problem of the high speed transmission monitoring is a proper signal probing without affecting transmission in the monitored line. This goal can be achieved with relatively low coupling factor level and physical construction of coupler which does not disturb the EM field distribution around the transmission line which guides the probed signal. The research on determination of optimal coupling factor is summarized in Chapter 4. In the following considerations, the influence of the coupler on the main transmission line under test will be defined as the impact of the coupler on **S** parameters of the main line (measured from the Tx and Rx side) within the operating bandwidth. The obtained **S** parameters for the configuration consisting of the line and the coupler will be related to the parameters of the line without the coupler. After adding the coupler, the working conditions from the Tx and Rx point of view should not be changed. It is acceptable that the coupler has non-negligible impact on the main transmission line working conditions outside the operating bandwidth of the link.

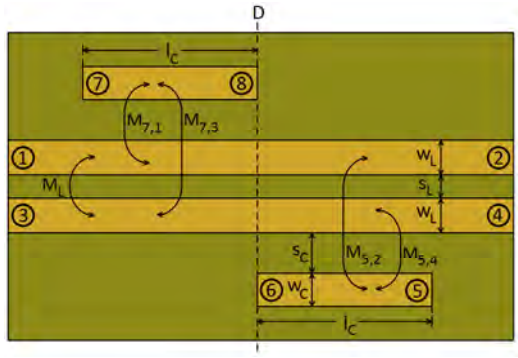

Figure 3.11: Concept of differential signal coupler for transmission monitoring

Contact-less probing can be realized by endowing the PCB with a coupler on the monitored transmission line [52]. In this approach, it is necessary to satisfy a few conditions. Most importantly, the overlayed coupler should not significantly affect the impedance of the main line - this assumption can be satisfied by using sufficiently small coupling factor and the appropriate structure of coupler's board implementation. On the other hand, the coupling factor must be sufficiently large to decouple a part of the signal which can be subsequently processed in the next functional block of the measurement system (equalizer, flip-flop and data acquisition subsystem) in the specified frequency band. We assume that the coupler works with an existing transmission line so that only the geometrical dimensions of the coupler itself are considered to be the designable parameters.

In the first approach, let us consider the differential signal coupler which is implemented on the same PCB as the monitored line (Fig. 3.11). In [56, 57], the author demonstrated by measurements that, with very good approximation, this setup can be used to analyze the coupler overlayed on a PCB with the line when the coupler's branches are implemented on the separate parts of the laminate and no additional laminate is overlayed directly on the line under test. The proposed differential signal coupler is composed of the two simple, classical proximity couplers (lines 5-6 and 7-8) located on both sides of the transmission line (1-2, 3-4). Minimum impact on the transmission line is accomplished by shifting one coupler apart from the other one along the line. This configuration allows us to eliminate the undesired capacitances between branches (Fig. 3.12). The useful signal in the transmission line V_d (defined as a difference of signals in lines 1-2 and 3-4) is guided by a pair of parallel, coupled paths (the main transmission line). A total guided signal V_d can be represented as a set of two components defined as signals V_1 and V_3 between a common ground plane and the corresponding wires (1-2 and 3-4 respectively). Signals V_1 and V_3 have the same amplitudes and opposite phases. In the far field area, the sum of V_1 and V_3 is zero. Let us define the following coupling factors in [dB] for coupling phenomena between the pairs of paths: M_L, $M_{5,2}$, $M_{5,4}$, $M_{7,3}$, $M_{7,1}$ (Fig. 3.11). Geometrical

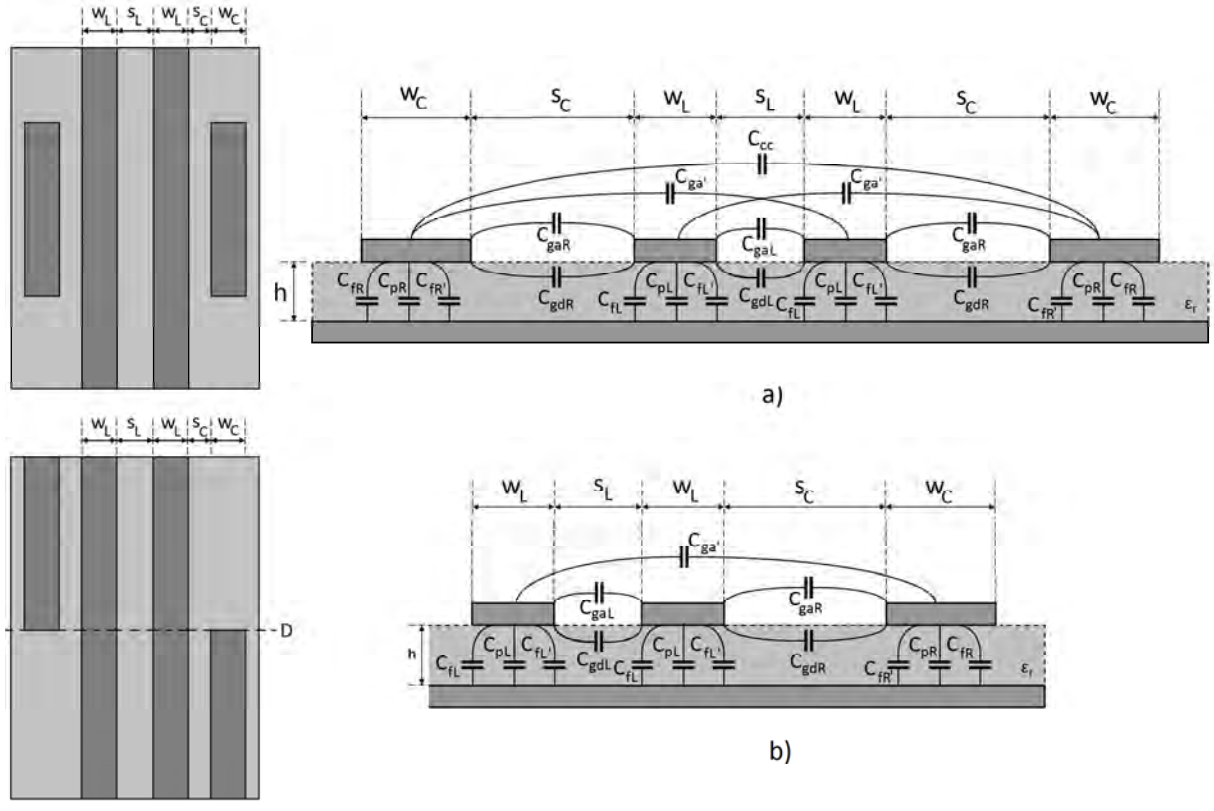

Figure 3.12: Differential signal coupler. Un-shifted (a) and shifted (b) configuration with inter strip capacitances

relations between the dimensions of the transmission line and the coupling strips allow us to assume that $M_{5,2} < M_{5,4}$ and analogically $M_{7,3} < M_{7,1}$. Let us define an additional signal V'_d (defined as the difference of the signals at points 5 and 7) and assume that $V'_d \sim V_d$. Geometrical dimensions of the coupling lines, s_C, w_C and l_C, are determined by the desired differential coupling factor M_{diff} (defined as a coupling factor between a differential transmission line port 1-3 and a coupler output port 6-7) for a given frequency with minimal coupler impact on the transmission line. We demonstrate that it is possible to use the design methodology adopted from the classical directional coupler [56, 57] as a proper tool for designing the coupler overlayed on the transmission line while maintaining a particular structure of the coupler's board. The examples of physical implementation of differential couplers is presented in Chapter 4 (Sections 4.3 and 4.7).

3.2.2 Directivity optimization

Although the directional coupler for microstrip line technology is a quite old invention, a considerable research effort is still observed to improve the key performance parameters and miniaturization [129, 130, 131, 132, 133]. We still observe the research and development on optimization techniques for classical constructions of couplers. According to the design methodology presented in Section 3.2, where the differential signal coupler was decomposed into two identical couplers and the design was carried out for a single structure, the differential signal coupler optimization will be performed the same way. The coupler will be decomposed into two identical sections and the optimization procedure will be performed for a single section.

The most important parameter of the coupler which will determine its ability to decouple the signal from the monitored line, which is guided in a particular direction, is directivity. The directivity can be significantly improved by the phase velocity alignment for even and odd modes. There are four main methods that can be used for improving directivity of the microstrip coupler [133, 134]: (1) adding lumped capacitances at the end of the coupled lines [118], (2) using dielectric overlay on the top of the coupled lines [135], (3) using wiggly lines [118] and (4) using stepped impedance [136].

All techniques of coupler directivity improvement listed above are suitable for microstrip technology. However, there are many limitations which do not allow us to use it for differential signal coupler for data transmission monitoring which will be overlayed on PCB with the line under test. The first and the most important issue is the possibility of modifying the geometry only for the branch. The restriction is that it is not allowed to connect any additional elements which eliminates the wave velocity compensation by adding external capacitors. Addition an extra dielectric block between the transmission line and the coupling branch will disturb the main transmission line working conditions which is unacceptable. Finally, the structure of the transmission line which guides the probed signal can not be modified at all (the wiggly line and stepped impedance technique can not be applied directly).

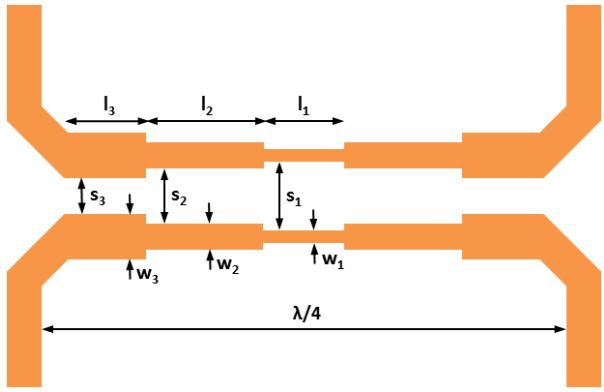

Figure 3.13: Coupler directivity improvement with step impedance technique

The original stepped impedance methodology assumes that both mode velocity can be compensated by proper choosing sections length, impedance and local coupling factor 3.13) [133]. The wave traveling along the sections from the input to the isolated port are reflected and canceled out, which finally improves the directivity. In [136], it was suggested that the number of sections should be limited to three and each section should have the same length (total branch length should be $\lambda/4$). In [133] author presents the sample measurement results obtained for three and five section configurations. The dimensions of improved structures were obtained through optimization.

The author decided to use the stepped impedance technique to design the modified version of the coupler. The incentive for using these approach is the general assumption that only geometrical dimensions of the coupler branch can be adjusted. The proposed modification allows to meet electrical design requirements with maintaining desired mechanical properties [54, 53]. The design is presented in Chapter 4.

Chapter 4

Simulations, Measurements and Applications

This chapter presents the simulation and measurement results of physically realized differential signal couplers. Considered models were designed using methodologies presented in Section 3.1.2. The obtained results confirm the correctness of the approach used to the design of a differential signal coupler for measurement purposes. The final sections present the review of applications (not limited to measurements). The chapter is organized as follows:

- In Section 4.1 the analysis of the coupler's impact on working conditions of main transmission line is analyzed. The analysis is executed for several transmission line self coupling factors and single branch coupling factors. All simulations are performed for two configurations of the coupler: shifted and unshifted. The main goal of this research is to determine the relations between transmission line self coupling factor, coupler's coupling and the impact on main transmission line scattering parameters. The second goal is to determine the optimal value of branch coupling factors from main transmission line impact point of view.

- Section 4.2 describes the measurement results of differential signal couplers designed for operating frequency f_0=5GHz implemented in two versions: shifted and unshifted. The main goal of this experiment is to determine, in practical way, the real difference in coupler's impact on main transmission line for both coupler's configurations.

- In Section 4.3, the simulation and measurement results for differential signal couplers in shifted configuration designed for f_0=1GHz operating frequency are presented. The configuration where coupler is implemented on the same PCB as the monitored line is compared with the reference transmission line (without a coupler) and the transmnission line with two other configurations of couplers, implemented on the separate boards which are overlayed

on the PCB under test. The experiments should determine whether the proposed design methodology of the differential signal coupler can be applied to versions overlayed on PCB with the monitored line.

- Section 4.4 describes the coupler's directivity optimization process which is applied to the differential signal coupler designed and measured in Section 4.3. The coupler's directivity improvement should increase the time resolution of the transmission monitoring. Apart from the simulations, the measurements are performed as well. The results are compared with data obtained in Section 4.3 for the non-optimized version and the reference transmission line.

- In Section 4.5, the simulation results for signal decoupling from the main transmission line which guides the transmission in the differential mode are presented. The analysis is done for two versions of couplers in shifted configuration: non-optimized and optimized. The transmission line with the coupler are modeled with **.sNp* files obtained by measurements in Section 4.3 and 4.4.

- Section 4.6 describes the measurement results for signal decoupling from the main transmission line which guides the transmission in the differential mode. The analysis is performed for non-optimized and optimized version of the differential signal coupler. The main goal of measurements is practical verification of simulations conducted in Section 4.5 and the final confirmation of possibility of signal probing with differential signal coupler from the pair of coupled microstrip lines which guides differential transmission.

- Section 4.7 includes the description of potential applications of the differential signal coupler which include bur are not limited to serial transmission monitoring.

4.1 Analysis of coupler's impact on transmission line

Overview

This section presents an analysis of the coupler's impact on working conditions of the main transmission line. The simulations were executed with Agilent Momentum 3D Planar EM Simulator [137] for several transmission line self coupling factors and single branch coupling factors. The two configurations of the coupler were considered: unshifted (Fig. 4.1a) and shifted (Fig. 4.1b). As criteria to define the impact of the probing coupler on the main transmission line under test, the influence of the coupler on the transmission line scattering parameters were taken. The set of parameters which are taken as a metric is transmission line match, transmission line self coupling and total transmission line loss. All simulation results will be evaluated in the frequency band up to $1.5f_0$=1.5GHz (we assume that communication in the main line can use this band).

Table 4.1: Geometrical dimensions of main line for several self coupling factors

	-10dB	**-15dB**	**-20dB**
s_L	0.17mm	0.67mm	1.59mm
w_L	2.5mm	2.88mm	3.02mm

Table 4.2: Geometrical dimensions of coupler's branch for several coupling factors

	-10dB	**-13dB**	**-15dB**	**-17dB**	**-20dB**	**-22dB**
s_c	0.17mm	0,43mm	0.67mm	0.98mm	1.59mm	2.18mm
w_c	2.5mm	2.77mm	2.88mm	2.95mm	3.02mm	3.04mm

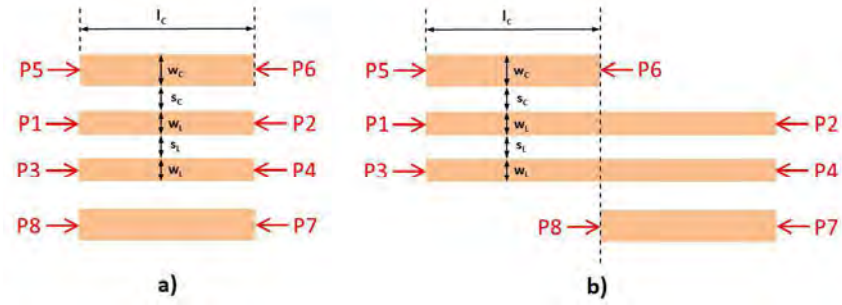

Figure 4.1: The geometrical structures of (a) unshifted and (b) shifted version of differential signal coupler

Goals

The main goal of the analysis is to determine the relations between the transmission line self coupling factor, coupler's coupling and the impact on the main transmission line scattering parameters. The second objective is to determine the optimal coupling factor for the coupler, which allows post-processing of the probed signal in the subsegment blocks of the measurement system (equalizer, flip-flop and data acquisition subsystem) without disturbing working conditions of the transmission line throughout the link bandwidth.

Simulations

To determine the impact of the coupler on the main transmission line, several simulations for different values of the transmission line self coupling factors S_{31} and branch coupling values S_{51} for both coupler configurations were performed. The three sample transmission line self coupling factors (-10dB, -15dB and -20dB) and six values of the single branch coupling (-10dB, -13dB, -15dB, -17dB, -20dB and -22dB) for each case were taken. The circuits were analyzed in band 50MHz-3GHz. The assumed operating frequency is f_0=1GHz which gives the

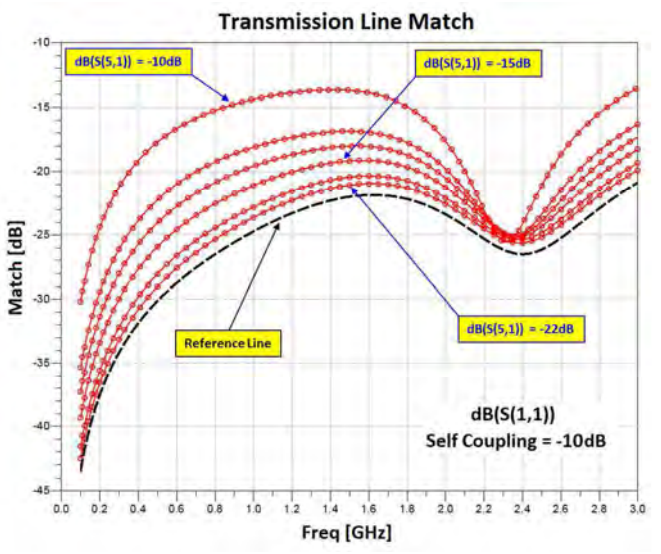

Figure 4.2: The simulation results for un-shifted coupler configuration. The dependency of transmission line match and coupler's branch coupling factor for M_L=-10dB

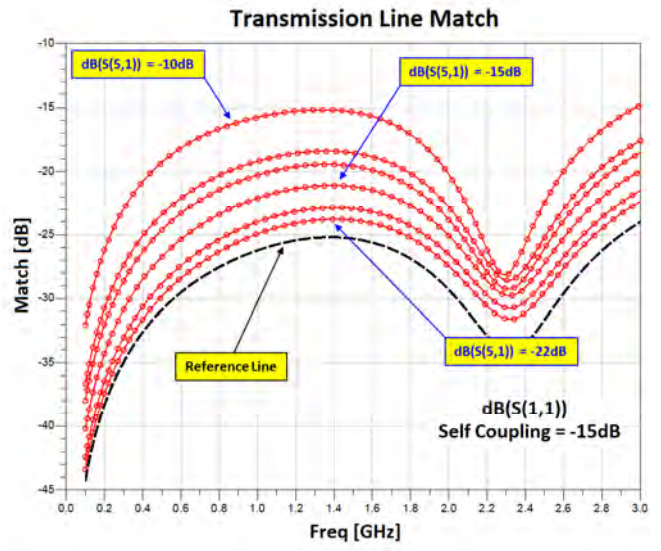

Figure 4.3: The simulation results for un-shifted coupler configuration. The dependency of the transmission line match and the coupler's branch coupling factor for M_L=-15dB

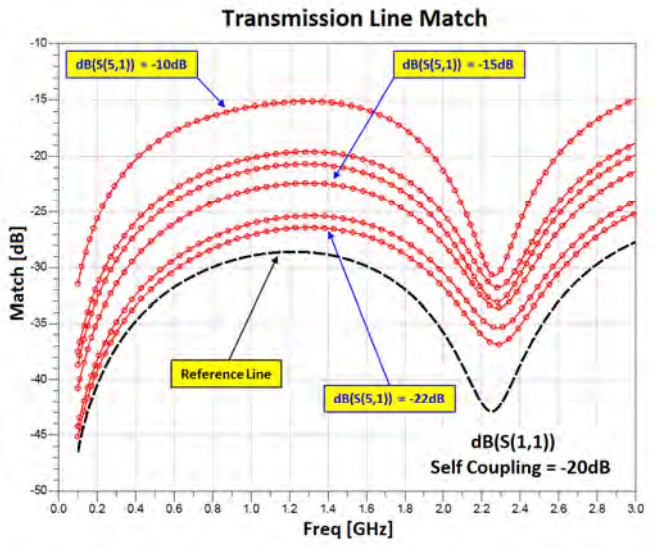

Figure 4.4: The simulation results for un-shifted coupler configuration. The dependency of the transmission line match and the coupler's branch coupling factor for M_L=-20dB

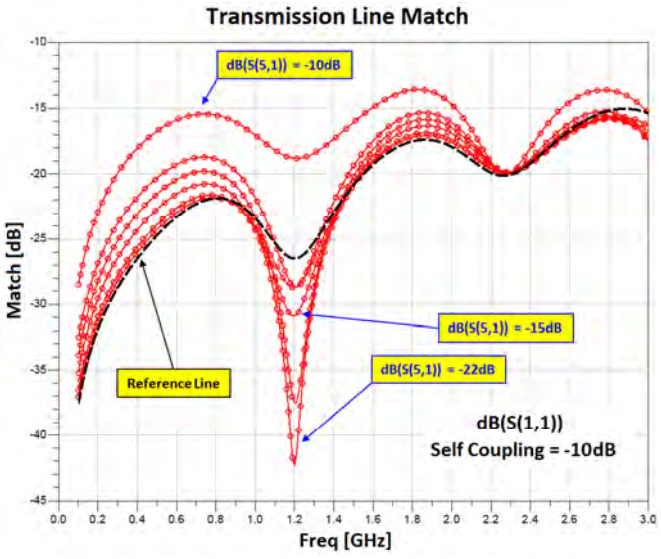

Figure 4.5: The simulation results for shifted coupler configuration. The dependency of the transmission line match and the coupler's branch coupling factor for M_L=-10dB

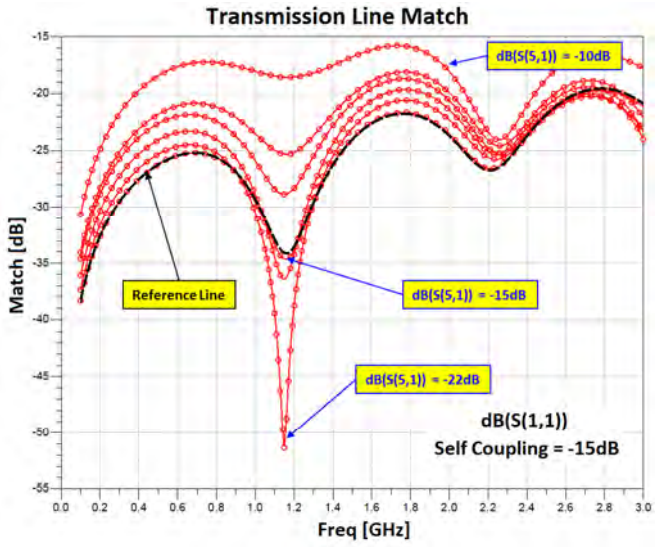

Figure 4.6: The simulation results for shifted coupler configuration. The dependency of the transmission line match and the coupler's branch coupling factor for M_L=-15dB

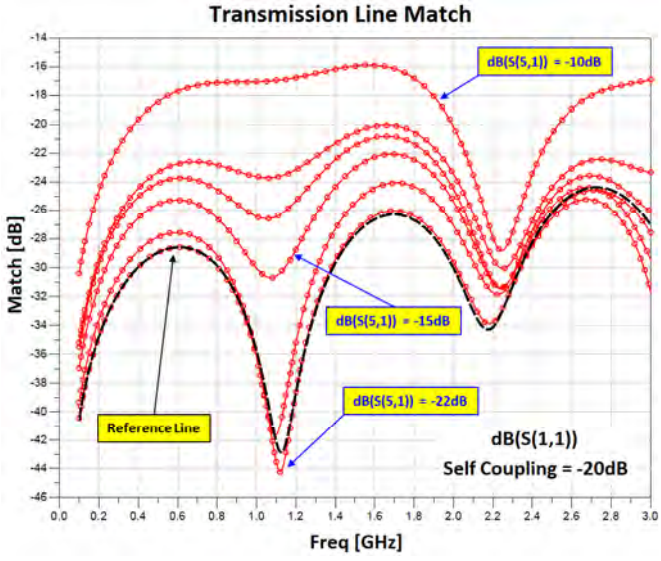

Figure 4.7: The simulation results for shifted coupler configuration. The dependency of the transmission line match and the coupler's branch coupling factor for M_L=-20dB

coupler's branch length l_c=41.33mm. Other geometrical dimensions for each configurations are presented in Tab. 4.1 and Tab. 4.2.

As expected, the influence of the differential signal coupler on the transmission line match for both configurations strongly depends on the level of branch coupling factor. This impact is more visible for unshifted (Fig. 4.2, Fig. 4.3 and Fig. 4.4) than for shifted (Fig. 4.5, Fig. 4.5 and Fig. 4.7) configuration. Moreover, we can observe that the level of this influence strongly depends on relation between the main transmission line self coupling factor M_L (S_{31}) and branch coupling S_{51}. The differential signal coupler affects lesser the main line match when the difference between M_L (S_{31}) and branch coupling factor S_{51} increases. Based on the data obtained for the performed simulations, we can decide that for un-shifted structure, the impact of the coupler on the main transmission line match is negligible (lower than 1dB) when single branch coupling factor S_{51} is at least 12dB lower than the transmission line self coupling M_L (S_{31}). For shifted configuration, the same criterion gives 5dB difference.

Similar considerations can be conducted for impact of the coupler on the main transmission line self-coupling factor. The mechanism which describes the influence of the coupler on the main transmission line self-coupling is similar as for the transmission line match case. The impact of the coupler assuming the same coupling and line self coupling factor is greater for unshifted configuration, however, the relation between M_L (S_{31}) and branch coupling S_{51} which ensures compliance with the 1dB criteria is not so strong as for the line match. Analyzing the Fig. 4.8, Fig. 4.9 and Fig. 4.10 we can observe that for unshifted configuration, the sweep of the coupling factor S_{51} (from -10dB to -22dB) results in the transmission line self-coupling factor impact at the level of 2dB to 3dB for all analyzed values of M_L (-10dB, -15dB and -20dB). Based on Fig. 4.11, Fig. 4.12 and Fig. 4.13 we can determine that for the same scenario, the impact of the coupler on the transmission line self-coupling is at the level of 1dB to 2dB.

To evaluate the boundary value of coupling factors according to the impact on the main transmission line loss characteristic, the 0.2dB criteria was taken. We can observe that the impact on the transmission line loss characteristic is higher for the shifted structure and high branch coupling factors S_{51} (up to 0.9dB) than for the unshifted version (up to 0.75dB). However, for low coupling factors we are dealing with the opposite trend: the shifted structure introduces less disturbances (close to zero for S_{51}=-22dB) than the un-shifted one (up to 0.05dB).

Conclusions

Summarizing all previous observations, we can confirm that for appropriately low level of branch coupling it is possible to design a differential signal coupler which does not disturb working conditions of the main line in terms of the assumed acceptance criteria (for the main transmission line match and self coupling 1dB and for transmission loss 0.2dB of permissible impact). The final criteria of maximal branch coupling factor determination S_{51} which satisfies all presented

Figure 4.8: The simulation results for un-shifted coupler configuration. The dependency of the transmission line self coupling and the coupler's branch coupling factor for M_L=-10dB

requirements is:

$$|S_{51}| \leq M_L - 12dB, \qquad \text{for un-shifted structure} \tag{4.1}$$

$$|S_{51}| \leq M_L - 5dB, \qquad \text{for shifted structure} \tag{4.2}$$

On the other hand, the coupling factor must be sufficiently large to decouple a part of the signal which can be subsequently processed in the next functional block of the measurement system. Combining the all conditions listed above, the optimal value of coupling factor for single branch can be described as:

$$|S_{51}| = M_L - 12dB, \qquad \text{for un-shifted structure} \tag{4.3}$$

$$|S_{51}| = M_L - 5dB, \qquad \text{for shifted structure} \tag{4.4}$$

In the designs, tests, simulations and measurements presented in the following sections, a configuration with M_L=-15dB and S_{51}=-20dB is considered. For most cases, the shifted version of the coupler was used as a configuration which has less impact on the main line.

Figure 4.9: The simulation results for un-shifted coupler configuration. The dependency of the transmission line self coupling and the coupler's branch coupling factor for M_L=-15dB

Figure 4.10: The simulation results for un-shifted coupler configuration. The dependency of the transmission line self coupling and the coupler's branch coupling factor for M_L=-20dB

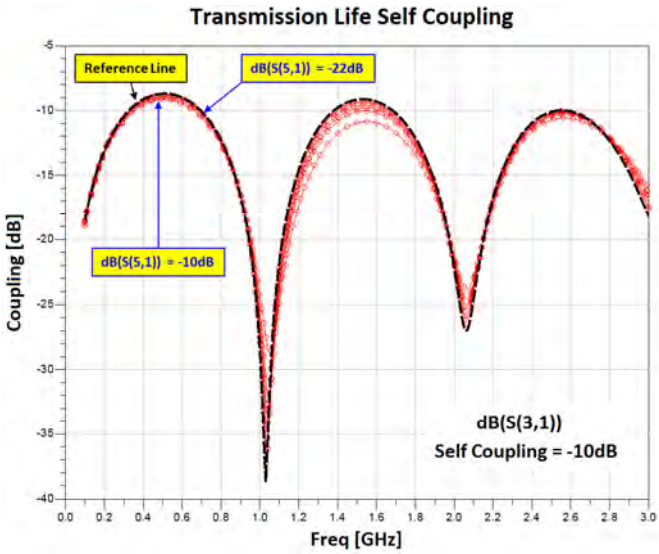

Figure 4.11: The simulation results for shifted coupler configuration. The dependency of the transmission line self coupling and the coupler's branch coupling factor for M_L=-10dB

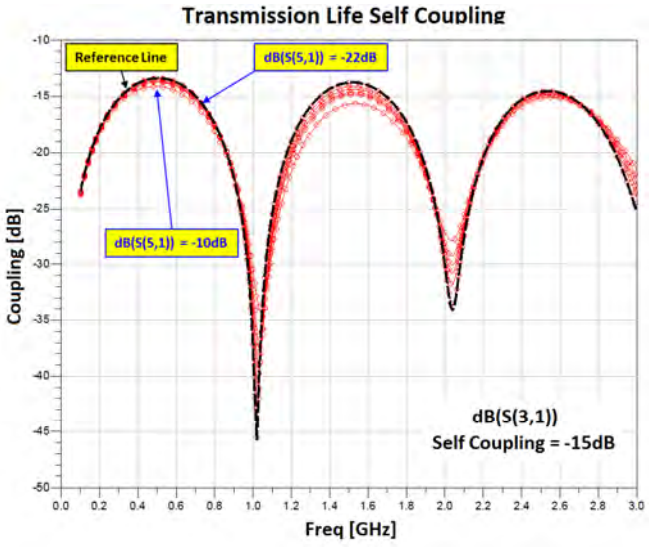

Figure 4.12: The simulation results for shifted coupler configuration. The dependency of the transmission line self coupling and the coupler's branch coupling factor for M_L=-15dB

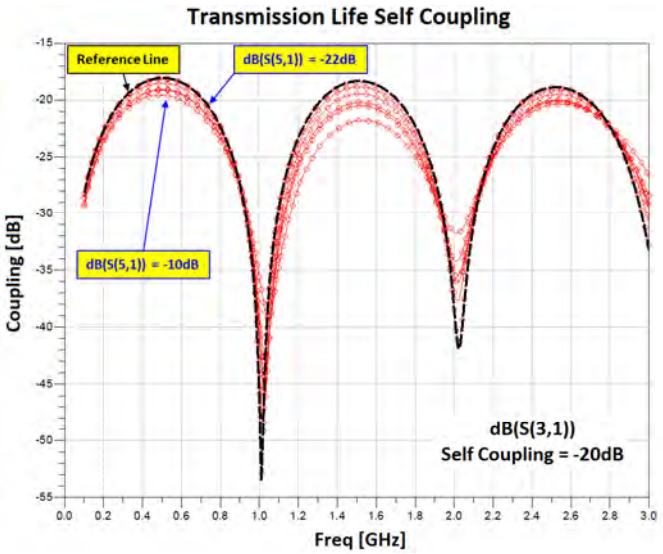

Figure 4.13: The simulation results for shifted coupler configuration. The dependency of the transmission line self coupling and the coupler's branch coupling factor for M_L=-20dB

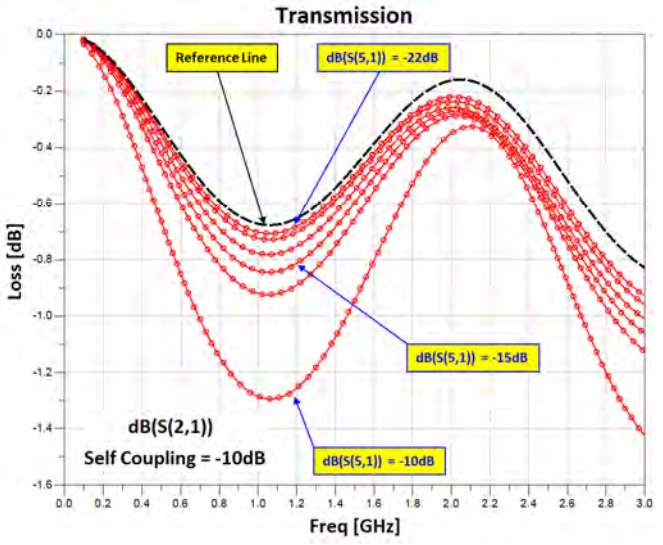

Figure 4.14: The simulation results for un-shifted coupler configuration. The dependency of the transmission line loss and the coupler's branch coupling factor for M_L=-10dB

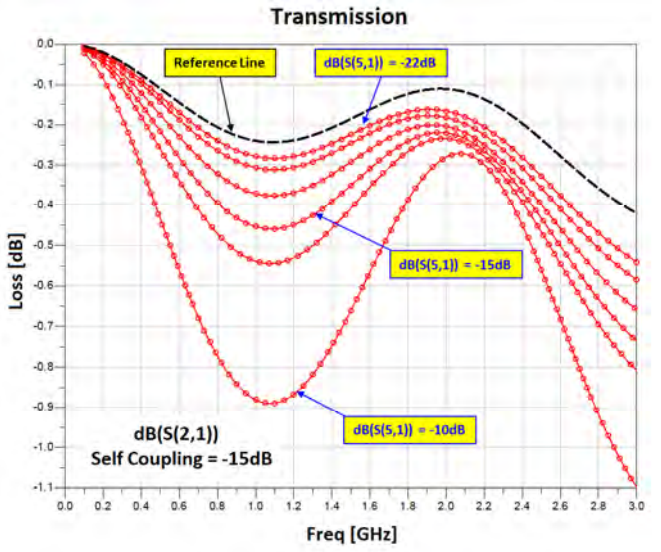

Figure 4.15: The simulation results for un-shifted coupler configuration. The dependency of the transmission line loss and the coupler's branch coupling factor for M_L=-15dB

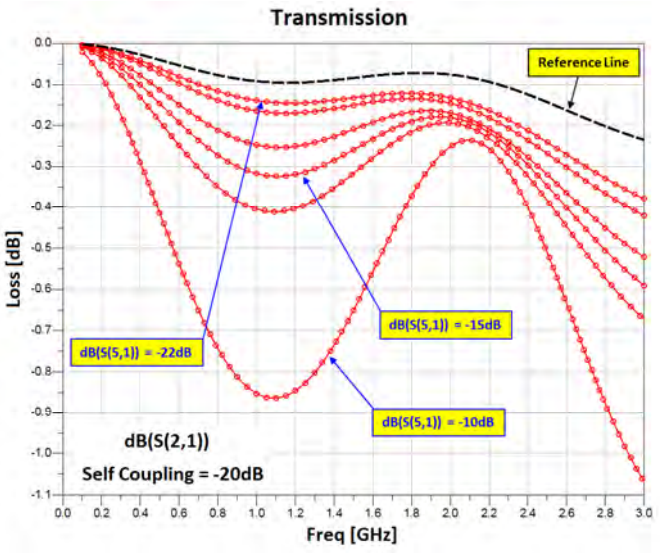

Figure 4.16: The simulation results for un-shifted coupler configuration. The dependency of the transmission line loss and the coupler's branch coupling factor for M_L=-20dB

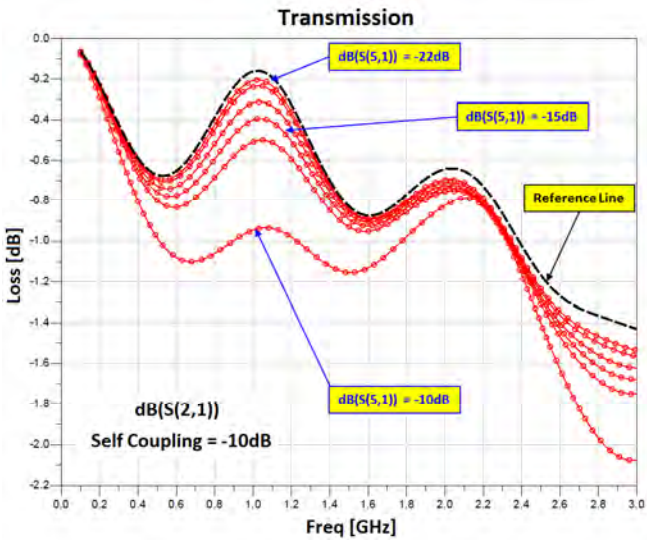

Figure 4.17: The simulation results for shifted coupler configuration. The dependency of the transmission line loss and the coupler's branch coupling factor for M_L=-10dB

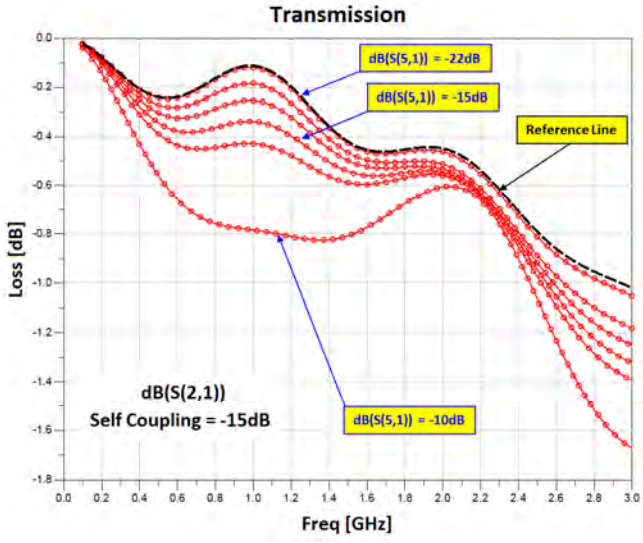

Figure 4.18: The simulation results for shifted coupler configuration. The dependency of the transmission line loss and the coupler's branch coupling factor for M_L=-15dB

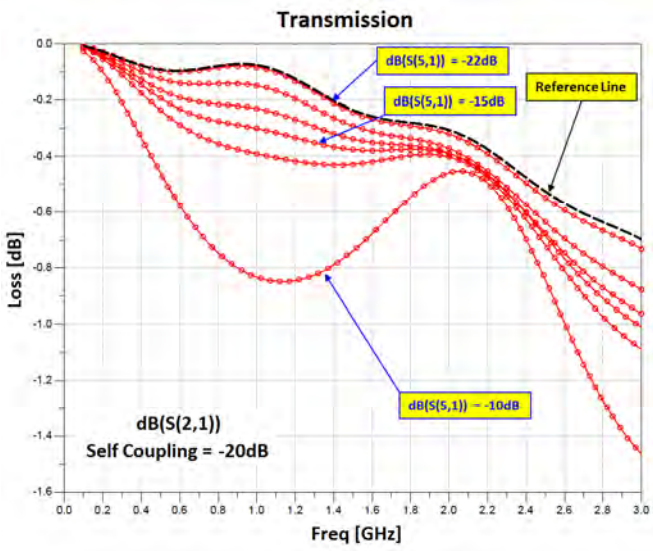

Figure 4.19: The simulation results for shifted coupler configuration. The dependency of the transmission line loss and the coupler's branch coupling factor for M_L=-20dB

4.2 5GHz differential signal coupler

Overview

This section presents the design and measurements of a differential signal coupler designed for operating frequency f_0=5GHz for PCIe 2.0 transmission monitoring (500MB/s per lane) [59]. Two versions of the coupler were measured: a shifted (Fig. 4.20) and an unshifted (Fig. 4.21) configuration. The measurements were performed in frequency domain using Vector Network Analyzer (VNA).

Goals

The obtained results should verify the theoretical design considerations conducted in the previous chapter. Additionally, the experiment will determine the actual difference in coupler's impact on the main transmission line for both coupler's configurations.

Design and measurements

The main transmission line composed of the two coupled microstrip lines, should have -15dB of coupling between the lines at the operating frequency

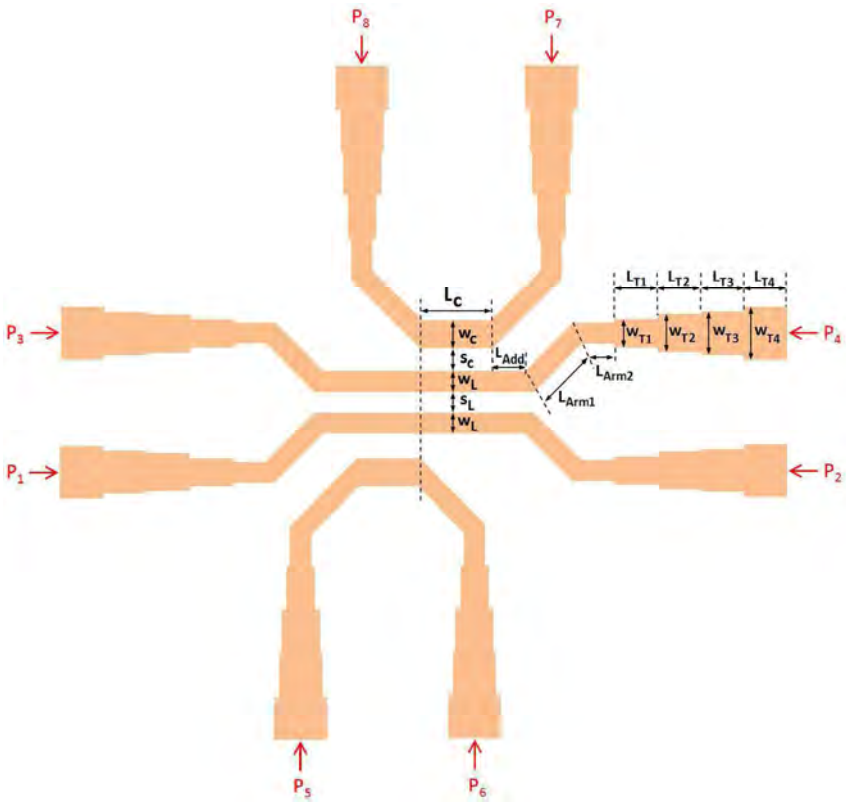

Figure 4.20: Differential signal coupler (shifted structure) for PCIe 2.0 transmission monitoring (f_0=5GHz)

Table 4.3: Geometrical dimensions of 5GHz PCIe 2.0 differential signal coupler (shifted structure, S_{31}=-15dB, S_{51}=-20dB)

Dimension	Value [mm]	Dimension	Value [mm]
w_L	0.75	L_{Arm2}	4.95
s_L	0.41	w_{T1}	0.84
w_C	0.77	L_{T1}	8.16
s_C	0.75	w_{T2}	0.89
L_C	9.26	L_{T2}	7.97
L_{Add}	19.71	w_{T3}	0.99
w_{Arm1}	0.79	L_{T3}	8.23
L_{Arm1}	30.34	w_{T4}	1.06
w_{Arm2}	0.79	L_{T4}	7.91

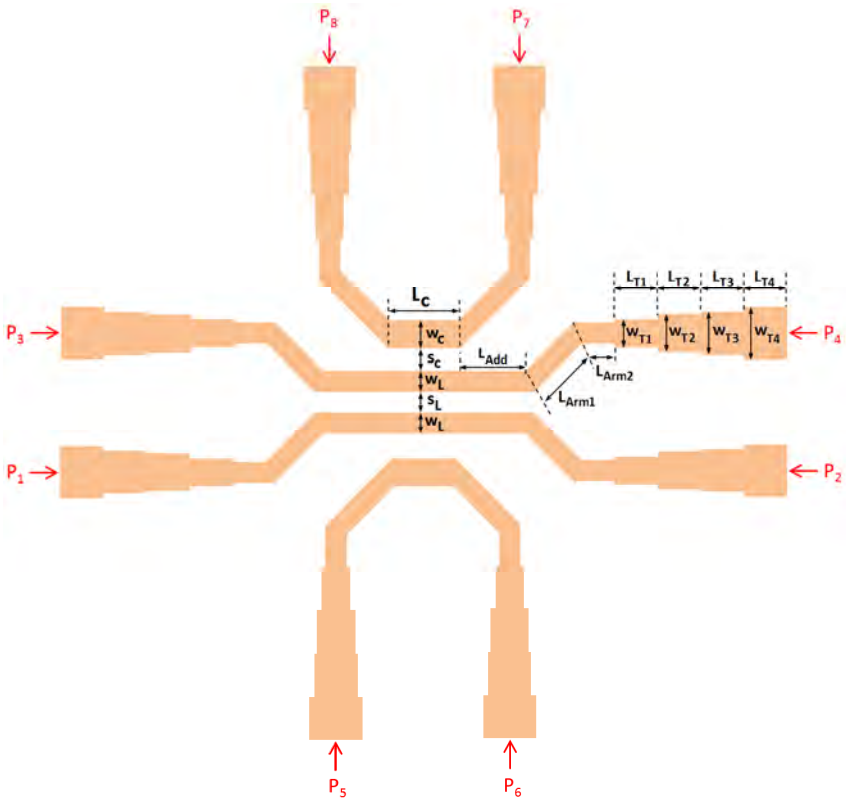

Figure 4.21: Differential signal coupler (unshifted structure) for PCIe 2.0 transmission monitoring (f_0=5GHz)

Table 4.4: Geometrical dimensions of 5GHz PCIe 2.0 differential signal coupler (unshifted structure, S_{31}=-15dB, S_{51}=-20dB)

Dimension	**Value [mm]**	**Dimension**	**Value [mm]**
w_L	0.75	L_{Arm2}	4.95
s_L	0.41	w_{T1}	0.84
w_C	0.77	L_{T1}	8.16
s_C	0.75	w_{T2}	0.89
L_C	9.26	L_{T2}	7.97
L_{Add}	24.34	w_{T3}	0.99
w_{Arm1}	0.79	L_{T3}	8.23
L_{Arm1}	30.34	w_{T4}	1.06
w_{Arm2}	0.79	L_{T4}	7.91

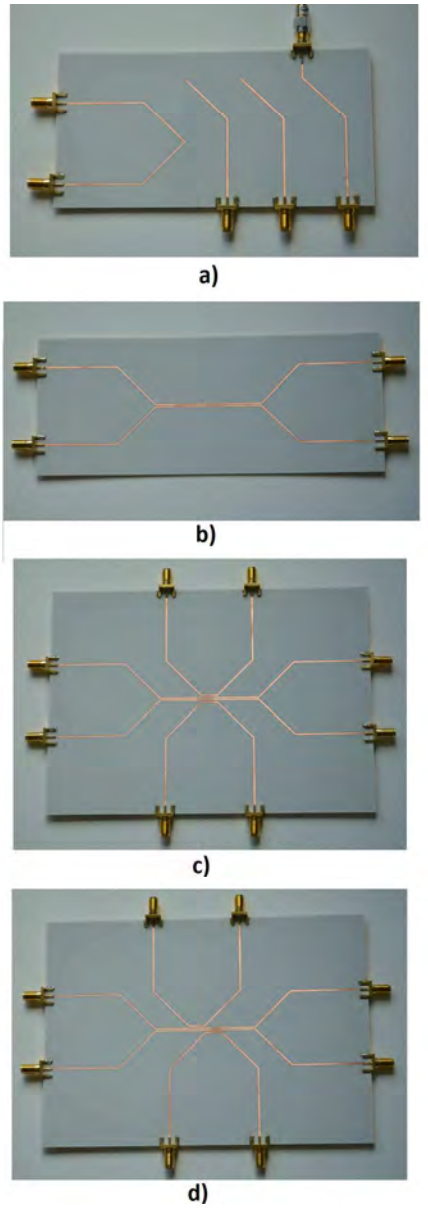

Figure 4.22: 5GHz differential signal coupler test boards: (a) calibration kit, (b) reference transmission line, (c) transmission line with unshifted version of coupler, (d) transmission line with shifted version of coupler

f_0=5GHz. To be compliant with PCIe 2.0 specification it was assumed that the characteristic impedance of the transmission line is Z_0=60Ω. The impedance measured between the two coupled mictostrip lines should be equal to Z_d=100Ω ($Z_d = 2Z_{0o}$). The desired level of coupling between the microstrip lines in the main line will be obtained when characteristic impedances for even Z_{0e} and odd Z_{0o} mode equal to 71.81Ω and 50.13Ω, respectively. The coupler's coupling factor for each branch should be lower than the main transmission line self-coupling at the operating frequency f_0 (based on considerations conducted in Section 4.1; for the project, the -20dB value was taken). For the coupling branch, the even Z_{0eC} and the odd Z_{0oC} mode are 66.32Ω and 54.28Ω, respectively. The physical model was implemented on 0.508mm height Roggers 4003C laminate ($\epsilon_r = 3.4$) [138]. The differential signal coupler design with -20dB coupling for single branch at 5GHz was carried out using the methodology considered in Section 3.1.2. The coupler was divided into two identical parts and geometrical dimensions of a single part were calculated using the well known methodology for classical microstrip couplers. The width of the single microstrip line w_L is 0.75mm. The calculated spacing between microstrip lines s_L which creates the main transmission line is 0.41mm. The coupler parameters (Fig. 4.20): branch width w_C, line-branch spacing s_C and branch length L_C is 0.78mm, 0.41mm and 9.26mm, respectively. The VNA ports have impedance 50Ω. The transmission line impedance must be transformed to this value. To achieve this goal, the stepped impedance matching circuit which transforms 50Ω to 60Ω was designed [139]. The geometrical dimensions of the model are presented in Tab. 4.3. To take into account the additional matching network, a dedicated calibration kit was prepared (Fig. 4.22a). The prepared loads: OPEN, SHORT, MATCH and THROUGH were used to calibrate the VNA. The matched load which terminates the 60Ω end of the transforming structure for the MATCH calibration kit was realized as a serial connection of the Mini-Circuits 50Ω SMA termination and the Vishay 10Ω resistor (FC series, working to 20GHz). Additionally, the reference transmission line (without a coupler) was released (Fig. 4.22b). Its parameters will be treated as a reference for the models with couplers to identify the impact of the coupler on the transmission line. The practical realization of all PCBs are presented in Fig. 4.22. The prepared models were measured with Vector Network Analyzer (VNA) Agilent N5224A [140] in the frequency band 100MHz-7GHz.

Results

We can observe that both configurations of the coupler (shifted and unshifted) do not significantly affect the transmission line match characteristic for the frequency range below 5.3GHz (the impact is less than 1dB taking into account the dynamic range of match from 0dB to -25dB) (Fig. 4.23a). For frequencies higher than 5.3GHz the impact of unshifted structure is greater (up to 3dB). Additionally, the resonant frequencies for this band are lower (about 100MHz) than for the reference transmission line. The shifted structure does not introduce such distortions. The negligible impact of both coupler configurations on transmission line match for common mode is caused by a slight impact of the coupler's

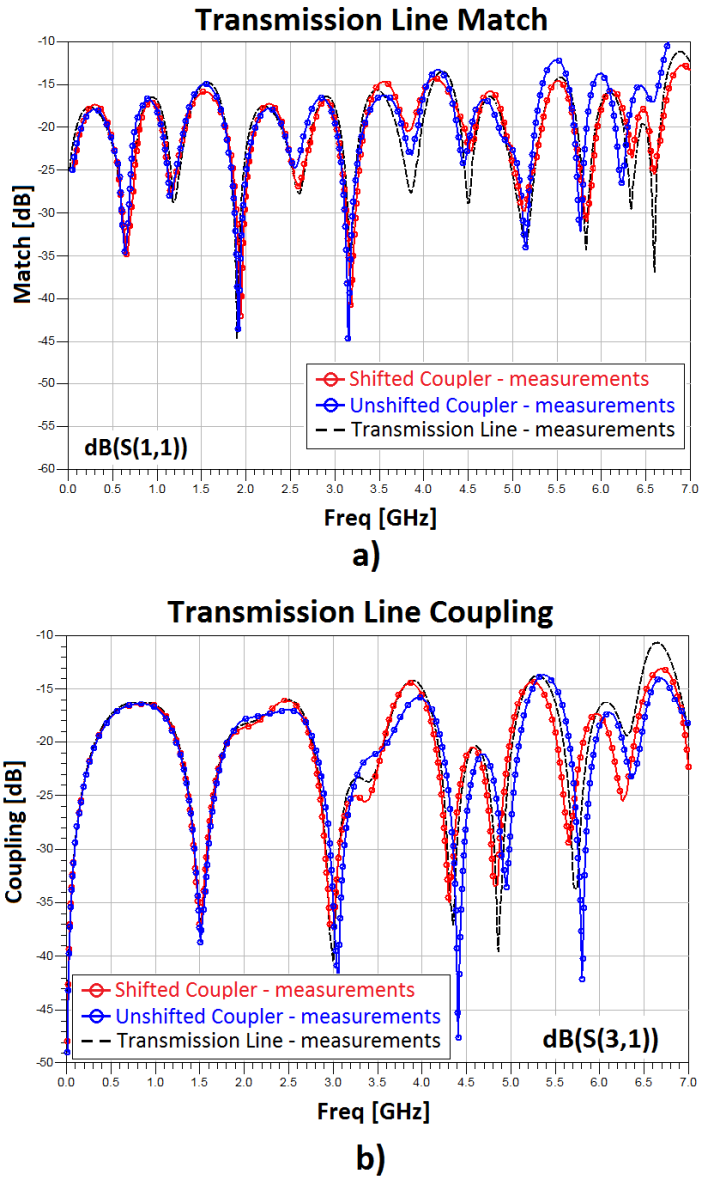

Figure 4.23: 5GHz differential signal coupler measurement results: (a) main transmission line match, (b) main transmission line self coupling

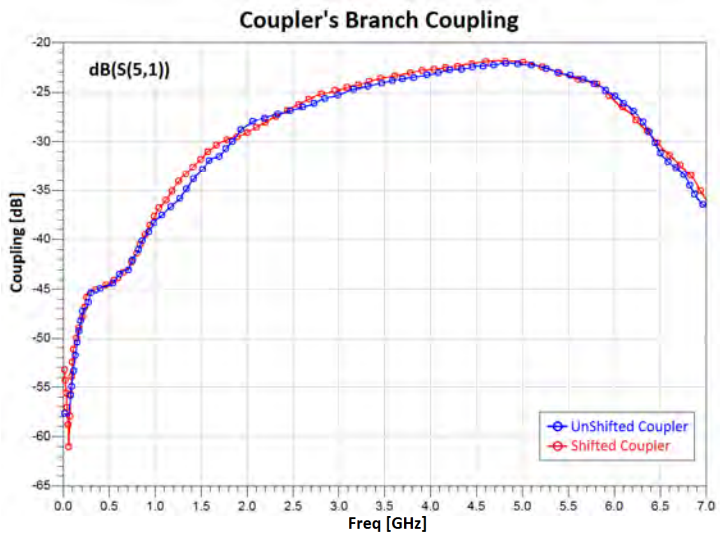

Figure 4.24: 5GHz differential signal coupler measurement results - single branch coupling characteristic

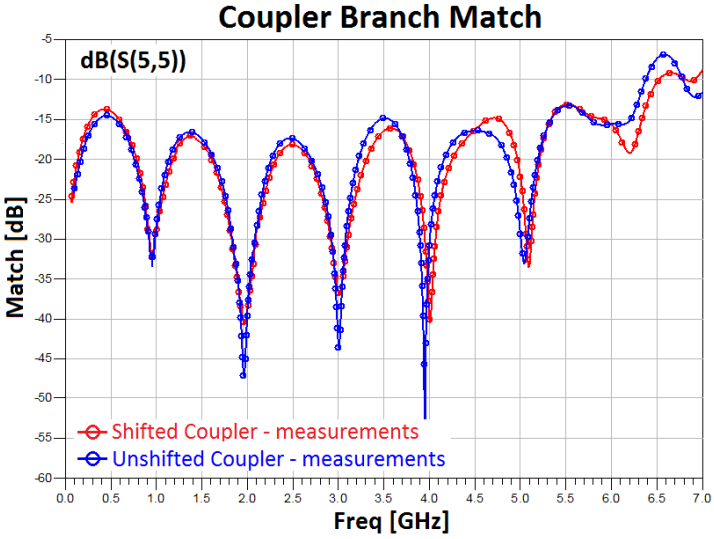

Figure 4.25: 5GHz differential signal coupler measurement results - single branch match

branches on the field distribution in proximity of the coupler from the point of view the main coupled microstrip lines working with even mode and relatively small coupling factor between each microstrip line and the coupler's branch.

The transmission line self-coupling measurement results are presented in Fig. 4.23b. In general, we can see that the impact of the shifted structure on the main transmission line self-coupling characteristic is lower than for the unshifted structure. The first difference is evident in the sub-bands 1.7-2.6GHz and 3.6-4GHz where characteristic for the unshifted structure differs significantly from the shifted structure and the reference line. For band 3.2-3.5GHz, both coupling structures are not consistent with the reference line characteristic. The introduced shifted structure results in lower coupling factor and the unshifted one in higher in comparison to the reference line. The difference for both cases is similar (about 2.5dB). For frequencies higher than 4GHz we can observe that resonances of the structure with unshifted coupler are shifted to higher frequencies (about 100MHz) in comparison to the reference structure. For frequencies higher than 5GHz, the frequency shift towards lower frequencies (from 80 to 120MHz) is visible. The greatest differences in comparison to the reference line appear for frequencies higher than 6GHz for both coupler configurations. Overall, we can conclude that the impact of both coupling structures on the main transmission line can be considered as negligible up to the operating frequency (the 1dB criteria for coupler's impact on the main transmission line match and self coupling characteristic is satisfied for both configurations). Additionally, the experiment proved that the shifted structure introduces smaller disturbance of the main transmission line working condition than the unshifted one. For the shifted configuration, the 1dB criteria is satisfied up to 6.5GHz.

The branch coupling characteristics for both coupler configurations are presented in Fig. 4.24. The achieved coupling factor has local maximum at the operating frequency f_0=5GHz. It equals -21.5dB (-20dB was the value assumed in the design process). The error magnitude (1.5dB) is acceptable at this first attempt. The coupling characteristics for both configurations have similar values in the entire measured frequency range. This is due to the fact that the field distribution between the coupling branch and the closer microstrip line is similar for both configurations. The same situation results in the coupler's branch match characteristics being very similar for the shifted and the unshifted coupler (Fig. 4.25). The coupler's match for frequencies lower than 5.8GHz is -15dB and decreases to -7dB for higher sub-band.

Conclusions

The obtained measurement results show that the proposed concept of the differential signal coupler is correct: while maintaining relatively low coupling factor, the coupler does not affect transmission in the main line. Additionally, the shifted configuration of the coupler has lower impact on the main transmission line self-coupling. The methodology proposed in Section 3.1.2 allows us to design proposed differential signal couplers with good accuracy.

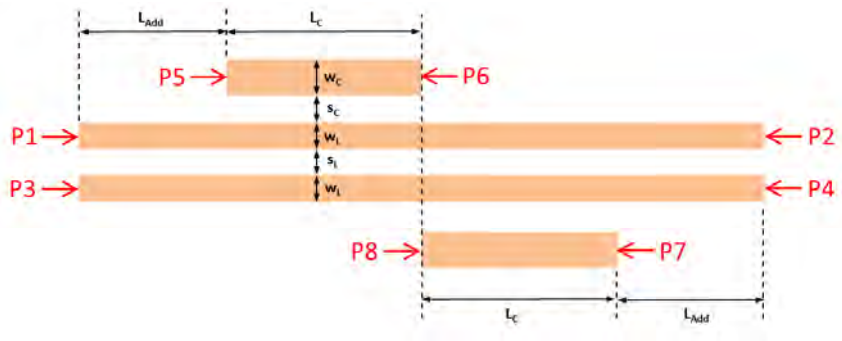

Figure 4.26: The structure of 1GHz differential signal coupler (shifted configuration)

4.3 1GHz differential signal coupler

Overview

The following section describes the simulations and measurement results obtained for a 1GHz differential signal coupler designed with the proposed approach. Using experience gathered from the 5GHz case presented in the previous section, which proves that the shifted coupler's structure has better properties in terms of the minimal impact on the working conditions of the main line, a similar structure was adopted for the 1GHz case. The configuration where the coupler is implemented on the same PCB as the monitored line is compared with the reference transmission line (without a coupler) and the transmission line with two other configurations of couplers, implemented on the separate boards which are overlayed on PCB under test.

Goals

The performed experiments should determine whether the proposed methodology concerning the differential signal coupler can be applied to the design of the couplers overlayed on PCB with the monitored line.

Design

As a target for the coupler design, the main transmission line composed of a pair of coupled microstrip lines with the coupling factor of -15dB at the operating frequency f_0=1GHz was taken. Based on the results obtained in Section 4.1, single coupler's branch coupling factor was taken as -20dB at f_0=1GHz. To simplify the measurement procedure and eliminate impedance transformers which realize impedance matching between the measured model and the VNA port, the characteristic impedance taken for transmission line and coupling branches is 50Ω. The coupler's branch characteristic impedance for even and odd modes

are Z_{0e}=55.28Ω and Z_{0o}=45.26Ω. The transmission line and coupler geometry was calculated for the FR-4 laminate (ϵ_r=4.4, h=1.55mm). The width of a single microstrip line w_L is 2.88mm. The spacing between microstrip s_L is 0.67mm. The differential signal coupler in shifted configuration was designed using methodology presented in Section 3.1.2. The calculated coupler's branch width w_C, branch and line spacing s_C and branch's length l_c is 3.02mm, 1.59mm and 41.33mm respectively. The additional main transmission line elements marked as l_{Add} is 30.2mm.

Simulations

The frequency domain simulations were performed with full wave EM Solver Ansys HFSS v10 [141, 142]. The simulation results compared to parameters obtained for reference transmission line without a coupler are presented in Figs. 4.27 and 4.28.

We can see that in the 100MHz-1.6GHz band, the transmission line match for the structure with the differential signal coupler is not degraded (Fig. 4.27a). For the sub-band 1.6GHz-1.85GHz, the 30MHz shift of resonant frequencies is observed. A similar situation takes place for the 2.2GHz-2.4GHz sub-band. For frequencies higher than 2.4GHz we can see an amplitude error defined as the difference between the amplitude characteristic of the reference line and the line with the coupler (to 2.5dB). The self-coupling characteristic of the main transmission line is presented in Fig. 4.27b. The differential signal coupler has negligible impact on the main transmission line self-coupling for frequencies lower than 1.9GHz. For higher band, the self-coupling characteristic differs from the characteristic of the reference transmission line (about 2dB in amplitude). For frequencies higher than 2.8GHz, the resonant frequencies for configuration with the coupler are shifted to higher frequencies (about 100MHz) in comparison to the reference transmission line. The characteristic of loss in the main transmission line for case with and without coupler is presented in Fig. 4.28b. The graph shows that the coupler has no influence on the loss characteristic in the main transmission line below 2GHz. For higher frequencies, the transmission loss increases successively. The transmission loss for the configuration with the coupler is 0.2dB higher at 2.6GHz and 1dB higher at 4GHz. The characteristic of the coupler's single branch coupling is presented in Fig. 4.28a. The single branch coupling factor at the operating frequency f_0=1GHz is -19dB (the desired value was -20dB). From the practical point of view the error at the level of 1dB can be considered as satisfactory.

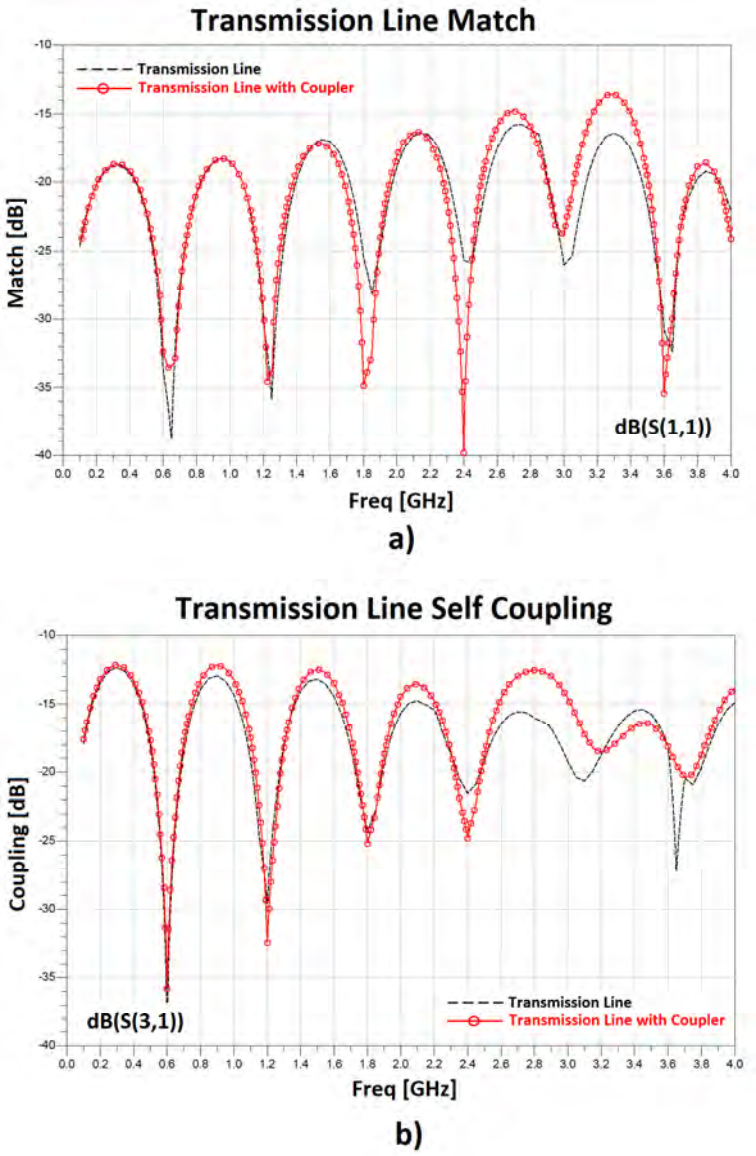

Figure 4.27: Simulation results for 1GHz differential signal coupler (shifted structure) performed on FR4 laminate (h=1.55mm) vs the reference transmission line without the coupler: (a) main transmission line match, (b) main transmission line self coupling

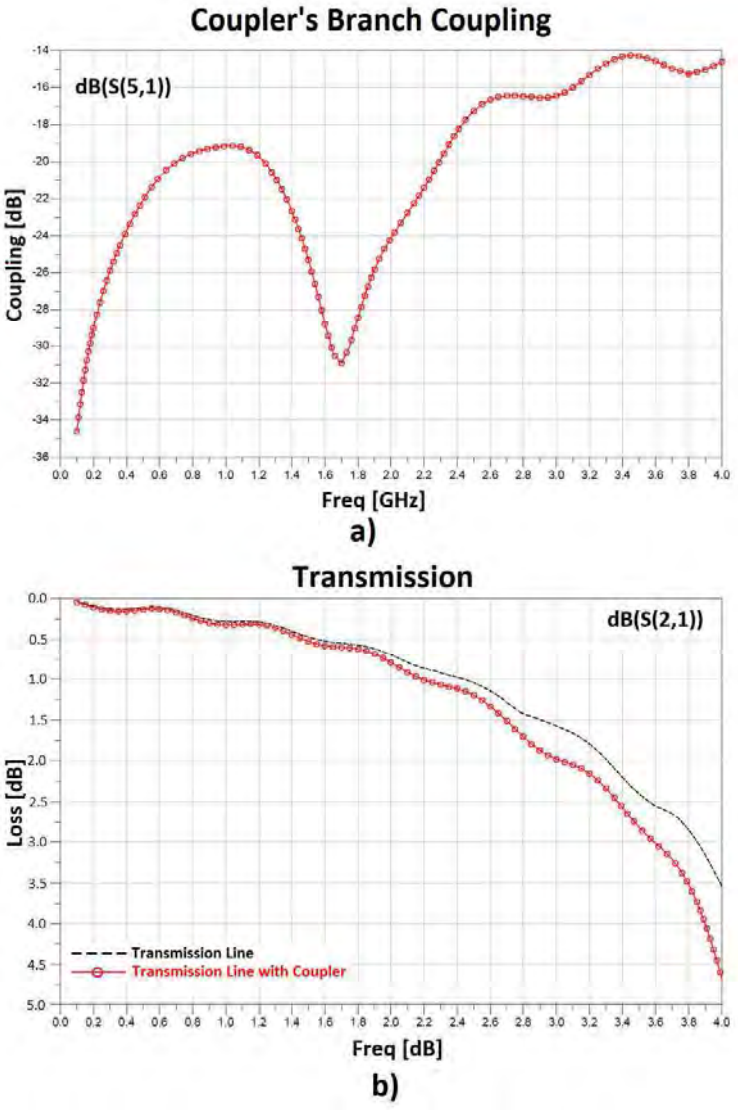

Figure 4.28: Simulation results for 1GHz differential signal coupler (shifted structure) performed on FR4 laminate (h=1.55mm) vs the reference transmission line without the coupler: (a) coupler's single branch coupling, (b) transmission loss in main line

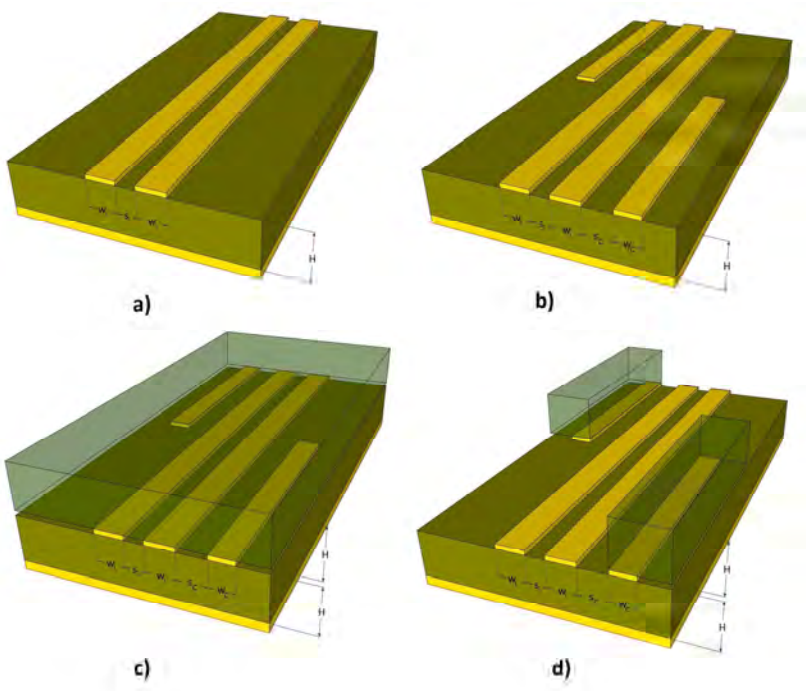

Figure 4.29: Four configurations of PCBs realized to verify the design of the 1GHz differential signal coupler: (a) the reference main transmission line, (b) the main transmission line with differential signal coupler (shifted configuration) implemented on the same board as transmission line, (c) the coupler implemented on the separate board which is overlayed on PCB with the main transmission line, (d) the coupler is implemented on the two separate boards which are overlayed on PCB with the main transmission line

Measurements

The next step is to verify the obtained simulation results through physical model measurements. The measurements were made using three coupler configurations: (1) the coupler is realized on the same PCB as the transmission line (Fig. 4.29b - the same case was considered in simulation approach), (2) the coupler is implemented on a separate PCB which is overlayed on the transmission line (Fig. 4.29c), (3) the coupler is realized on two small pieces of PCB overlayed on the board with the main line (Fig. 4.29d). The configuration (1) should verify the design methodology in terms of the obtained parameters and refer it to the results obtained by simulations previously. Models (2) and (3) should determine the impact of the additional dielectric layer overlayed on PCB with the main line on the working conditions of the main transmission line. This experiment can be

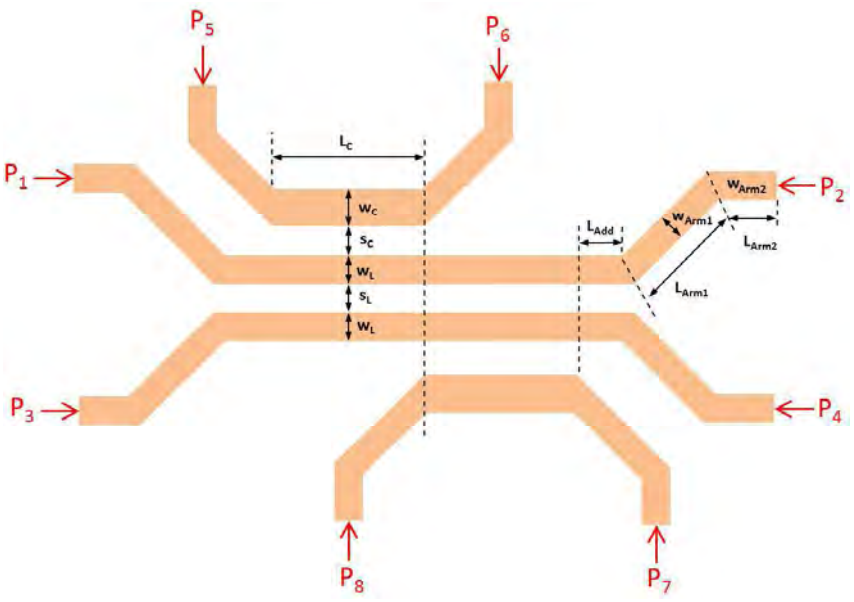

Figure 4.30: The PCB diagram for the 1GHz differential signal coupler model

Table 4.5: Geometrical dimensions of the 1GHz differential signal coupler (shifted structure)

Dimension	**Value [mm]**
w_L	2.88
s_L	0.67
w_C	3.02
s_C	1.59
L_C	41.33
L_{Add}	30.00
w_{Arm1}	2.97
L_{Arm1}	30.00
w_{Arm2}	2.97
L_{Arm2}	13.00

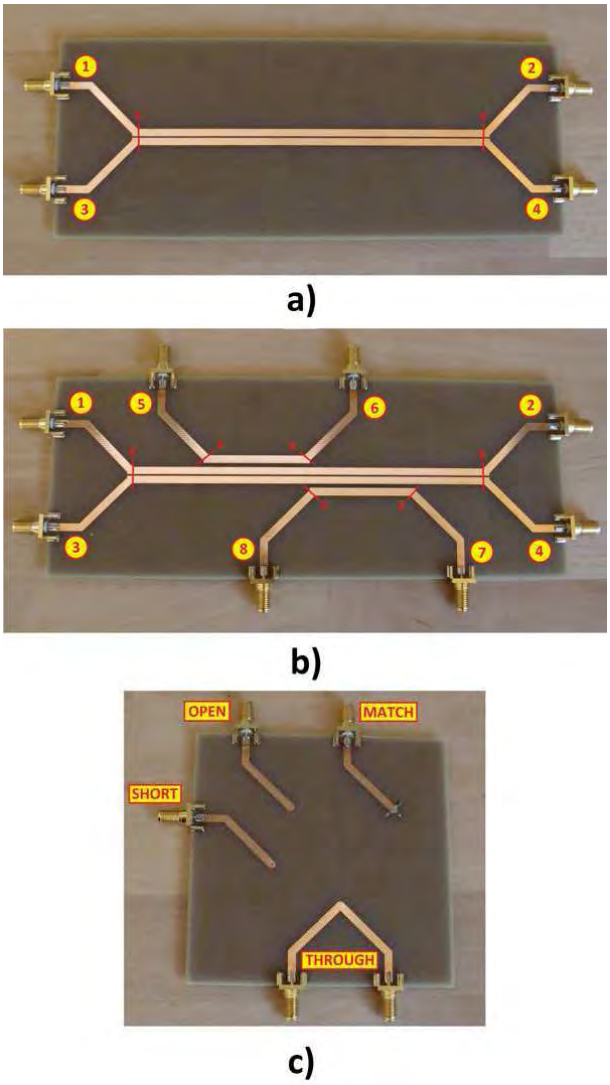

Figure 4.31: The model of the 1GHz differential signal coupler: (a) reference transmission line, (b) transmission line with differential signal coupler (shifted configuration), (c) VNA calibration kit

considered as a feasibility study of the coupler which could be realized on separate PCB and overlayed on the board under test to probe signals transmitted in the main transmission line. All results are compared to the reference transmission line without a coupler. The geometrical dimensions of the transmission line and the coupling branches are the same as for the previous simulations. The diagram of the prepared PCB is shown in Fig. 4.30. The dimensions of the lines are listed in Tab. 4.6. The differential signal coupler is implemented along the middle part of the line. All ports (transmission line and coupler) are extended to the edge of PCB with 50Ω microstrip lines (each extension line has the same geometry). A special calibration kit was prepared which allows us to compensate the extension lines in the measurements (Fig. 4.31c). The measurements of physical model were performed with Vector Network Analyzer (VNA) Agilent ENA E5071C [143] in the frequency band 50MHz-4GHz.

The amplitude characteristic of the transmission line match for all measured configurations is presented in Fig. 4.32. We can observe that for the configurations presented in Fig. 4.29b and Fig. 4.29d, the coupler does not substantially affect the match of the main transmission line (the parameters are related to the transmission line without coupler - Fig. 4.29a). The error defined as the difference between the stand-alone transmission line match characteristic and the line with the coupler is not grater than 1dB in the frequency band of 300MHz to 1.9GHz. For higher frequencies the error increases to 3dB in some sub-bands. Additionally, the shift of resonant frequencies is visible (difference about 50MHz). The match characteristic for the reference line is better than the results obtained by simulations (-19dB to -17dB for simulation vs -25dB to -20dB for band up to 1.6GHz). This effect is a result of the fact that the laminate used in the physical model has higher loss than the values recommended for the design in the FR4 datasheet [144]. This is a common occurrence because FR4 laminate is produced with relatively high level of dispersion of the production parameters [144, 145]. The situation is different in the case of configuration shown in Fig. 4.29c. The additional part of the laminate overlaied on the main transmission line significantly affects the main transmission line match characteristic (the amplitude error is up to 10dB and the resonant frequencies are shifted up to 400MHz). The part of the laminate under the main line causes the local change in the effective dielectric permittivity of the coupled microstrip lines in the coupler's neighborhood. The phase chatacteristic of the transmission line match is presented in Fig. 4.33. As in the case of the amplitude characteristics, the phase characteristics for configurations Fig. 4.29b and Fig. 4.29d have similar shape as the reference transmission line, but up to 2.65GHz. The configuration in Fig. 4.29c has 180° transition points shifted to lower frequencies (by about 100MHz) for the band above 1.8GHz. The main line self coupling amplitude characteristic is presented in Fig. 4.34. We can see high level of compliance characteristics obtained for configurations from Fig. 4.29b and Fig. 4.29 with reference transmission line up to 1.8GHz. Additionally, the obtained results are highly in line with the simulation results (Fig. 4.27b) up to 1.8GHz. Above this frequency, some additional

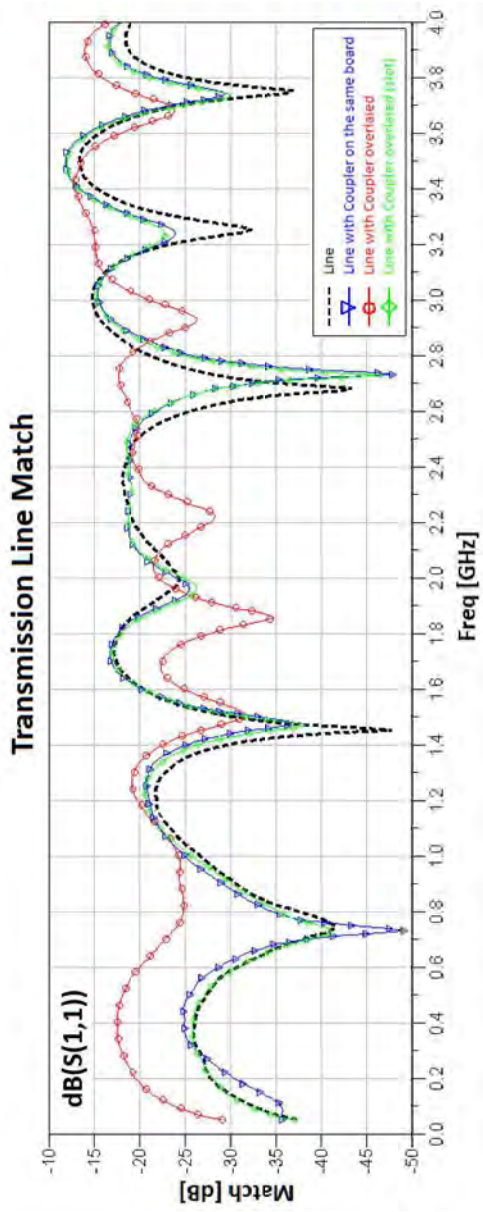

Figure 4.32: Transmission line match - amplitude characteristic (measurements)

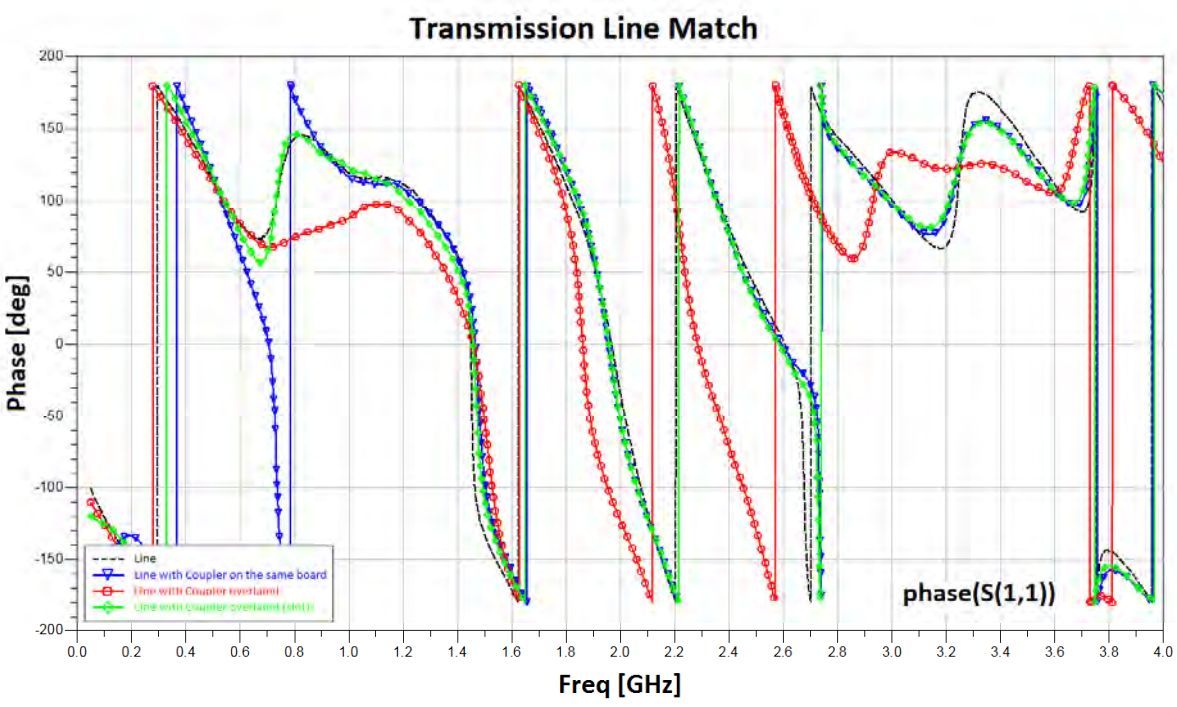

Figure 4.33: Transmission line match - phase characteristic (measurements)

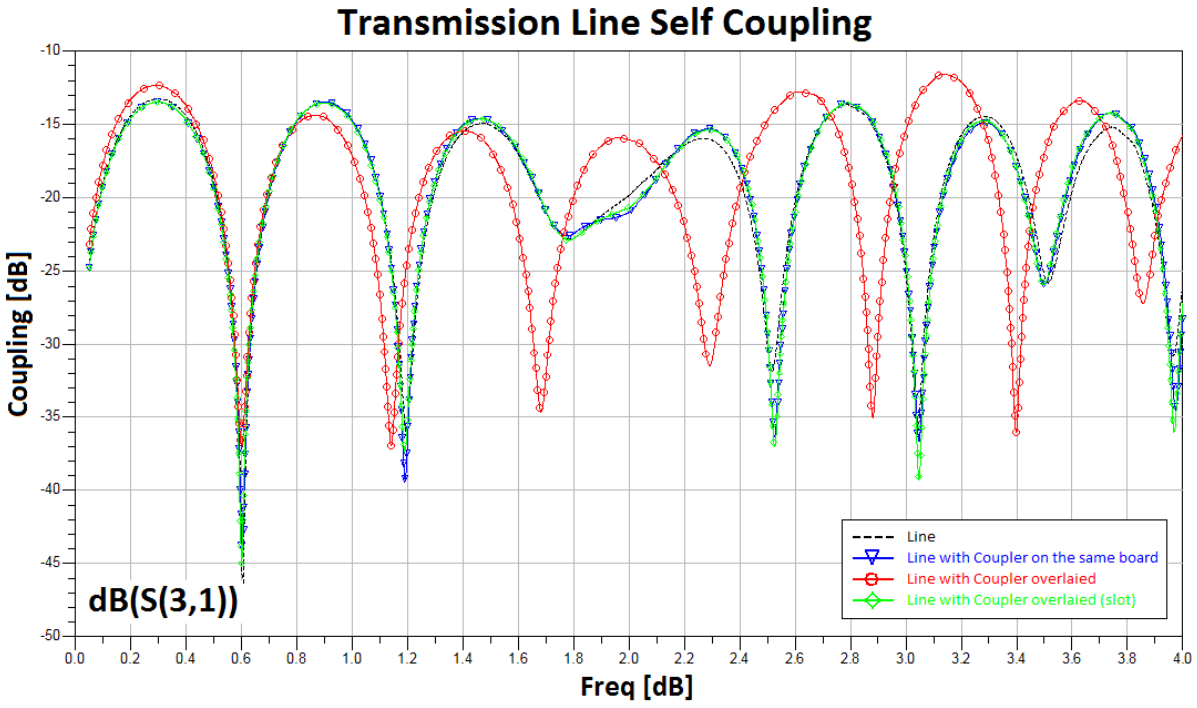

Figure 4.34: Transmission line self coupling amplitude characteristic (measurements)

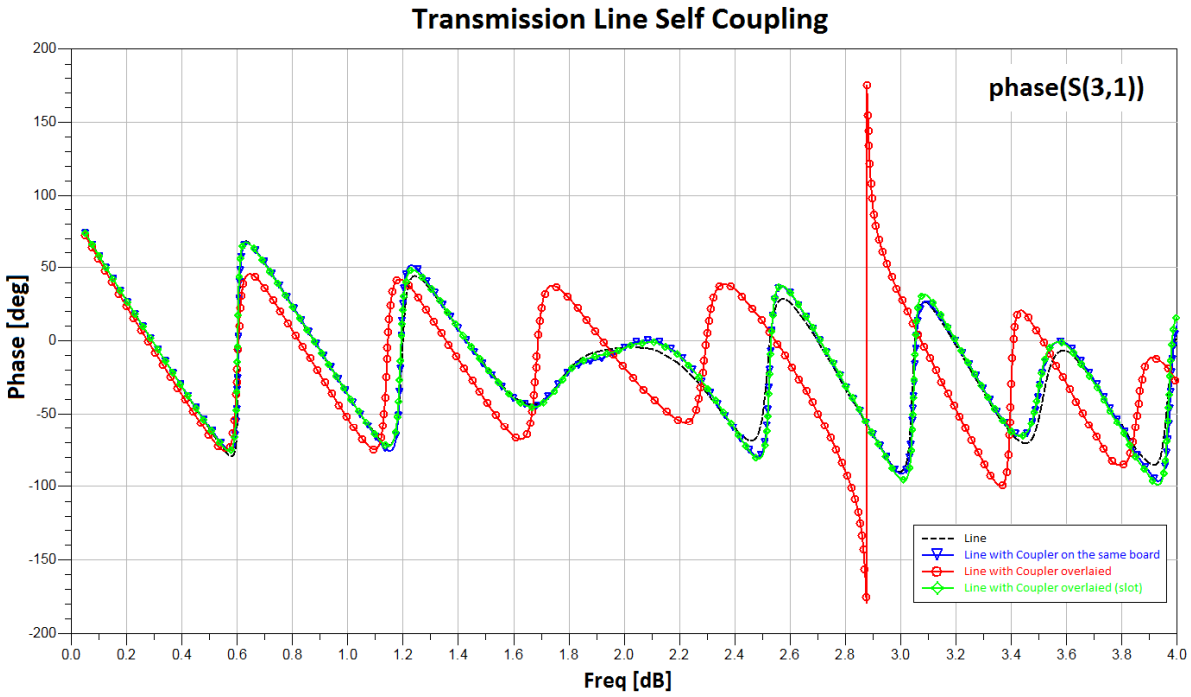

Figure 4.35: Transmission line self coupling phase characteristic (measurements)

resonances are observed in measurements which are caused by physical construction of the model. The error defined as a difference between the amplitude characteristic of the transmission line with the coupler (Fig. 4.29b and d) and the reference transmission line (Fig. 4.29a) obtained by measurements is significantly lower above 1.8GHz (up to 1dB in sub-bands 1.9GHz-2.4GHz 3.6GHz-3.85GHz) than for simulation (up to 2.5GHz and some frequency shifts in resonant frequencies up to 100MHz). For configuration in Fig. 4.29c, the self-coupling characteristic significantly differs from the parameters of the reference line (amplitude error up to 7dB and some frequency shifts for resonant points up to 250MHz). For phase characteristics obtained for the transmission line self-coupling, the observations are similar regarding the amplitude characteristics: configurations from Fig. 4.29b and Fig. 4.29d have phase characteristics fully in line with the reference line (Fig. 4.35). The main transmission line loss amplitude and phase characteristics are presented in Fig. 4.36 and Fig. 4.37, respectively. The amplitude of transmission in the main line is not disturbed by adding the differential signal coupler with configurations Fig. 4.29b and Fig. 4.29d. The loss factor from measurements has higher value than that obtained from simulations. For configuration in Fig. 4.29c, the effective dielectric permittivity in coupler's neighborhood is changed, which results in significantly lower loss level (2dB better at 3GHz). Due to this, the phase characteristic is successively moved to lower frequencies in relation to the reference line. The single coupler's branch coupling characteristic is presented in Fig. 4.38. A desired level of coupling factor -19.5dB at the operating frequency f_0=1GHz was obtained for configurations in Fig. 4.29b and Fig. 4.29d (this value is closer to the design specifications of -20dB than the coupling factor obtained in simulations, -19dB). The configuration in Fig. 4.29c gives -18dB of coupling at the operating frequency and the resonant frequency was shifted by 150MHz to lower frequencies referring to other configurations. Additionally, we can observe that the measured single branch coupling characteristic is flatter than the simulated one. The coupler's branch match characteristic is presented in Fig. 4.39. The coupler's match at the level -18dB for configurations in Fig. 4.29c and Fig. 4.29d can be considered as satisfactory for practical applications. The single branch isolation characteristic is presented in Fig. 4.40. We can observe a high level of compliance for configurations in Fig. 4.29b and Fig. 4.29d. The value of isolation at the operating frequency (f_0=1GHz) at the level -23dB is relatively low in comparison with the value of the single branch coupling factor (-20dB). The measured isolation is significantly higher for Fig. 4.29c configuration (-35dB at 1GHz).

Conclusions

The simulation results prove that the designed differential signal coupler does not significantly disturb the working conditions of the main transmission line for frequencies lower than 1.6GHz. Based on this fact, we can confirm that, in terms of disturbing the transmission in the main line, the proposed configuration of the differential signal coupler can be used to probe the signals from the main line for

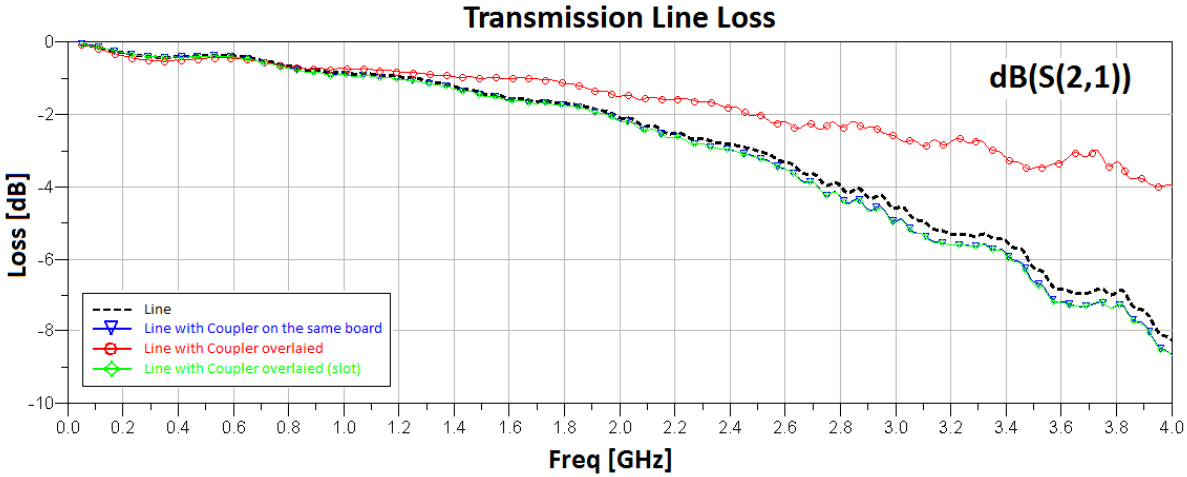

Figure 4.36: Main transmission line loss characteristic (measurements)

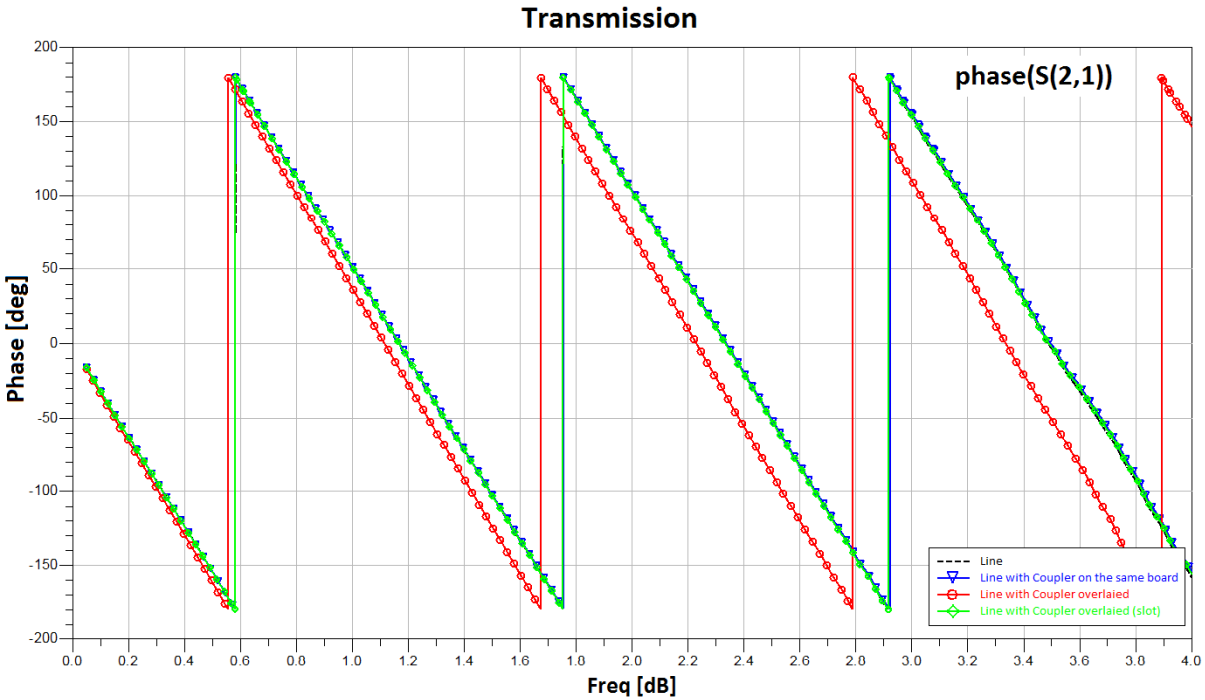

Figure 4.37: Main transmission line loss phase characteristic (measurements)

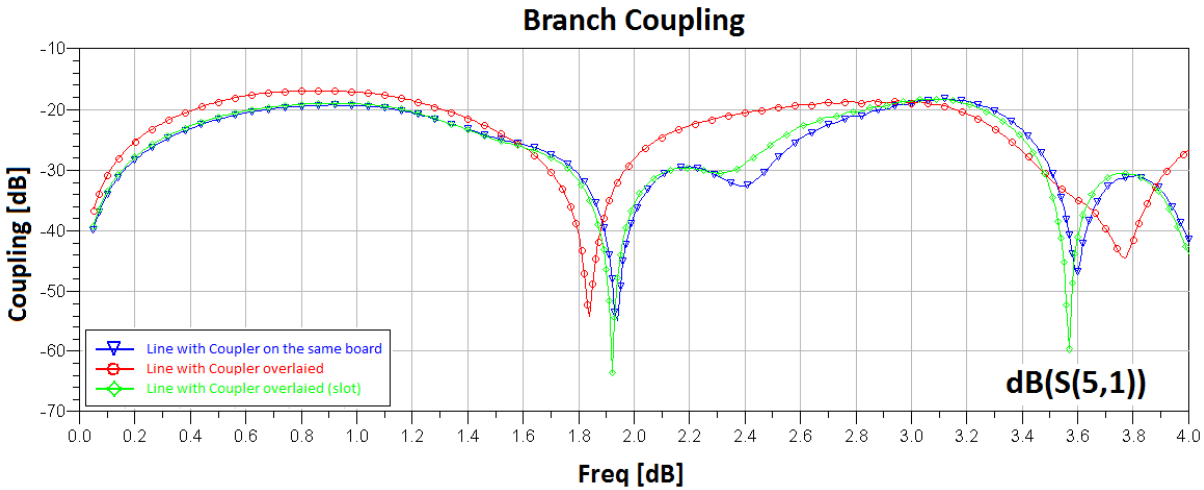

Figure 4.38: Single branch coupling characteristic (measurements)

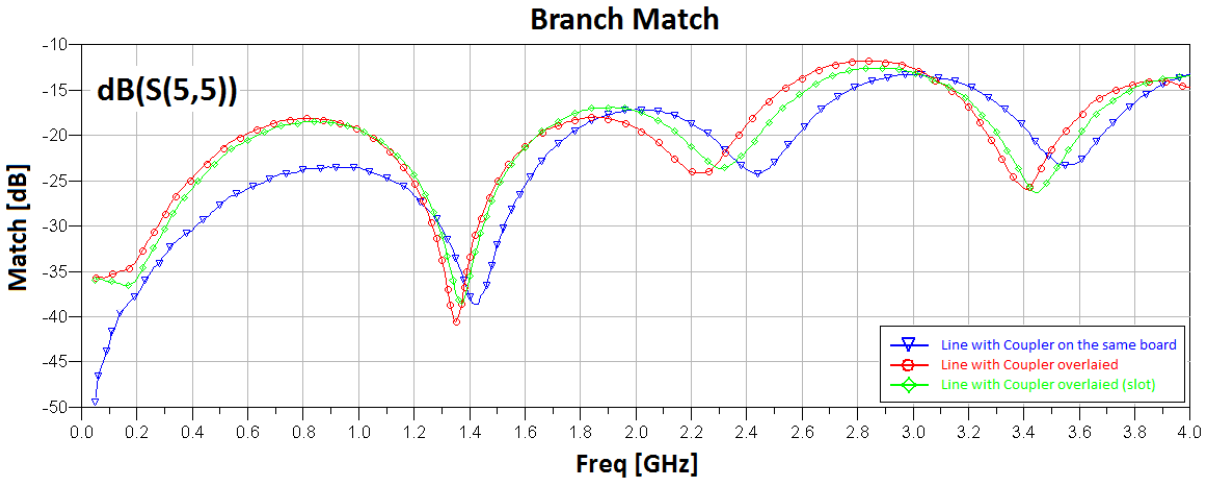

Figure 4.39: Single coupler's branch match (measurements)

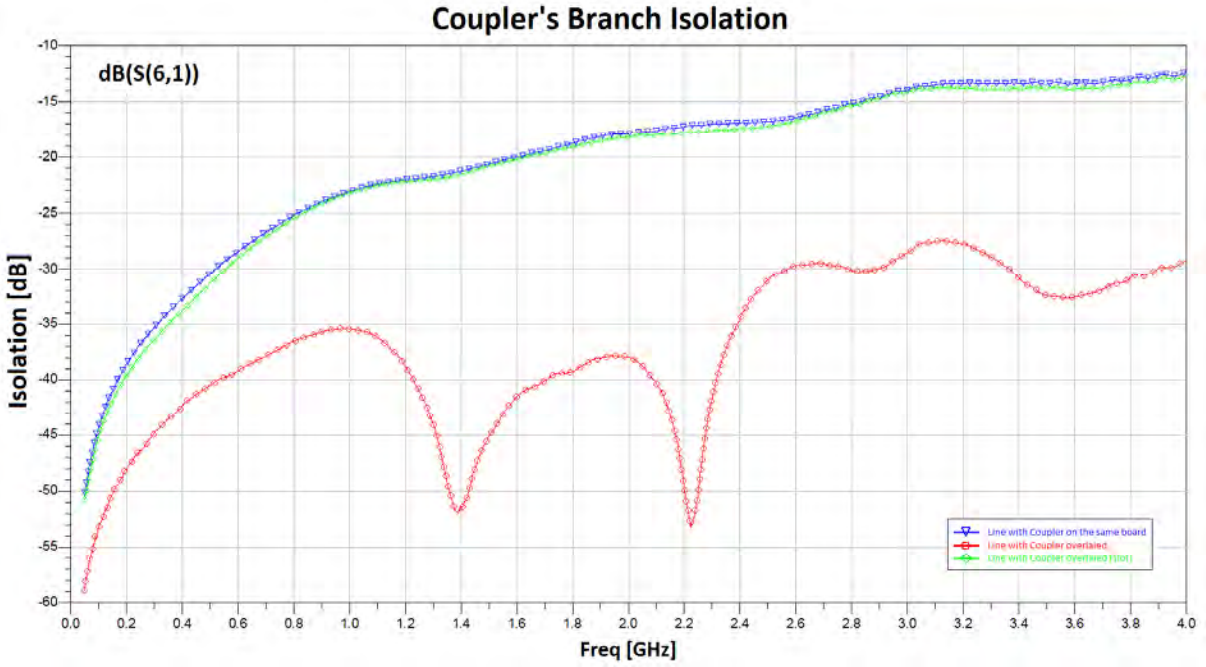

Figure 4.40: Single coupler's branch isolation (measurements)

measurement purposes. Additionally, it was shown that the proposed design methodology allows obtaining a desired coupling factor at a given operating frequency.

The measurement results discussed above indicate the correctness of the proposed design methodology. They are in excellent agreement with simulations up to 1.8GHz (the operating frequency is f_0=1GHz). Above this frequency, we observe some differences which are caused by the additional parasitic elements present in the physical model which were not included in the simulations. The numerical model used in simulations seems to be sufficient to design a differential signal coupler for operating frequencies up to 1.8GHz.

Additionally, it was shown that it is possible to implement the designed coupler's branch on two separate pieces of PCB and overlay it on the PCB containing the main transmission line (configuration in Fig. 4.29d) without disturbing transmission in it. The measurements have shown the low isolation (caused by poor directivity) for the coupler configurations which do not disturb significantly the main line working conditions. The level of isolation at the operating frequency is close to the coupling factor. Thus, low directivity is not sufficient for measurement probing where the distinguishing between the signals from the main line propagating from a given direction is particularly important. In the following sections, the practical method of coupler's directivity improvement will be presented.

4.4 1GHz optimized differential signal coupler

Overview

As shown in the previous section, directivity of the differential signal coupler is relatively poor (isolation is very close to the coupling factor). Directivity is a key parameter in terms of ability to distinguish the signals transmitted in each direction through the main transmission line. This section describes the coupler's directivity optimization process which is applied to differential signal coupler designed and measured in Section 4.3. The coupler's high directivity should increase the time resolution of the transmission monitoring. Apart from the simulations, the measurements were performed as well. The results are compared with data obtained in Section 4.3 for non-optimized version and the reference transmission line.

Coupler's directivity optimization

To improve the coupler's directivity, the methodology described in [133] and quoted in Section 3.2.2 was adopted. The results presented so far confirm that the design methodology based on dividing full differential signal coupler structure into two parts and the use of well known design relations for classical microstrip proximity couplers is correct. Directivity optimization can be therefore performed in a similar way: only single branch of the differential coupler will be used in the optimization procedure. The results will be applied to both parts of the coupler.

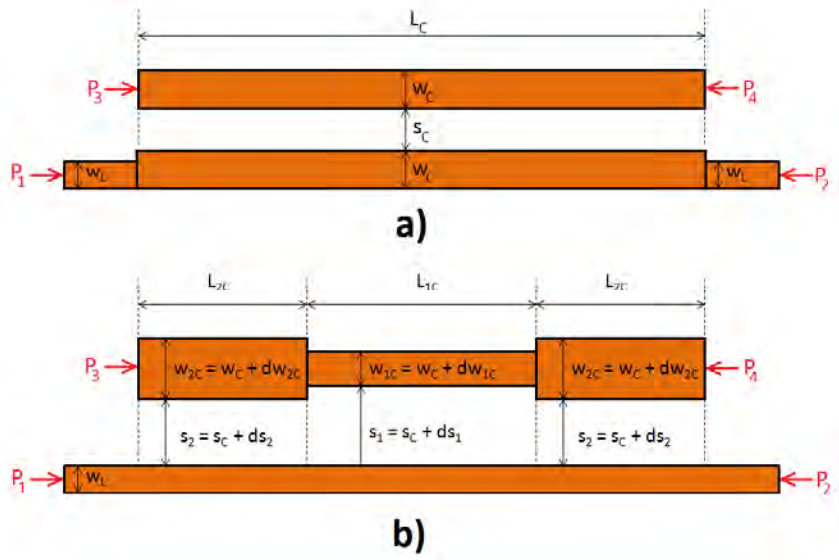

Figure 4.41: Parametrized single branch of differential signal coupler for directivity optimization

The methodology described in [133, 134] and presented in Section 3.2.2 is based on the step impedance change of both lines which are mutually coupled. In our case, this methodology can not be applied directly. The differential signal coupler for signal probing assumes that one of the coupled lines represents a coupler's branch whereas the second represents a single line from the monitored transmission line. In Muller's methodology [133] the widths of both coupled lines are modified. From the application point of view, if we want to implement a differential signal coupler on separate parts of the laminate and overlay them on the board with the main transmission line to probe signals transmitted in it, modification of the main transmission line dimensions is not possible. The only option is to modify the dimensions of the coupler's branch. The initially designed coupler with analytical relations described in Section 4.3 was parametrized as shown in Fig. 4.41. The three-section structure was assumed. The design optimization goals are shown in Fig. 4.42 and Fig. 4.42. From the measurement point of view, considering the isolation is more intuitive than directivity. The isolation I is clearly associated with the directivity D as a sum of the directivity D and the coupling factor M. In our case, the coupling factor M is invariable so we can conclude that isolation depends only on directivity. It was assumed that the goal for coupler's isolation is -35dB. This value has been adopted based on the measured isolation for the configuration presented in Fig. 4.29c. This level of isolation should be obtained while maintaining other significant parameters at the satisfactory level around the operating frequency: main line match -30dB,

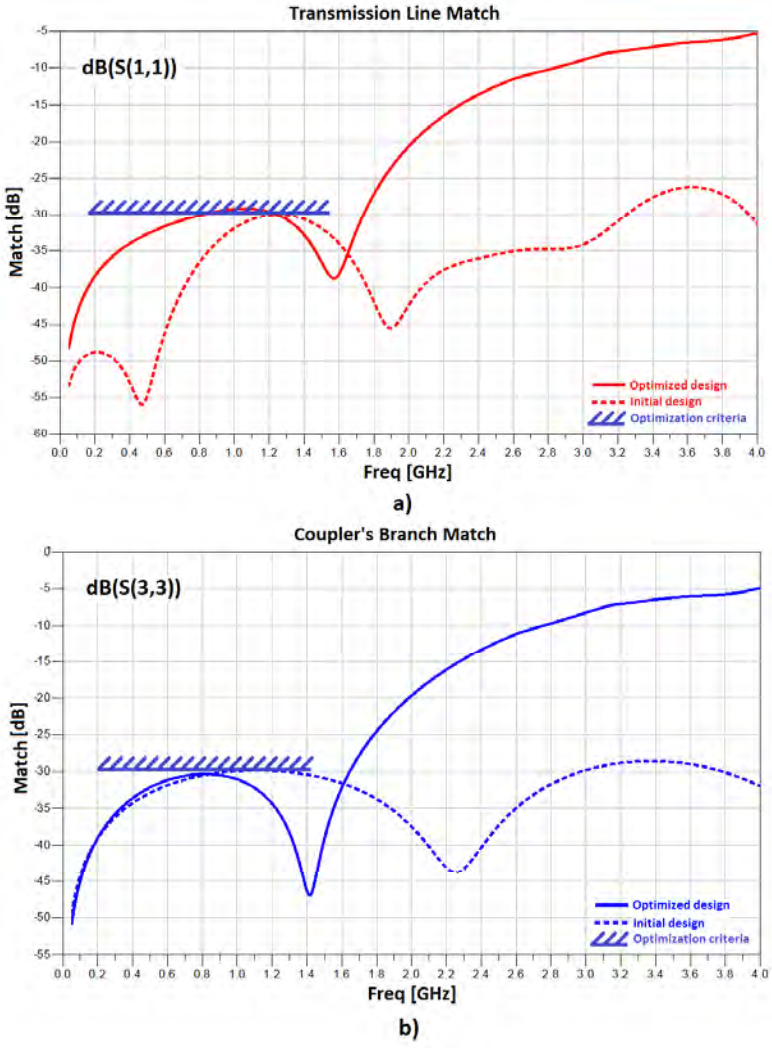

Figure 4.42: 1GHz differential signal coupler optimization goals: (a) main transmission line match, (b) single coupler's branch match

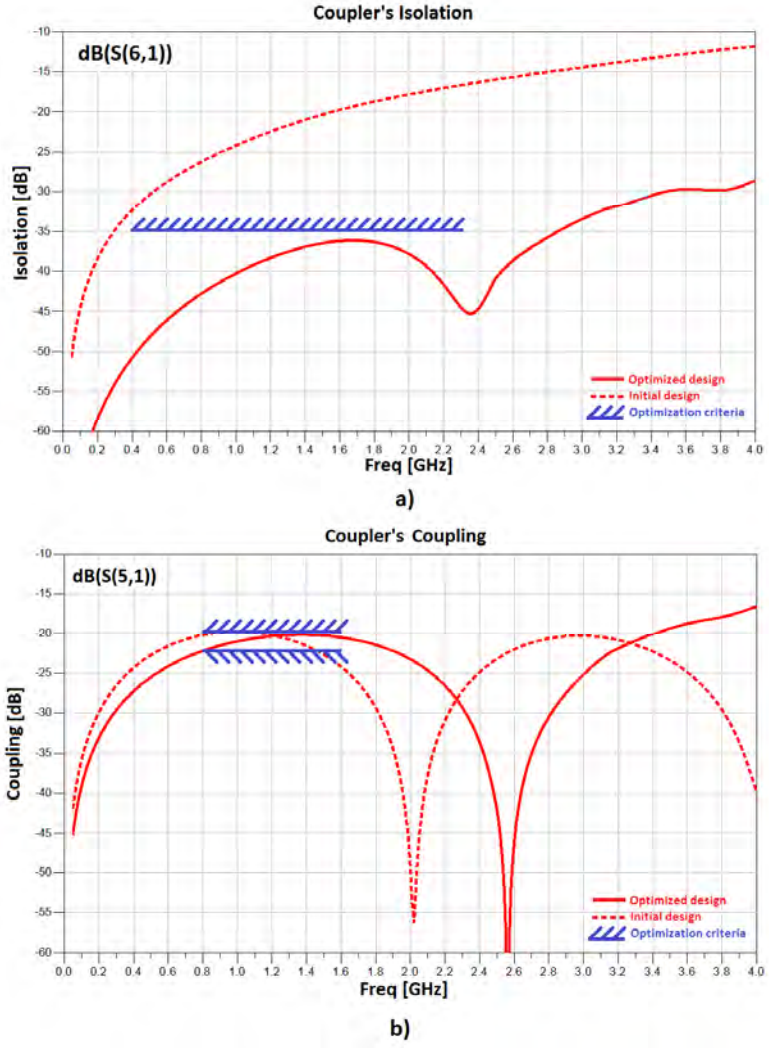

Figure 4.43: 1GHz differential signal coupler optimization goals: (a) single coupler's branch isolation, (b) single coupler's branch coupling

the coupler's branch match -30dB, the branch coupling factor in the range -18dB to -22dB. It is also assumed that the optimized structure can not be longer than the initial one. The optimization was performed using the Quasi-Newton algorithm built in Agilent ADS. The Quasi-Newton search method uses second-order derivatives of the error function as well as its gradient to find a descend direction [146]. The second order derivatives are estimated by the Davidson-Fletcher-Powell update formula [147].

Simulations

After optimization, the coupler's isolation was increased from -28dB to -40dB at f_0 =1GHz (for lower frequencies the isolation is better). The improvement of directivity did not result in deterioration of other important parameters (coupler's match, transmission's line match, coupling factor). Furthermore, the total length of the coupler branch was reduced from L_C=41.33mm to 29.7mm. As suggested in [134], the length of each section is equal after optimization. The geometrical dimensions of optimized coupler are as follows: w_{1C}=0.67mm, w_{2C}=6.24mm, s_1=4.92mm, s_2=0.67mm, L_{1C}=9.9mm, L_{2C}=9.9mm (the symbols are consistent with those shown in Fig. 4.41b). The optimized differential signal coupler was simulated with Ansoft HFSS v10. The results are presented in Fig. 4.44, Fig. 4.45, Fig. 4.46, Fig. 4.47 and Fig. 4.48. The isolation significantly increased (Fig. 4.44) - at the coupler's operating frequency f_0=1GHz it has a value of -40dB. Additionally, in the neighborhood of this operating frequency, the isolation characteristic is more flat than for the non-optimized version. Achieving high level of isolation is not obtained at the expense of other important parameters in the operating band. The amplitude characteristic of the transmission line match is presented in Fig. 4.45. The optimized version of the coupler has the main transmission line characteristic in line with the initial coupler's structure and the reference line up to 1.3GHz. Above this frequency, in the 1.3GHz-1.65GHz sub-band, it decreases by 2dB. The next mismatch increase is visible (up to 7dB) in the sub-band 3.25GHz to the end of the measurement range (4GHz). The main transmission line self-coupling characteristic and loss in the main transmission line is presented in Fig. 4.46 and Fig. 4.47, respectively. The obtained simulation results indicate that the characteristics are identical with the initial, non-optimized coupler case. These results show that the optimized structure of the differential signal coupler has similar impact on the main transmission line working conditions as the initial coupler's structure designed using the methodology presented in Section 3.2.1. The single branch coupling characteristic is shown in Fig. 4.48. The desired coupling factor at operating frequency f_0=1GHz is -19dB (the same value as obtained for the initial coupler's structure). Overall coupling characteristic is very similar to the characteristic of the initial coupler's structure. The results obtained through simulation show that it is possible to optimize the structure of the differential signal coupler by modifying the coupler's branch impedance (step-impedance configuration), and to obtain higher directivity without significant deterioration of other important parameters (such

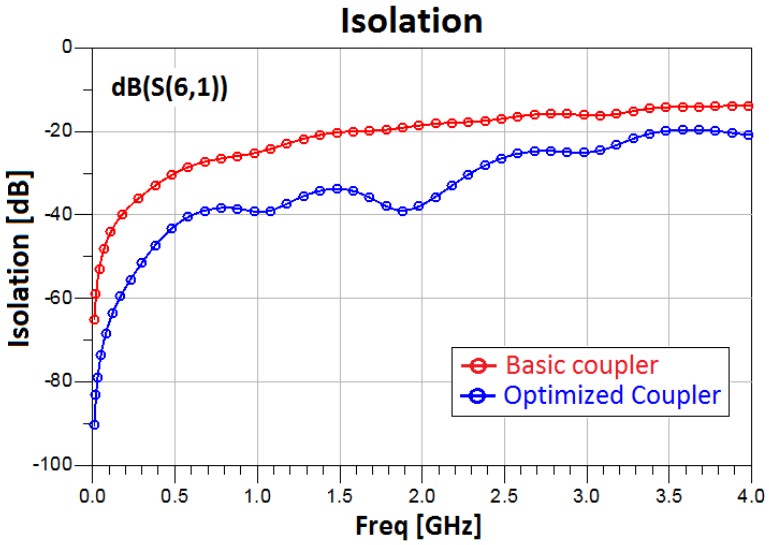

Figure 4.44: 1GHz differential signal coupler optimization results (simulation): single coupler's branch isolation

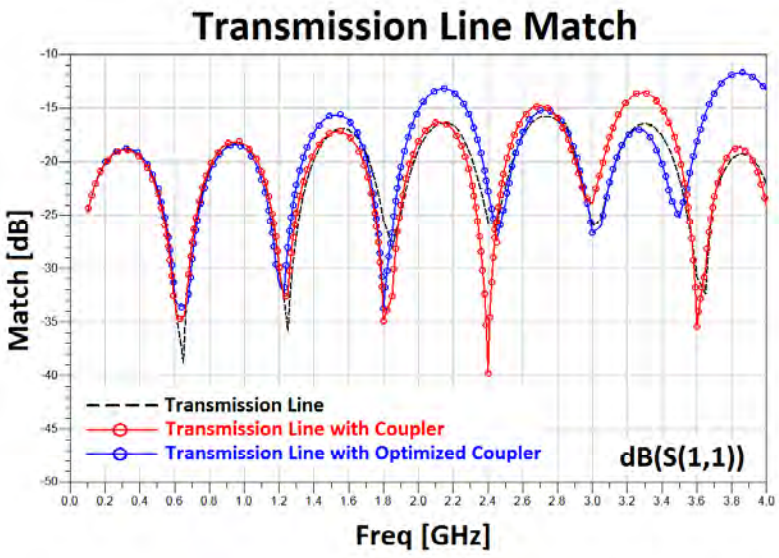

Figure 4.45: 1GHz differential signal coupler optimization results (simulation): main transmission line match

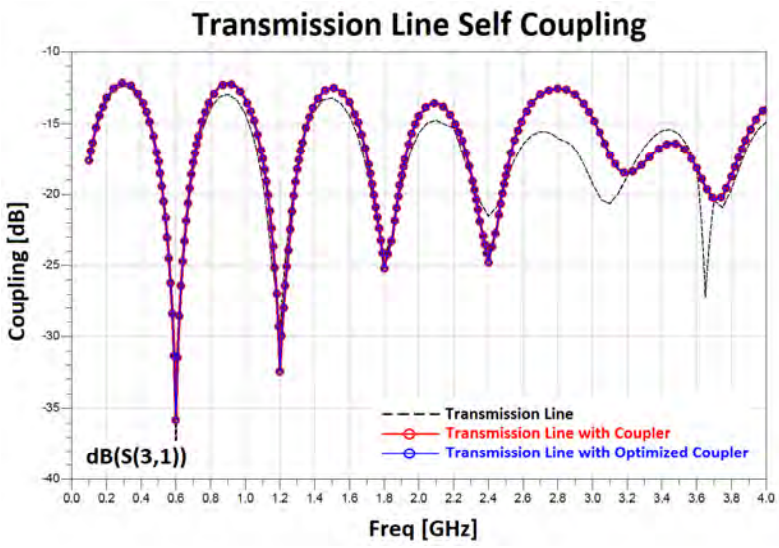

Figure 4.46: 1GHz differential signal coupler optimization results (simulation): main transmission line self coupling

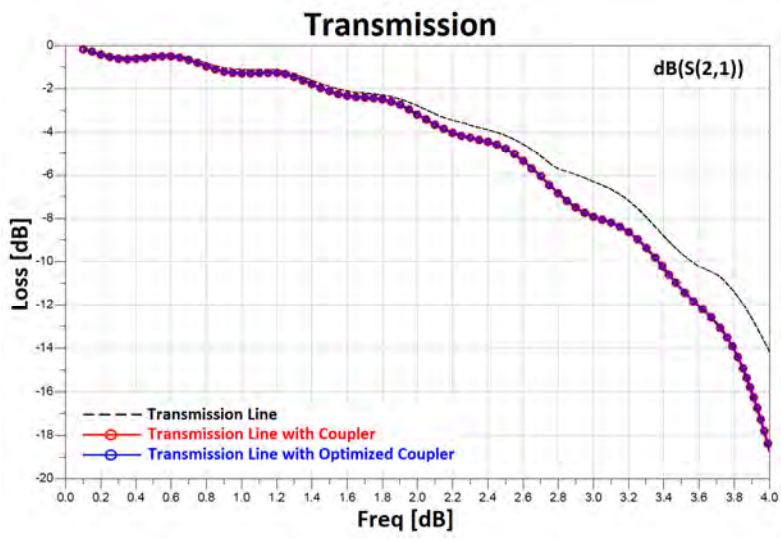

Figure 4.47: 1GHz differential signal coupler optimization results (simulation): main transmission line loss characteristic

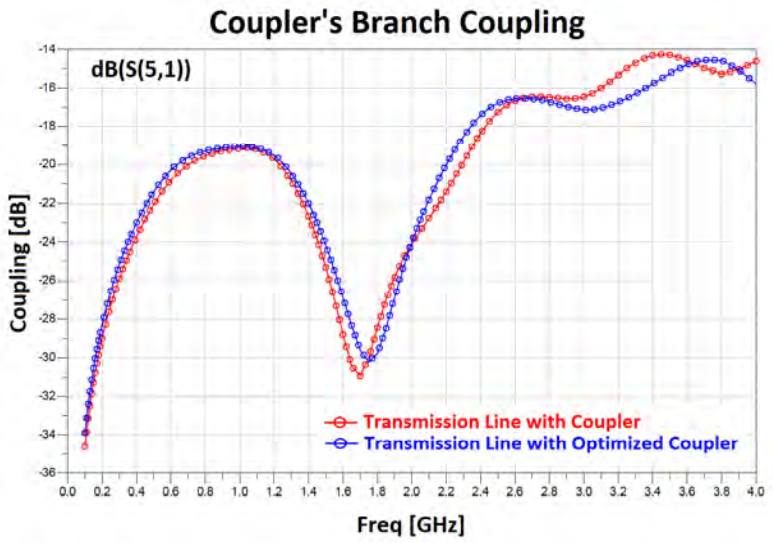

Figure 4.48: 1GHz differential signal coupler optimization results (simulation): single coupler's branch coupling

as impact on the main transmission line working conditions or decoupling characteristic) in the assumed operating band. The coupler's directivity is crucial for some applications (like contact-less signal probing from differential transmission).

Measurements

The next step is to measure the physical model of the optimized coupler and to compare the obtained results with the reference transmission line and with the initial structure of the coupler. The dimensions of physically realized model are presented in Fig. 4.49. The physical realization of the optimized differential signal coupler is shown on Fig. 4.50c. All measurements were performed using the Agilent Vector Network Analyzer (VNA) E5071C [143] in the frequency band 50MHz-4GHz. To compensate for the impact of the auxiliary transmission lines (L_{Arm1} and L_{Arm2}), the dedicated calibration kit was used to calibrate VNA (the same as in measurements described in Section 4.3 - Fig. 4.31c). The measurement results are presented in Fig. 4.51, Fig. 4.52, Fig. 4.53, Fig. 4.54, Fig. 4.55, Fig. 4.56, Fig. 4.57 and Fig. 4.58. All results are compared with the parameters of reference transmission line and the line with non-optimized version of the coupler. We can observe that the main transmission line match characteristic for the optimized coupler configuration agree with the non-optimized one up to 1.8GHz (Fig. 4.51). The most significant differences are visible in the sub-band 750MHz-900MHz. For the optimized coupler configuration the transmission line characteristic is more flat than for the non-optimized version.

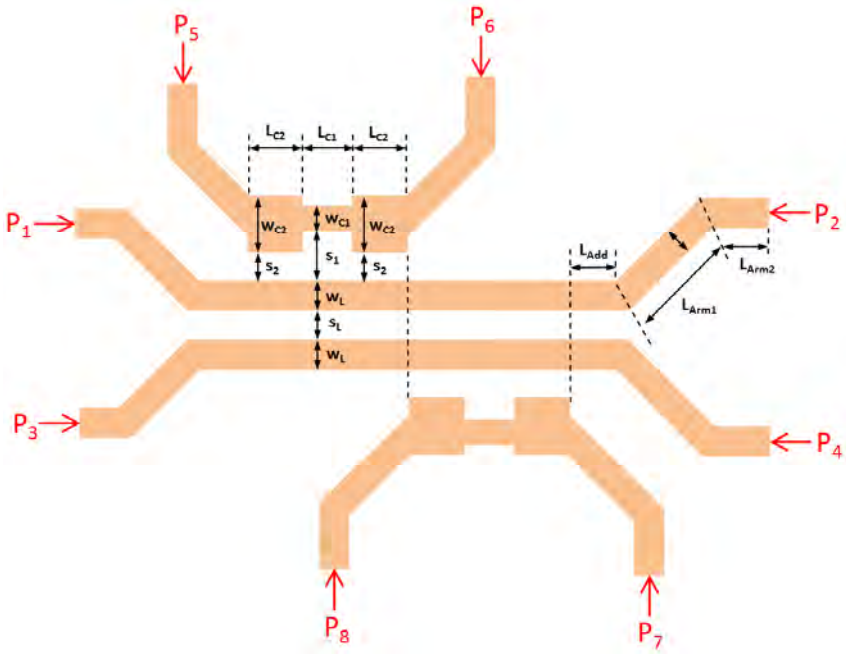

Figure 4.49: Physical model of the 1GHz optimized differential signal coupler

Table 4.6: Geometrical dimensions of the 1GHz optimized differential signal coupler

Dimension	Value [mm]
w_L	2.88
s_L	0.67
L_{Add}	30.00
w_{Arm1}	2.97
L_{Arm1}	30.00
w_{Arm2}	2.97
L_{Arm2}	13.00

Dimension	Value [mm]
w_{C1}	0.67
s_1	4.92
L_{C1}	9.90
w_{C2}	6.24
s_2	0.67
L_{C2}	9.90

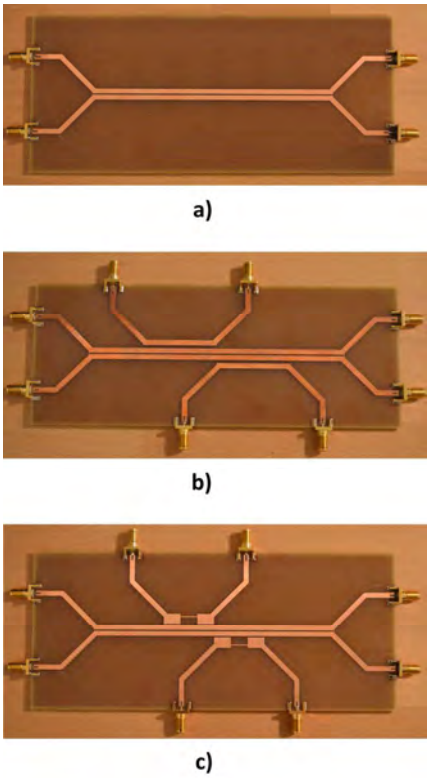

Figure 4.50: Physical realization of models: (a) reference transmission line, (b) transmission line with differential signal coupler, (c) transmission line with optimized differential signal coupler

From the practical point of view, this difference is not critical because it takes place in the area when match is better than -30dB. Above 1.8GHz the transmission line match characteristic significantly differs from the characteristics of the non-optimized version and the reference transmission line. We can observe in the transmission line phase characteristic (Fig. 4.52) that the configuration with the optimized version of the coupler is closer to the reference line than the non-optimized up to 450MHz. In the sub-band 700MHz-900MHz, the error defined as a difference between the phase characteristic of the configuration with the coupler and the reference line is greater for the optimized (up to 50°) than the non-optimized version (up to 5°). For higher sub-band (900MHz-1.2GHz), the error for both configurations has similar values (up to 40°) but the opposite sign. For sub-band 1.2GHz-1.5GHz characteristics for both configurations are in line with the reference line. For higher frequencies (up to the end of the measurement band), the characteristic of the optimized configuration has different

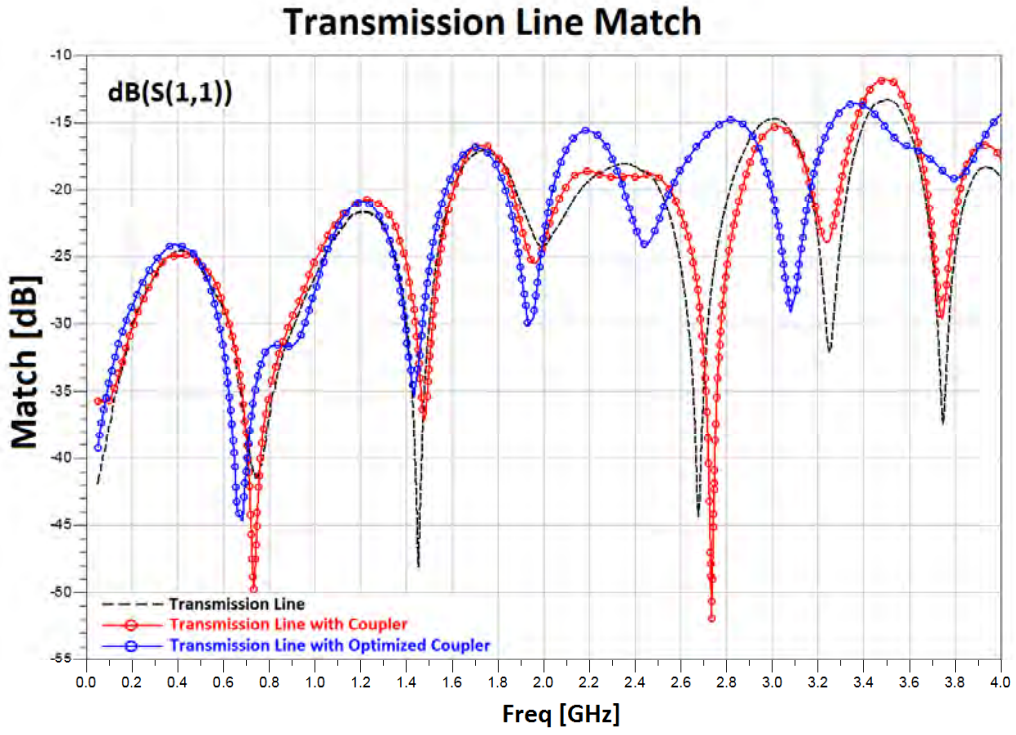

Figure 4.51: 1GHz differential signal optimized coupler - measurement results: main transmission line match

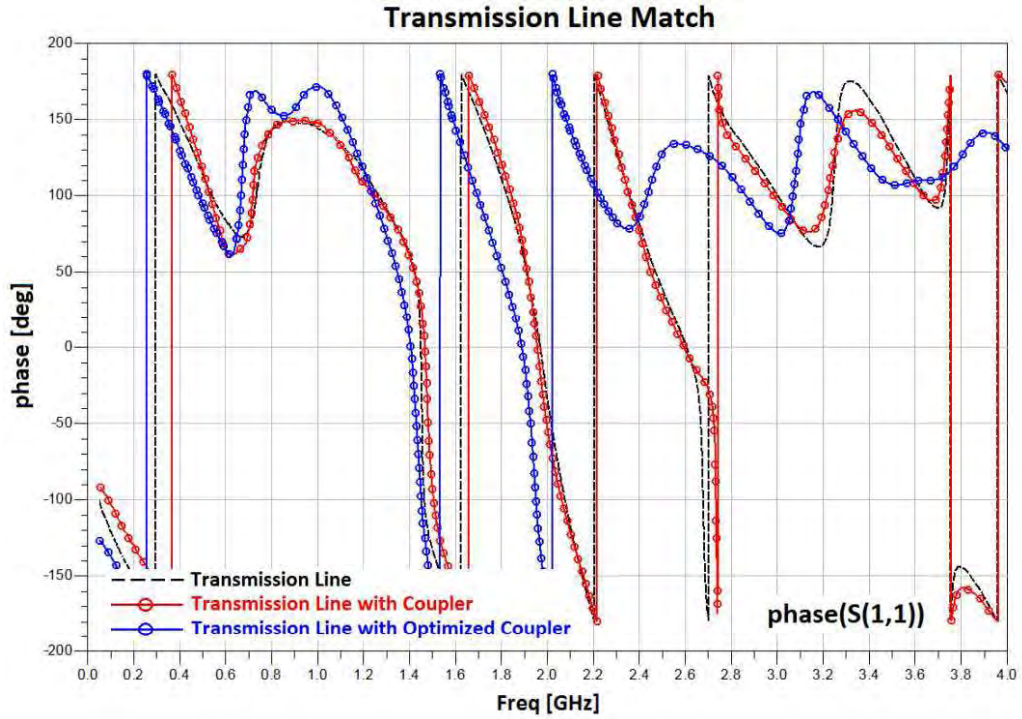

Figure 4.52: 1GHz differential signal optimized coupler - measurement results: main transmission line match phase characteristic

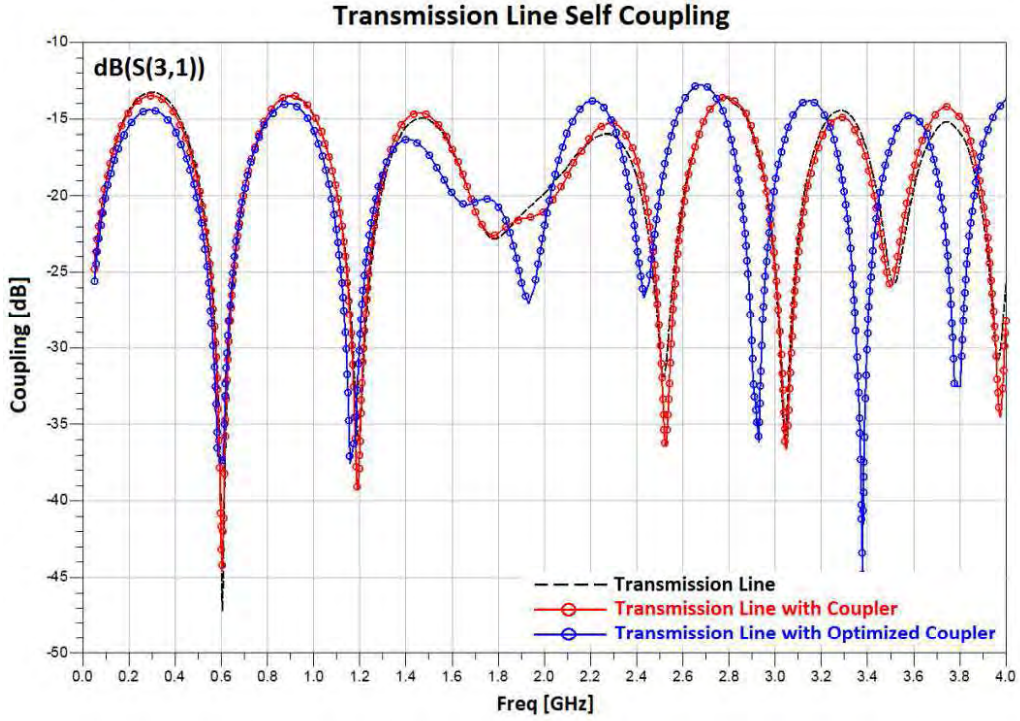

Figure 4.53: 1GHz differential signal optimized coupler - measurement results: main transmission line self coupling

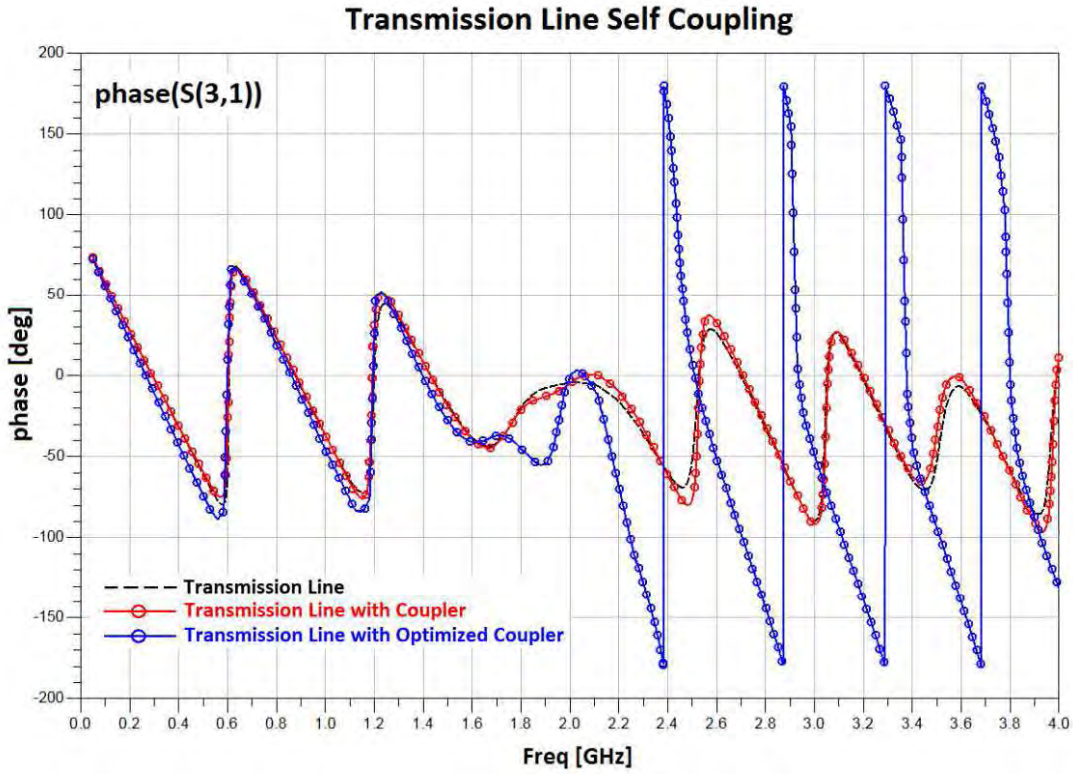

Figure 4.54: 1GHz differential signal optimized coupler - measurement results: main transmission line self coupling phase characteristic

shape than the reference line and the non-optimized configuration. The main transmission line self coupling characteristic is presented in Fig. 4.53 and Fig. 4.54. In sub-band 200MHz-400MHz, the amplitude of the main transmission line self-coupling characteristic is about 1dB lower than for the non-optimized version and the reference transmission line. For higher frequencies up to 1.4GHz, both coupler configurations are in line with the reference line. In the sub band 1.4GHz-2.0GHz, the shape of the amplitude characteristic for the optimized coupler significantly differs from the non-optimized configuration and the main transmission line (the difference reaches 3dB). For higher frequencies (up to 4GHz, which is the end of the measurement range) the amplitude of the main transmission line self-coupling characteristic of the optimized configuration has similar shape as the non-optimized version as well as the reference line but it is shifted towards lower frequencies (by about 100MHz to 200MHz). Similar observations can be made for the main transmission line self coupling phase characteristic (Fig. 4.54). The single coupler's branch coupling characteristic for the optimized coupler structure (-21.5dB) is lower than for the non-optimized version (-19dB) at the operating frequency f_0=1GHz. This effect is due to the fact that one of the goal functions defined in the optimization process allowed a single branch coupling factor to be contained within the range of -18dB to -22dB. The resonance was shifted about 100MHz towards lower frequencies in comparison to the non-optimized structure. This effect is caused by the fact that the optimized coupler structure branch length is shorter than for the non-optimized version. As expected, the optimized version of the coupler has significantly better isolation through the entire measured frequency band (50MHz-4GHz). At the operating frequency, the isolation is 17dB better for the optimized version (-40dB) than for the non-optimized structure (-23dB). The same value was obtained through simulation (Fig. 4.44). The main line transmission loss characteristic is presented in Fig. 4.57 and Fig. 4.58. We can observe that up to 2.9GHz, the main transmission line loss characteristic for the configuration with the optimized coupler is closer to the reference transmission line than for the non-optimized version. For higher frequencies the attenuation for the optimized version is lower than for the non-optimized case and the reference line (the difference reaches 0.7dB). For the optimized coupler version some phase error in the main transmission line is visible (Fig. 4.58). Up to 800MHz, the error is negligible. For higher band (to 1.6GHz) the error is lower than 25° and it steadily grows for higher frequencies.

Conclusions

The measurement results show that it is possible to optimize the geometry of the differential signal coupler the branch step impedance methodology, and to improve the isolation without significant deterioration of other important parameters. For the physically realized model, the isolation was improved in the entire measurement range (from 50MHz to 4GHz). The isolation has been increased by 17dB from -23dB for non optimized to -40dB for the optimized version at the operating frequency of f_0=1GHz. The desired single branch coupling factor was preserved at the satisfactory level of -21.5dB (for initial structure this factor was

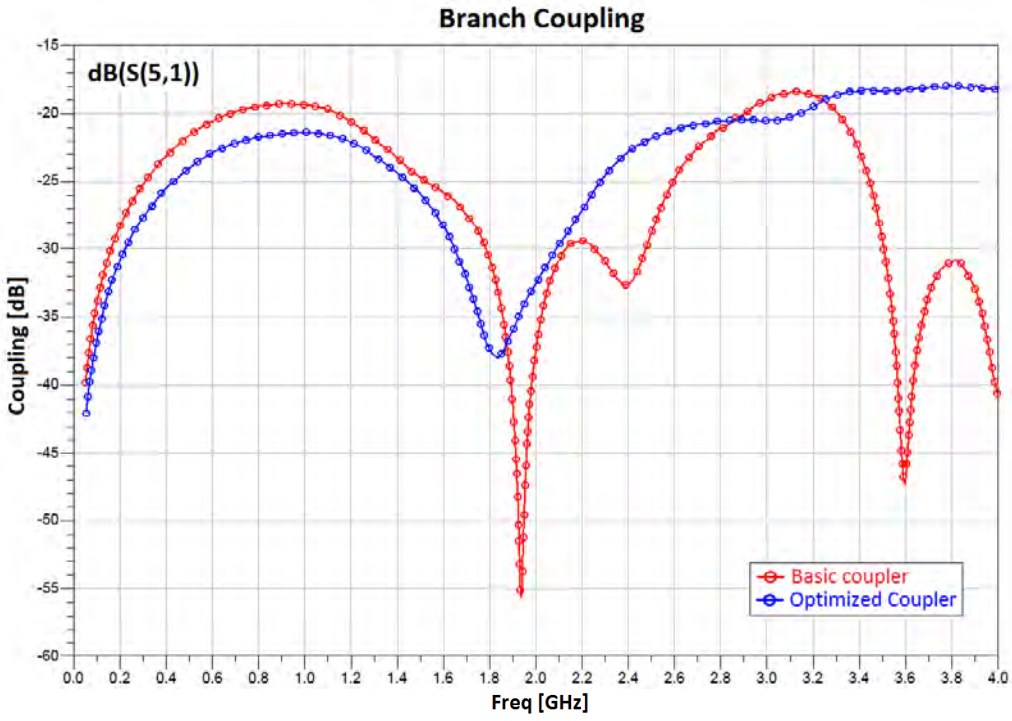

Figure 4.55: 1GHz differential signal optimized coupler - measurement results: single coupler's branch coupling

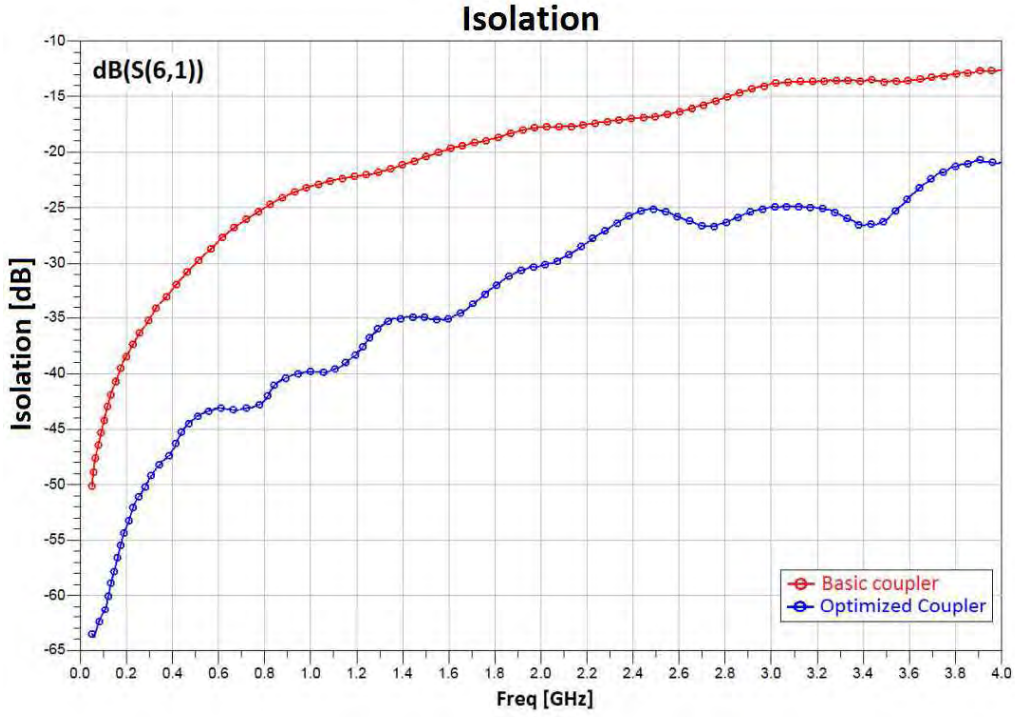

Figure 4.56: 1GHz differential signal optimized coupler - measurement results: single coupler's branch isolation

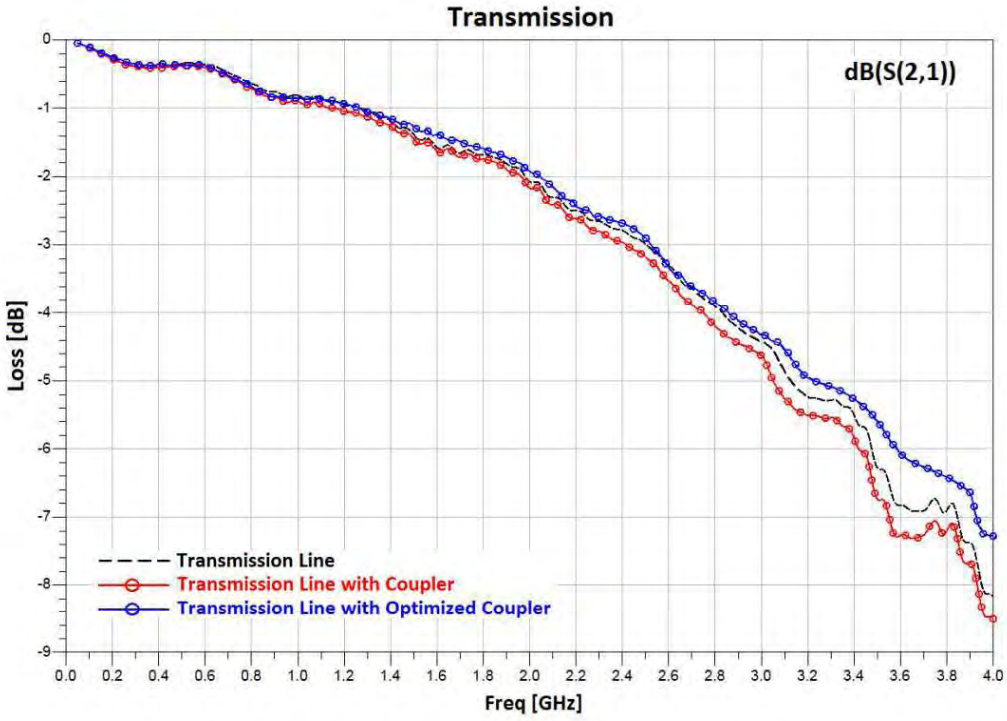

Figure 4.57: 1GHz differential signal optimized coupler - measurement results: main transmission line loss characteristic

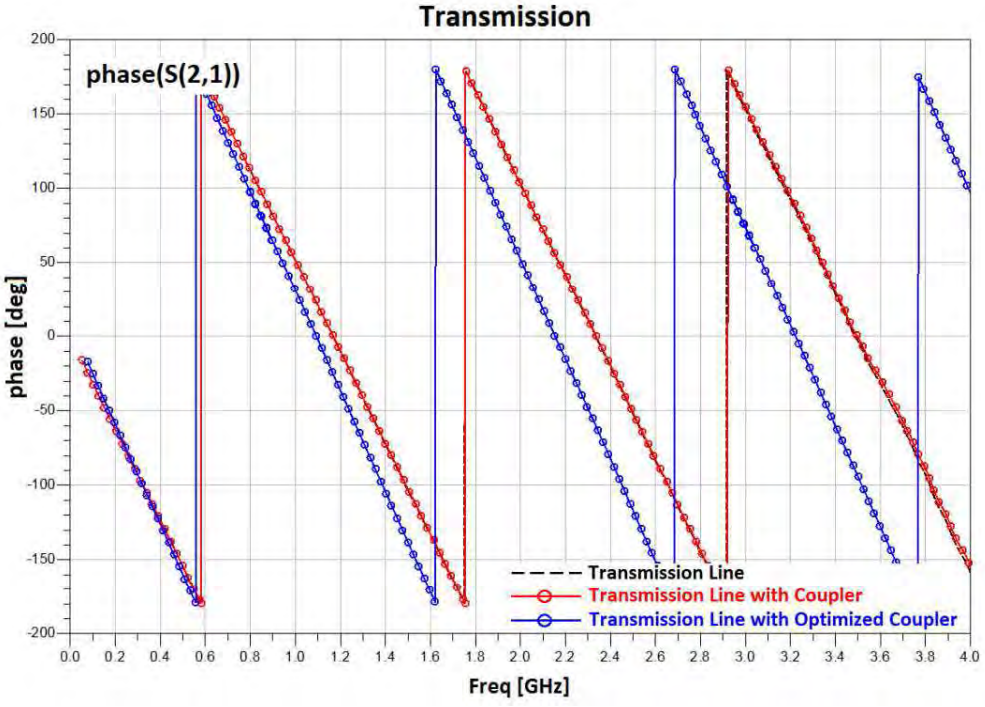

Figure 4.58: 1GHz differential signal optimized coupler - measurement results: main transmission line loss phase characteristic

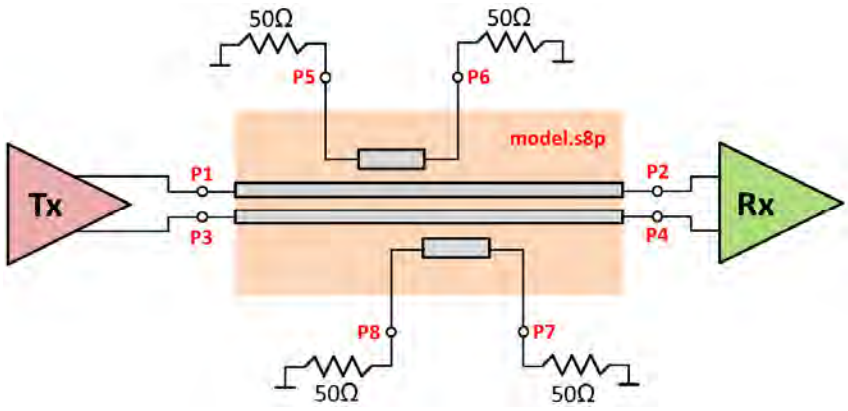

Figure 4.59: Block diagram of simulated link configuration

at the level -19dB). Additionally, it was shown that the optimized structure has negligible impact on the main transmission line working conditions (transmission line match, self-coupling factor and the main transmission line transmission loss).

4.5 Chip-to-chip time domain simulations

Overview

This section presents the time domain simulations of high speed data transmission monitoring for chip-to-chip communication on PCB. The simulations were performed with Agilent ADS simulation environment which has included the dedicated models of digital transmitters. The analysis was done for the two transmission rates: 200Mb/s and 333Mb/s and two configurations of a differential signal coupler (operating frequency f_0=1GHz): initial (designed in Section 4.3) and optimized (designed in Section 4.4)). All results are compared with the parameters obtained for the reference transmission line without a coupler.

Goals

The main goal of these simulations is to prove that it is possible to decouple the signal from a pair of lines on PCB which guides transmission in the differential mode. Additionally, the comparison of results obtained for two coupler configurations (initial and with improved directivity) should be done.

Simulations

The behavior of the main transmission line with the differential signal coupler was modeled by use of **.s8p* files from frequency domain measurements obtained in the previous sections. The environment of the simulated system is presented in Fig. 4.59. The signal generated in the transmitter Tx is transfered through

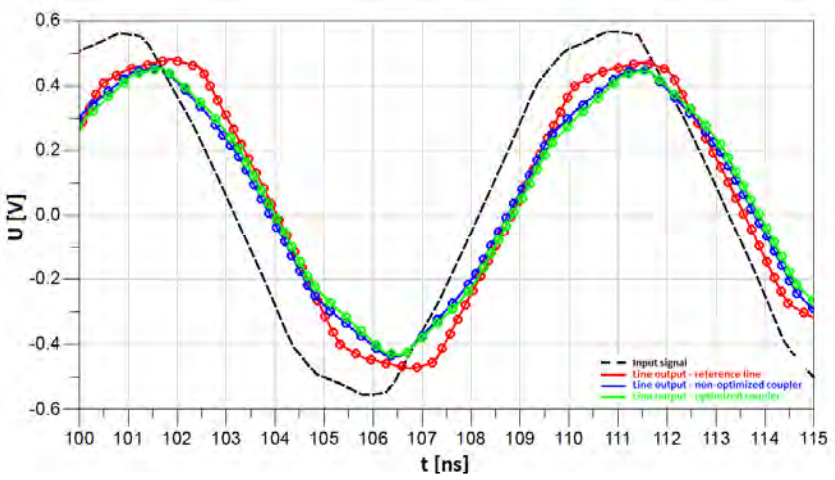

Figure 4.60: Transmission line input (black) and output signals (200Mb/s transmission) for reference line (red), line with non-optimized coupler (blue) and line with optimized coupler (green)

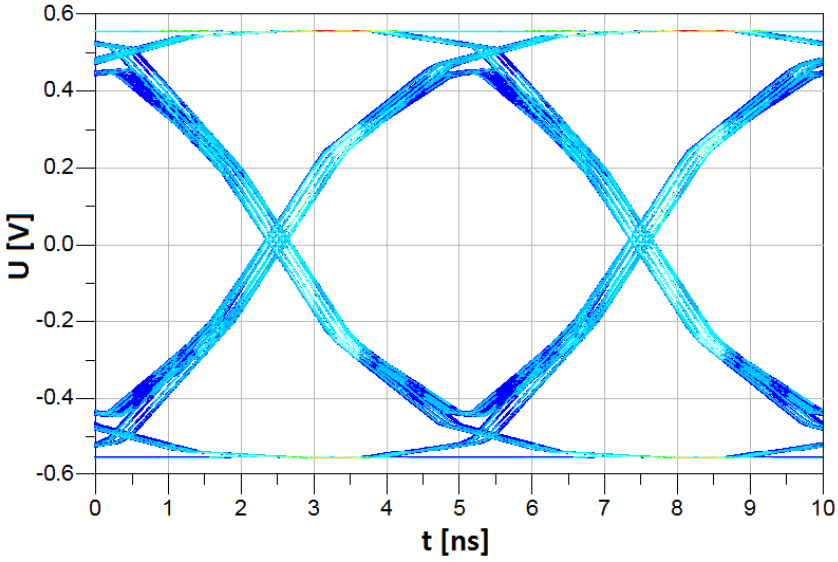

Figure 4.61: Eye diagram for the transmission line output signal (200Mb/s transmission)

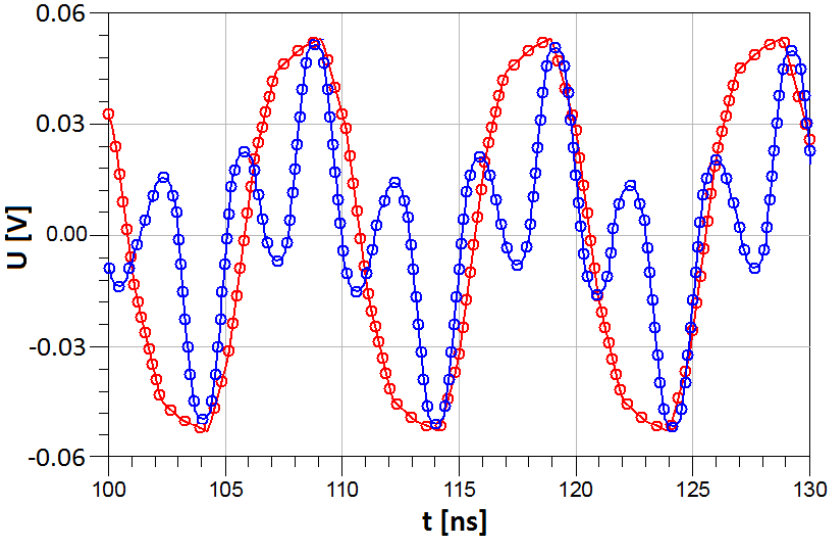

Figure 4.62: Transmission line decoupled signals (200Mb/s transmission) for non-optimized coupler (red) and line with optimized coupler (blue)

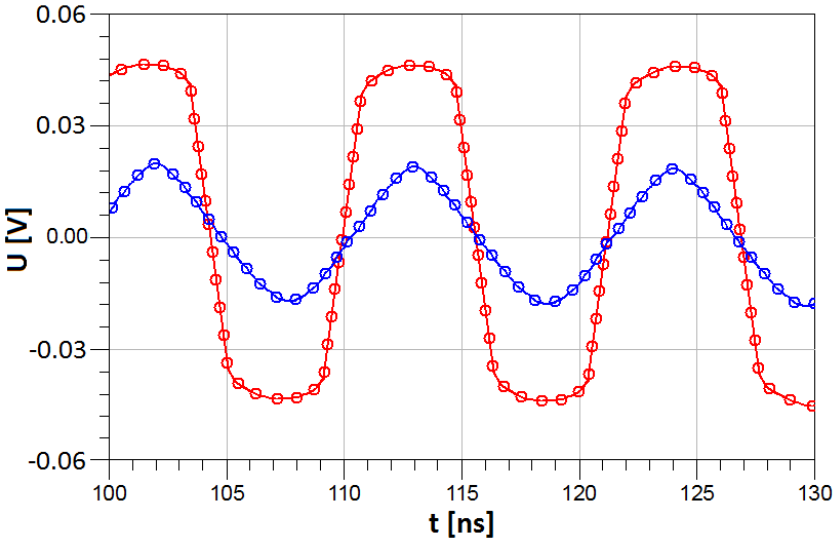

Figure 4.63: Signal in isolated port for non-optimized (red) and optimized (blue) version of coupler (200Mb/s transmission)

the main transmission line from the port input (P1-P3) to the output (P2-P4). The transfered signal is decoupled by the differential signal coupler placed along the central part of the main transmission line.

The simulation results for 200Mb/s transmission rate are presented in the figures below. The eye diagram obtained for random data encoded with 8b/10b scheme is presented in Fig. 4.65. The width and height of the eye diagram is 5ns and 0.9V, respectively. The input and output signal waveforms for the three configurations of the lines under test (the reference transmission line, the transmission line with the non-optimized coupler and the transmission line with the optimized coupler) are presented in Fig. 4.64. We can observe that the time of signal transmission from the input to the output is the same for all cases and it is 2ns. The output signals for both configurations with the coupler have are almost identical, and they are slightly different from the reference line case. The most important differences are visible at the top and the bottom backs of waveforms. The backs for the reference line case are more flat than for the configurations with couplers. This is caused by additional parasitic capacitances introduced by the coupler's branches neighborhood. The output signal from the coupler's coupled port P5 is presented in Fig. 4.66. For both coupler configurations, the amplitudes of the decoupled signal have the same values. We can observe that the decoupled signal for the optimized coupler has steeper slopes than the non-optimized version. Additionally, for the optimized version, the reaction to the rising and falling edges of the signal in the monitored line is more clear (we can see the rapid changes of amplitude when the slope in the main line occurs). The rising and the falling edges can be easily determined based on polarization of the decoupled impulse. This fact is particularly important from the measurement applications point of view. The ability to determine the moment of rising and falling edge arrival in the main line will determine the time resolution of the monitoring system. The output signal from the coupler's isolated port P5 is presented in Fig. 4.67. For the ideal case, no signal should be observed in the isolated port when transmission is carried out only in one direction. The non zero amplitude of the signal in the isolated port is caused by the finite coupler's directivity (some part from the decoupled port is visible in the isolated port). We can observe that the amplitude of the signal in the isolated port is significantly (two times) lower for the optimized version of the coupler. The amplitude for the non-optimized version of the coupler is comparable to the amplitude of the signal in the decoupled port. The coupler's directivity has key influence on the ability to distinguish the direction of the transmission in the main line.

The simulation results for the same test set but with 333Mb/s transmission rate are presented in the figures below. We can observe that the transmission delay for both configurations with the coupler (Fig. 4.64) are the same (3ns) which is about 0.3ns more than for the reference line without the coupler. The signal observed in the decoupled port of couplers is presented in Fig. 4.66. We can make similar conclusions regarding the optimized and not optimized versions of the coupler. For 333Mb/s transmission case, the shape of the signal decoupled with the optimized coupler is closer to the non-optimized version. The returns

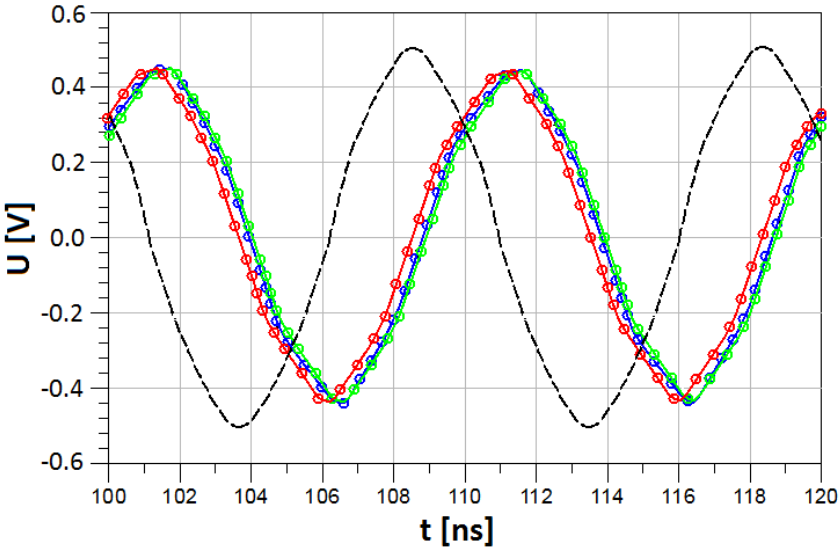

Figure 4.64: Transmission line input (black) and output signals (333Mb/s transmission) for reference line (red), line with non-optimized coupler (blue) and line with optimized coupler (green)

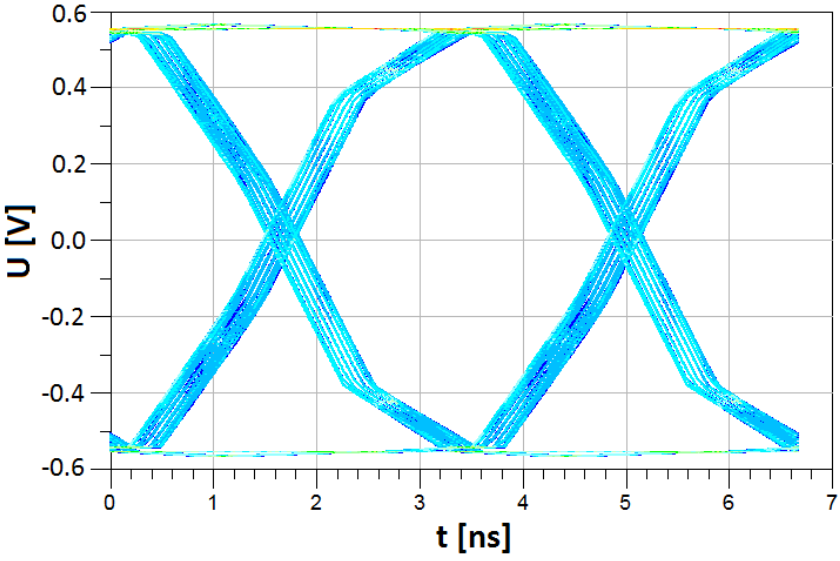

Figure 4.65: Eye diagram for transmission line output signal (333Mb/s transmission)

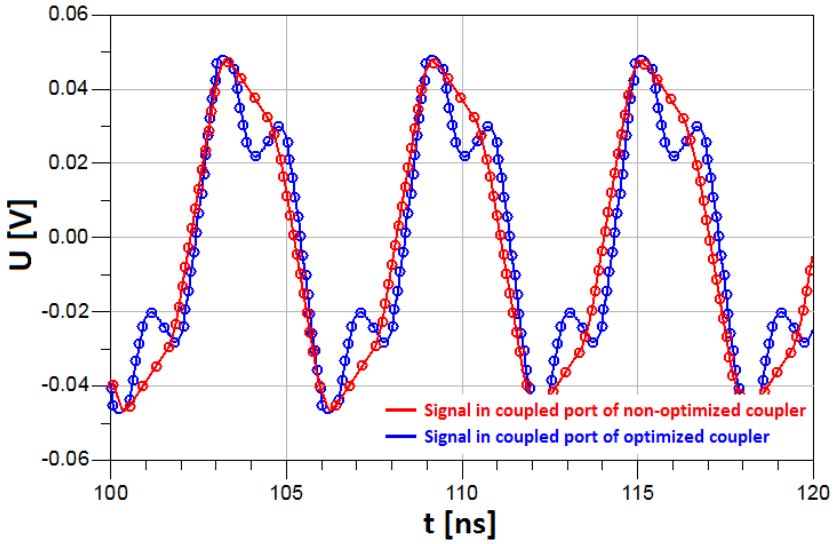

Figure 4.66: Transmission line decoupled signals (333Mb/s transmission) for non-optimized coupler (red) and line with optimized coupler (blue)

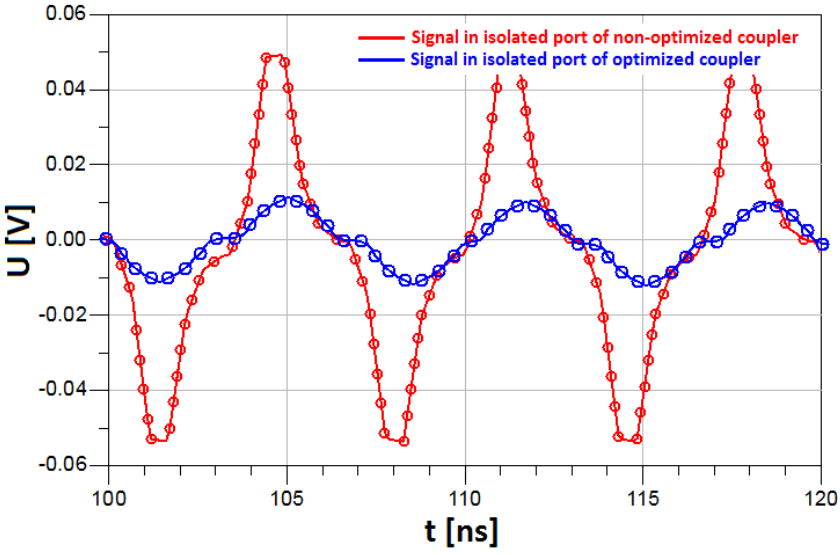

Figure 4.67: Signal in isolated port for non-optimized (red) and optimized (blue) version of coupler (333Mb/s transmission)

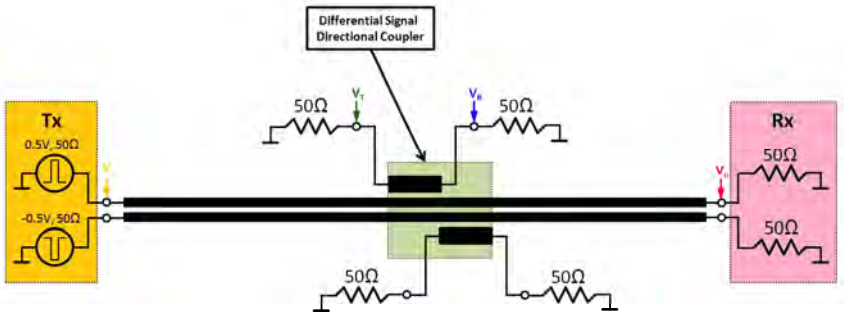

Figure 4.68: Block diagram of measurement test set

to the vicinity of zero amplitude between rising and falling edges of the signal in the main transmission line for the optimized coupler are not as clear as for the 200Mb/s case. This is caused by the limited bandwidth of the coupler (the significant power of 333Mb/s signal is located at higher frequencies than for the 200Mb/s case). The signals observed in the isolated ports for each coupler configuration are presented in Fig. 4.67. The observations are similar as for 200Mb/s case, however for 333Mb/s transmission, the difference in amplitude between both coupler's configurations is higher (the amplitude for the optimized coupler is five times lower than for the non-optimized one).

Conclusions

The simulation results show that it is possible to probe the signal from the main transmission line with the differential signal coupler for transmission monitoring purposes. The simulations indicate that the optimized version of the coupler exhibits better properties in terms of the time domain resolution than the non-optimized one. The time domain resolution which enables the possibility of determining the time position of rising and falling edges of the signal in the monitored line is a very important parameter for transmission monitoring applications.

The next step is to verify the simulation results through measurements of a physical model. This will be presented in the next section.

4.6 Chip-to-chip time domain measurements

Overview

This section describes the practical example of serial transmission monitoring with previously described differential signal coupler on PCB between two ICs. As an example IC, the FPGA Xilinx chip will be used. The measurements are performed for two example transmission rates: 200Mb/s and 333Mb/s. The block diagram of the measurement setup is presented in Fig. 4.68.

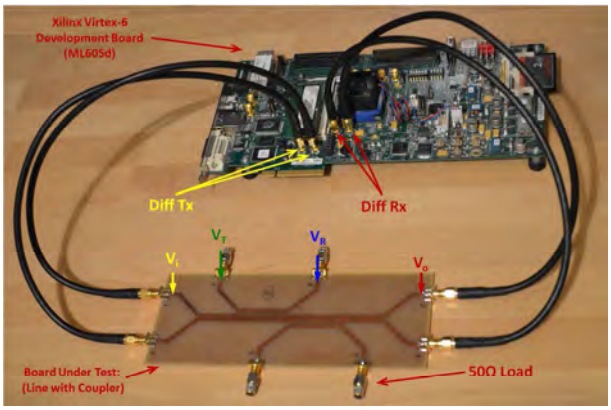

Figure 4.69: Measurement test set: Xilinx Virtex-6 FPGA development board with transmission line under test and a differential signal coupler

Goals

The main objective is to verify the practical possibility of decoupling the signal from transmission guided in a pair of coupled microstripes on PCB using the proposed construction of the differential signal coupler. Additionally, a comparison of the initial and the optimized version of the coupler will be carried out.

Measurements

The measurement system is composed of the differential transmitter (Tx) and the receiver (Rx) integrated in the IC (Xilinx ML605M development board with MultiGigabit SMA ports [148]), transmission line with the differential signal coupler under test with test points (signed as V_i, V_T, V_R and V_o). The Tx generates a differential signal with amplitudes 0.5V in reference to the ground which results in 1V amplitude between the coupled lines. The differential signal coupler is placed in the middle of the transmission line.

All ports of the differential signal coupler are terminated with the matched 50Ω load. The PCB under test is connected with Tx and Rx by SMA 50Ω cables. The signals are observed with Agilent InfiniVision 7000B digital osciloscope [149] in the measurement points as follows: V_i - the input signal for the single micristrip line, V_T - the signal decoupled from the transmission line in direction Tx-Rx, V_R - the coupler's isolated port, V_o - a single transmission line output at the Rx side. Additionally, the spectrum of signals transmitted by Tx is observed with Agilent X-Series Signal Analyzer N9000A [150]. The measurement result will be presented for initial configuration of the coupler (designed with classical design methodology presented in Section 4.3) and for the optimized version presented in Section 4.4. The operating frequency for the differential signal couplers is f_0=1GHz. The PCB was implemented on FR4 laminate (ϵ_r=4.4, H=1.55mm).

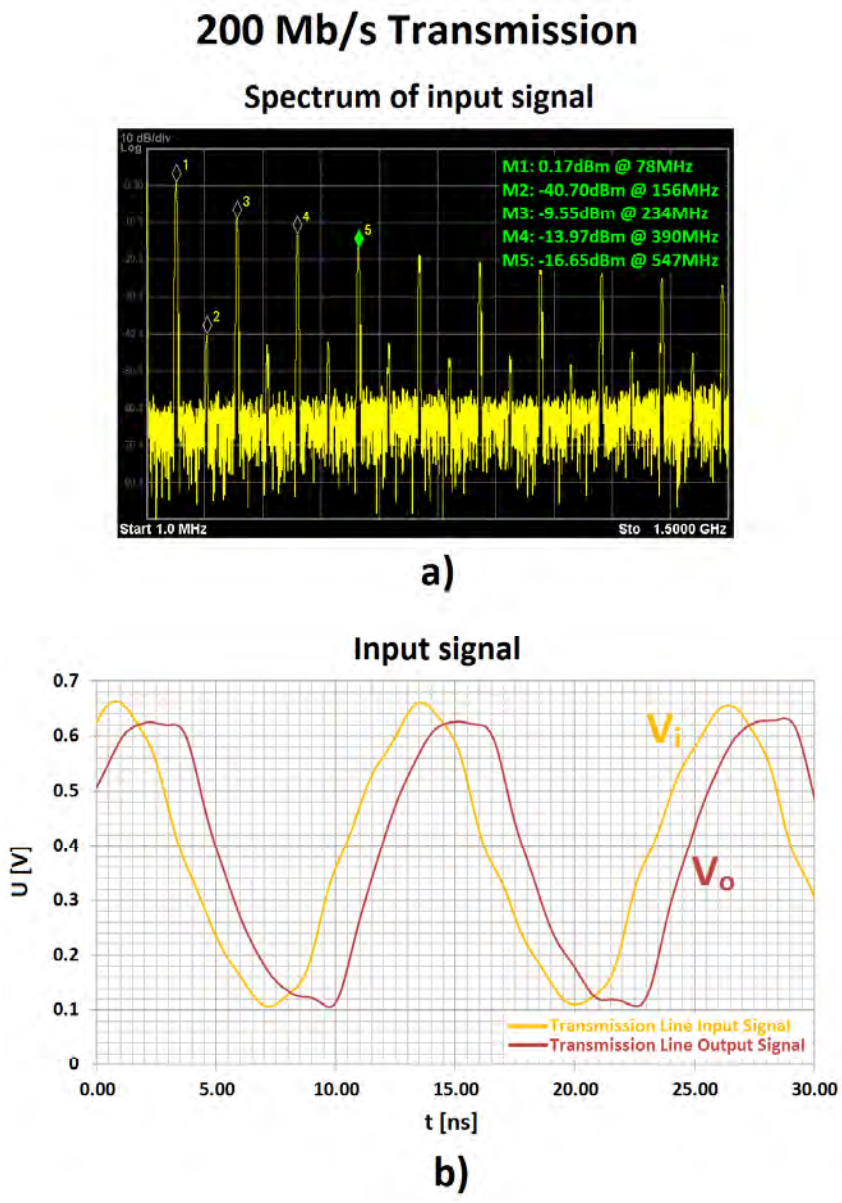

Figure 4.70: Time domain measurements results for 200Mb/s transmission: (a) the spectrum of V_i signal, (b) V_i and V_o signals

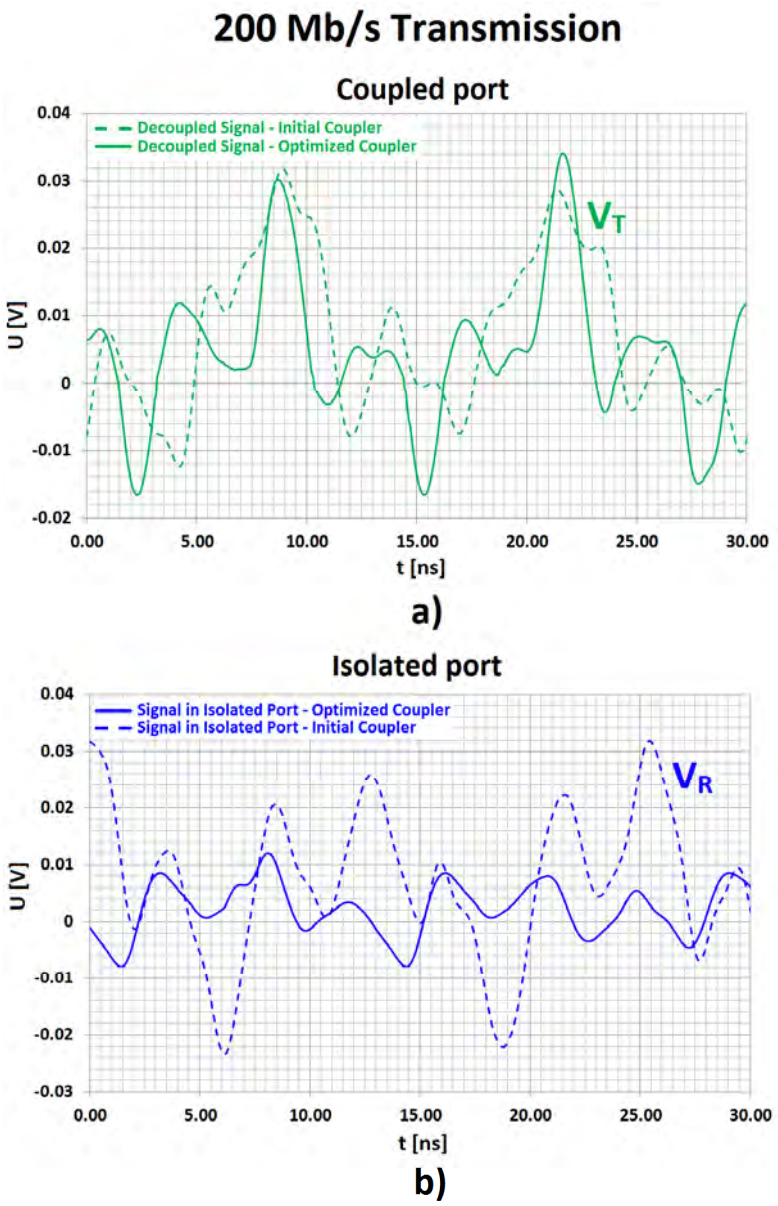

Figure 4.71: Time domain measurements results for 200Mb/s transmission: (a) signal V_T in coupled port, (b) signal V_R in isolated port for optimized and not optimized version of coupler

The measurement results related to the main transmission line parameters will be compared with the reference transmission line (without a coupler). The measurement setup is shown in Fig. 4.69.

The measurement results are presented in Fig. 4.70, Fig. 4.71, Fig. 4.72 and Fig. 4.73. As we can observe, a significant part of the input signal power for both cases is concentrated in the frequency band below 1GHz. For 200Mb/s transmission, the delay in the transmission line is 1.5ns. The amplitude of the signal V_o at the Rx side is 0.05V lower than V_i on the Tx side. Additionally, the shape of the signal is slightly distorted. The same results were obtained for all three test boards: the reference transmission line and the transmission line with couplers. This indicates that the designed differential signal couplers do not disturb the transmission under test. For 333Mb/s, the transmission delay has the same value as for 200Mb/s (1.5ns). For this case, the amplitude of the signal V_o on the Rx side is more significantly reduced (by about 0.2V). The measured waveforms were identical for all three boards, which proves that the couplers do not disturb transmission in the main line for 333Mb/s either. The signal from the coupled port V_T for 200Mb/s transmission has visible peaks at the moments when there is a rising or falling edge in the main transmission line. The amplitude of V_T is 45mV. This value is sufficiently high to be processed. The peaks are significantly more clear for the optimized version of the coupler (the one with higher directivity). For both cases, it is possible to recover the information about the data transmitted in the main line on the basis of the signal decoupled by the differential signal coupler. The signal in the isolated port V_R should be equal to zero for the ideal coupler. For the initial version of the coupler, the amplitude of the signal in the isolated port is comparable to the amplitude of the signal in the coupled port. The situation is greatly improved for the coupler with optimized directivity. The decoupled signal waveform V_T for 333Mb/s transmission looks completely different. The amplitude of V_T=60mV is higher than for 200Mb/s transmission. The reason for this is that the major part of the signal spectrum 333Mb/s is located at higher frequencies where the coupler's coupling coefficient is higher. Due to the short duration time of the Tx pulses V_i with smooth slopes, the coupled impulses caused by the rising and falling edges overlap. However, it does not preclude the possibility of recovering information about the signal transmitted in the main line on the basis of the signal decoupled by the differential signal coupler. For 333Mb/s case, similarly as for the 200Mb/s case, the signal in the isolated port V_R has much lower level for the configuration using the coupler optimized for directivity.

Conclusions

The obtained measurement results prove that it is possible to observe serial transmission with differential signaling on PCB between ICs with the proposed differential signal coupler. Additionally, it was shown that the optimized version of the coupler (with improved directivity) allows us to improve directivity which results in better measurement resolution.

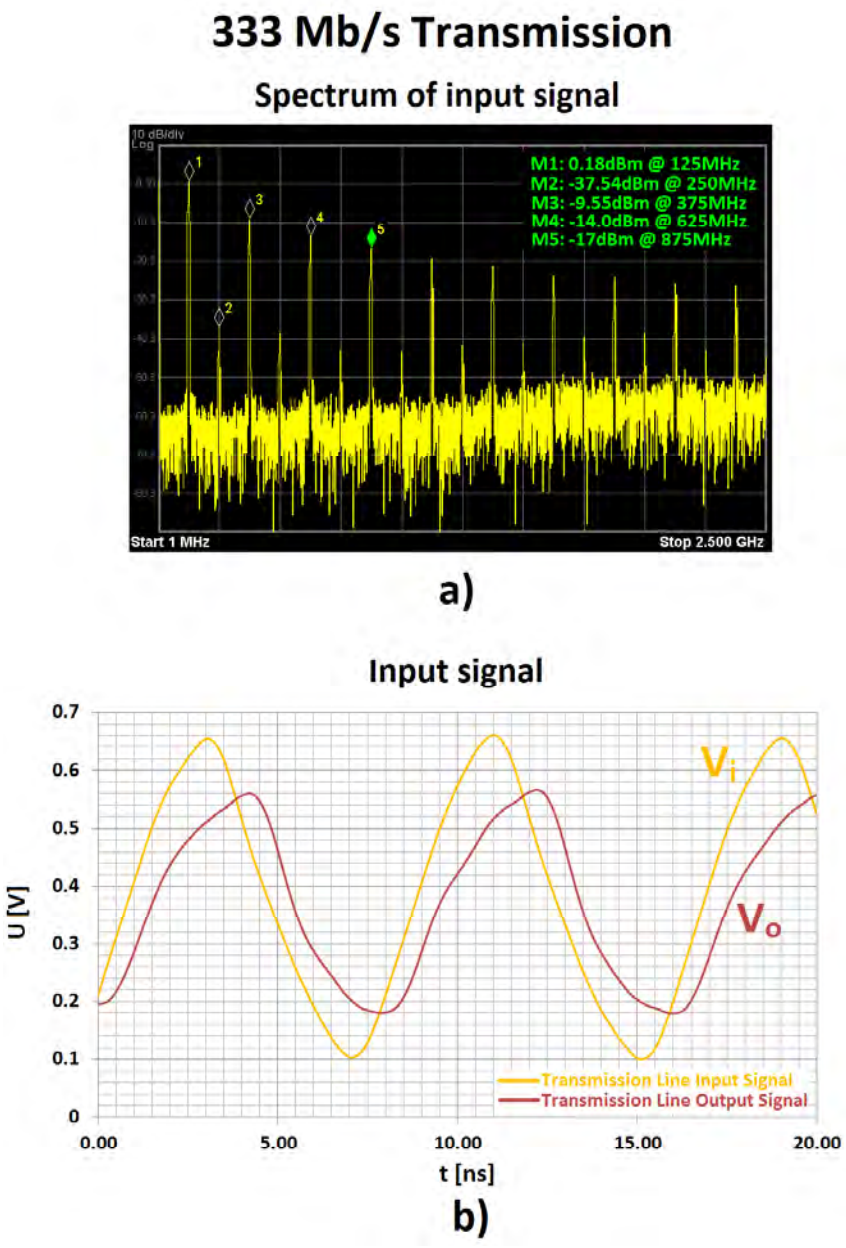

Figure 4.72: Time domain measurements results for 333Mb/s transmission: (a) the spectrum of V_i signal, (b) V_i and V_o signals

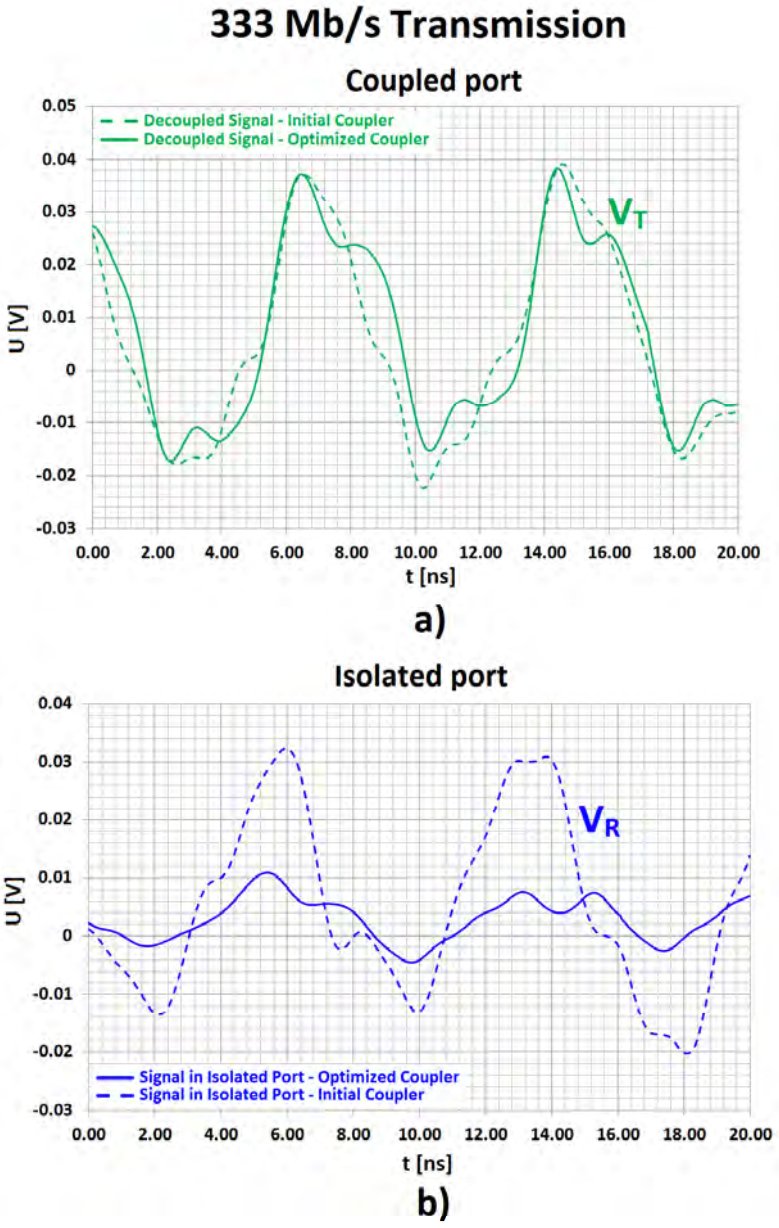

Figure 4.73: Time domain measurements results for 333Mb/s transmission: (a) signal V_T in coupled port, (b) signal V_R in isolated port for optimized and not optimized version of coupler

4.7 Applications

This section discusses possible applications of the proposed differential signal coupler for high speed data transmission. The possibility of using the differential signal coupler in the described applications was indicated by simulations and measurement results presented in the previous sections. The considered range of potential applications is not limited to the measurement systems. The author indicates the areas related to mission critical and AC Coupled Interconnect (ACCI) multi-slave systems.

Serial data transmission monitoring

The debugging process of high speed data links is becoming more and more important. Modern devices require extremely fast chip-to-chip interconnections. Often, the major bottleneck which limits the system performance is related to connections on PCBs (Printed Circuit Board) [151]. Limited bandwidth, mismatched terminations on the receiver (Rx) or the transmitter (Tx) side, crosstalks, interferences from other parts of the system, differences in transmission line length for multi-conductor transmission which causes the disturbance of phase relations, can significantly reduce maximum transmission rate which is available for a given bit error rate (BER) [48]. This situation drives the researchers to looking for new solutions [114, 116, 115].

An important aspect of improving the high-speed interconnection performance is to ensure that the prototype and production model signal integrity debug process allows for finding the real root cause. Various reasons (e.g., malfunction of Tx and/or Rx, rapid change of the line impedance, Tx/Rx mismatch, interference from other devices) may result in various problems in transmission quality, including excessive BER or interfering with other devices on PCB. Attempts to solve problems that are based on general symptoms of the defect, can, in many cases, result in incorrect conclusions. Some problems can only be detected by using special signal sequences or when a particular situation occurs in the adjacent subsystem e.g., in poorly designed links, considerably large error rates may appear for specific symbol sequences due to inter-symbol-interferences (ISI) [152]. Therefore, real-time debugging techniques become indispensable in many cases [97, 153].

The problems associated with launching the new systems, such as those mentioned in the previous paragraph, result in a situation where more and more designers develop their projects to comply with generally accepted standards and investigate the compliance of the design with these particular standards. Another incentive for this approach is wide availability of tools to verify compatibility with the common industrial standards, which can significantly speed up design and launching process. Regardless of the specific approach adopted by the designer, the most crucial element of the measurement environment employed to debug the system is a connector, which, beside of the limited bandwidth, can significantly affect the measured transmission.

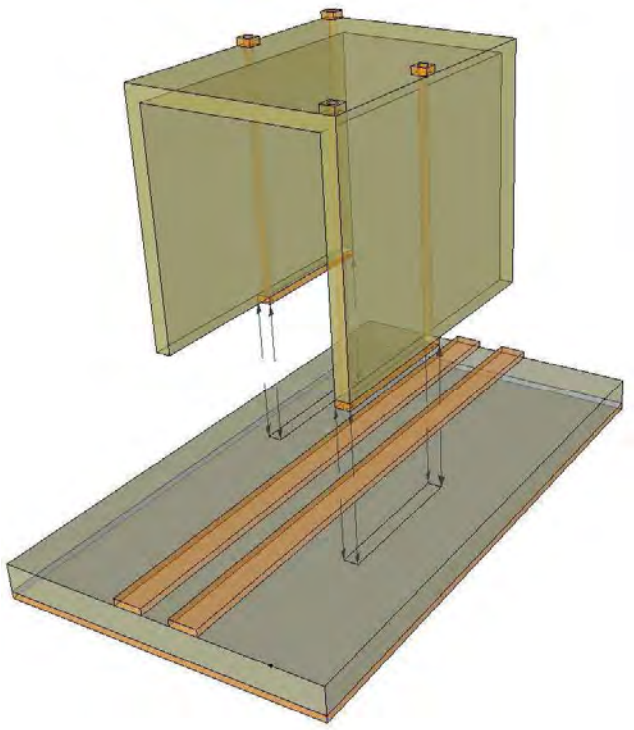

Figure 4.74: The mechanical construction of differential signal coupler for high speed data transmission monitoring on PCB

A possible solution to this problem are socket-less signal probing techniques [97] that have been rapidly developed over the last several years, and the use dedicated heads which are applied to the dedicated pads on board for signal probing. While this approach eliminates the need of installing dedicated connectors for signal probing, it requires adding special pads to the layout.

The proposed differential signal coupler allows probing a signal from a pair of coupled microstrip lines which use differential signaling without dedicated connectors and special test points performed on PCB with transmission line. The mechanical construction of the measuring head with differential signal coupler is presented in Fig. 4.74. The measuring head can be overlayed on PCB anywhere along the monitored transmission line. Using the setup of Fig. 4.74 the differential signal coupler can be easily applied for high speed digital systems runtime debugging, the product diagnostic cost reduction by eliminating dedicated measurement connectors and reverse engineering.

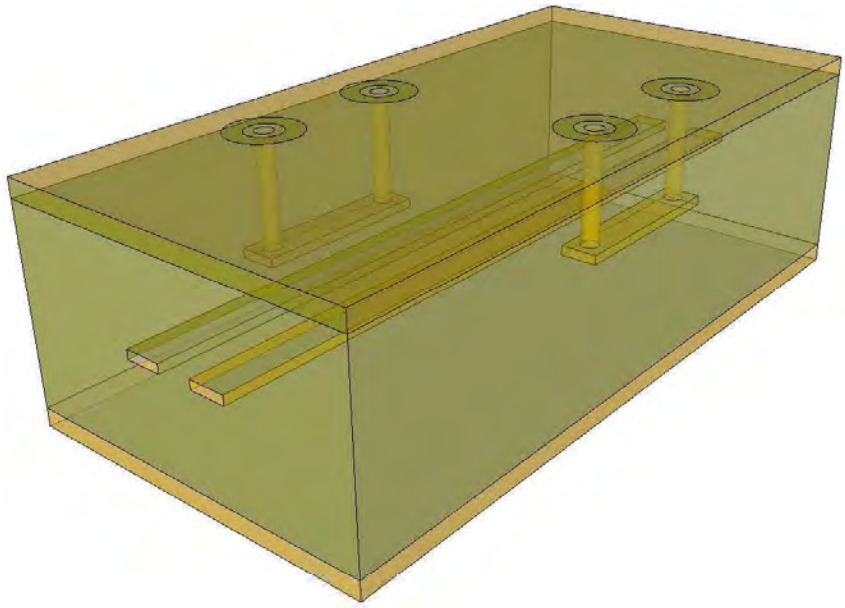

Figure 4.75: The stripline differential signal coupler implementation for high speed transmission monitoring

Inter-layer stripline link debug

Modern high speed data devices are more and more complex. The level of integration observed in new devices steadily grows. This results in continuous increase of PCB layout complexity [154, 155]. The new IC packages which have up to several hundred of pins, require multilayer PCB layout [156]. The development process of these devices is very complicated. In case of problems, monitoring of the signals at certain points in the system (located in the middle of the PCB layers stack) is difficult. Signal extraction is possible by means of special needles that are passed through the holes to the specific layer of the PCB laminate [157]. However, the use of these techniques is cumbersome and may interfere with the system working conditions.

Figure 4.75 presents the sample implementation of a differential coupler for stripline environment. This configuration can be used for transmitted signal probing without disturbing the system working conditions in multilayer PCB environment. The coupler branches can be easily added at selected points of the circuit along the strategic transmission lines. The probed signals can be piped to the surface of the PCB with the vias. The coupler's geometry design should take into account the vias diameter and length. The design procedure for coupler's geometry determination must be modified as compared to the methodology presented in Section 4.3. The relations appropriate for this case (strip line structure)

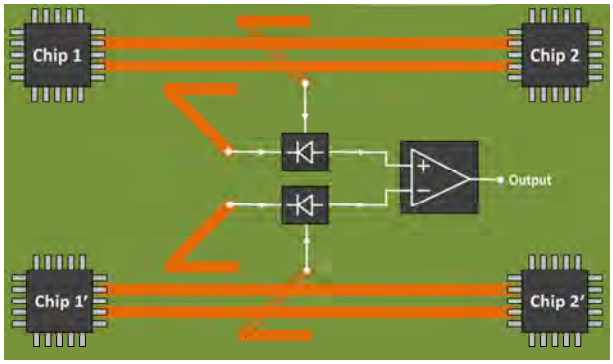

Figure 4.76: Application of differential signal coupler for mission-critical reliable redundant system

are presented in [158] for classical couplers. The proposed solution can be helpful in high speed system debug process by enabling signal acquisition without disturbing the system working conditions.

Mission critical systems

Many electronic systems which require extremely high level of reliability (like aircraft electronics, mission-critical server platforms or military equipment) use doubled components which perform the same operations simultaneously [159, 160, 161, 162]. The results obtained from both sources are compared. In case of differences it is concluded that an error has occurred and an extraordinary action is taken. The differential signal coupler can be used for transmission monitoring between two chips in mission critical system. This operation allows to identify the communication loss, physical disconnection or external interference detection. Additionally, as shown in Fig. 4.76 the set of two differential signal couplers allows us to compare communication activity in the main (Chip 1, Chip 2) and the redundant (Chip 1' and Chip 2') subsystem. The transmission activity monitoring can be implemented using a simple detector and an analog comparator without the need of using analysis on higher levels of communication (such as protocol analysis).

Load mismatch detection

The transmission line mismatch on the receiver side of a communication link can significantly degrade the quality of communication [163, 164]. Some part of the transmitted signal will be reflected at the end of the transmission line from the mismatched load. This phenomena should be considered taking by into account two aspects: decrease of signal power which is being processed in the receiver and the disturbance of the signal transmitted from Tx to Rx in the line by adding a reflected wave from the mismatched load. Both effects reduce SNR

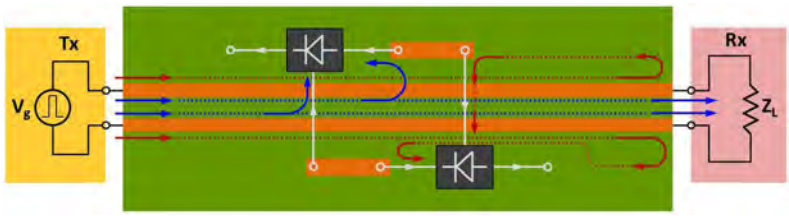

Figure 4.77: Load mismatch detection with differential signal coupler

in the receiver which can significantly decrease the quality of transmission. The differential signal coupler be used for transmission line mismatch load monitoring (Fig. 4.77). The information about increased mismatch level can be important for certain type of links (e.g. mission critical applications). Additionally, this methodology can disclose the receiver disconnection (e.g. intentional for hot-plug use case or unintentional, e.g. physical layer error). On the other hand, the monitoring of transmission line mismatches can be used to detect certain types of system attacks like overhearing by adding some probes by the attacker. After disclosure of sabotage, the transmitter may discontinue transmission to maintain data confidentiality.

ACCI multi slave

Modern high speed data interconnections take advantage of ACCI technology. The proposed differential signal coupler can be used to implement the separating element (Fig. 4.78a). This solution could significantly decrease the total product cost. In the literature, the first studies on the planar realization of coupling element on PCB are presented in [108, 109]. However, the reported studies are based on a different coupling structure.

Taking advantage of the fact that the presented construction of the differential signal coupler has negligible influence on the main transmission line (which was shown in Chapter 4 and in [56, 57]), it is possible to use it for ACCI multi slave architecture with relatively long structure (Fig. 4.78b). The basic concept of this solution is presented in Fig. 4.78 for CPU-to-multi-chip memory communication. The differential signal coupler parameters allow us to build a long chain of connected components.

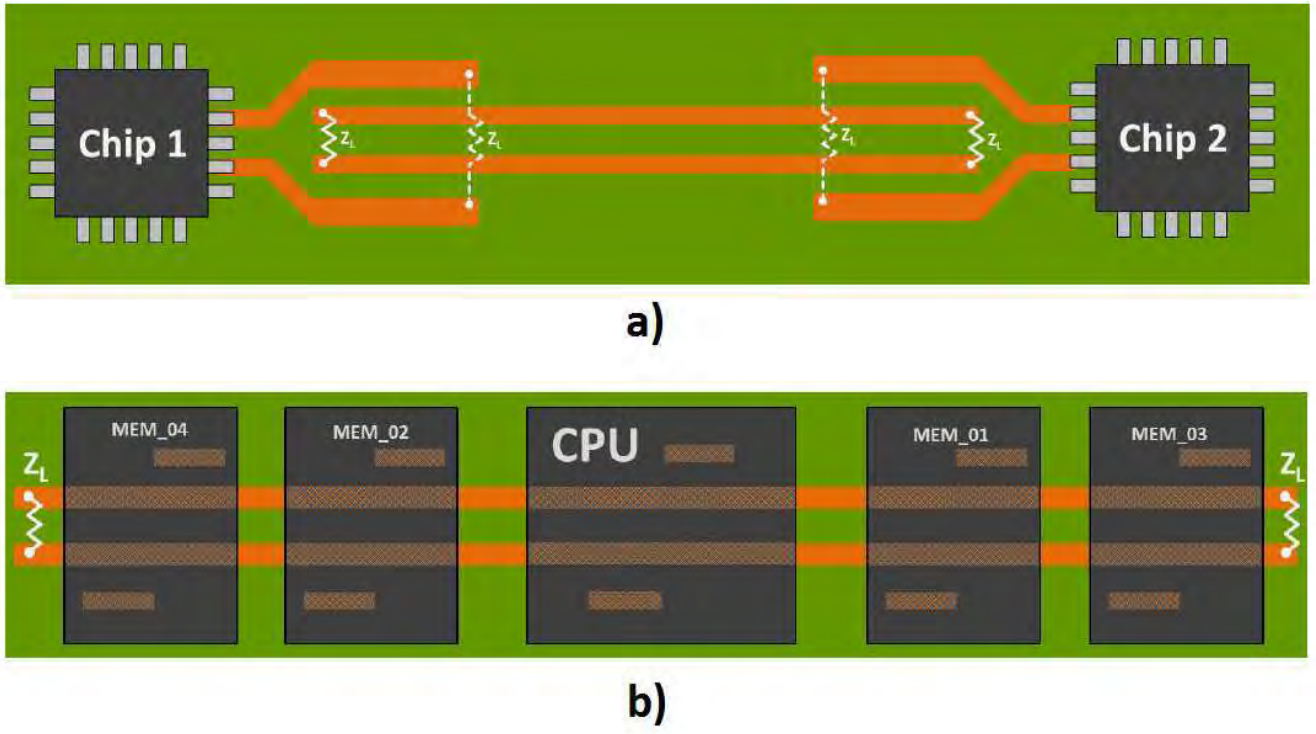

Figure 4.78: Differential signal coupler application for ACCI technology: (a) point-to-point communication, (b) multi-slave system

Chapter 5

Conclusions and Outlook

The main focus of this dissertation is in the introduction and development of the contact-less methodology of signal probing for high speed serial data transmission with differential signaling for chip-to-chip PCB interconnection environment. The architecture of differential signal coupler for monitored signal probing without disturbing the main transmission line working conditions was presented. The author proposed the complete design methodology which is based on methods for classical couplers. The correctness of the concept and design procedure was verified by simulations and measurements carried out for physically implemented models. Additionally, the full system measurements performed for real chip-to-chip transmission was realized. The obtained results were analyzed and evaluated for practical suitability. The presented contact-less serial transmission monitoring can be used for run-time system debug, reverse engineering or to minimize electronic devices manufacturing cost optimization by eliminating dedicated measurement connectors.

5.1 Summary of Original Accomplishments

The following are the original achievements of the author:

- Verification of the dissertation theses presented in Section 1.3.

  Thesis 1:

  It is possible to realize the proximity coupler which enables decoupling of the differential signal transmitted in the pair of coupled microstrip lines

  Thesis 2:

  It is possible to use the developed coupling structure to contact-less high speed data transmission monitoring between chips on Printed Circuit Board (PCB).

In Chapter 4, the author demonstrated through measurements and simulations that it is possible to realize the proximity coupler which enables the decoupling of the signal transmitted in the pair of coupled microstrip lines on PCB without disturbing the working conditions of the monitored line. Additionally, it was demonstrated, that it is possible to develop the coupling structure which enables monitoring of the high speed data transmission between chips on PCB.

- The concept of the new contact-less probing methodology for high speed data transmission monitoring on PCB chip-to-chip interconnections applied to a pair of coupled microstrip lines with differential signaling. The developed technology can be used for high speed data transmission diagnostics, run-time system debug and reverse engineering purposes.

- The topology of the coupling structure which enables contact-less signal probing without disturbing the working conditions of the main transmission line under test. The full design methodology with analysis, simulations and measurements was conducted. Obtained results confirm the correctness of taken assumptions and the proposed design procedure. The correctness of theoretical considerations was proved by simulations and measurement results for the example design. It was confirmed that the improved version of the coupler has significantly better probing properties than the original one.

- The methodology of directivity improvement with practical prove of concept. Geometrical dimensions of the new structure were obtained through optimization. Correctness of the proposed methodology of directivity improvement was verified by simulations and measurements of practical realized model. The obtained results were compared to the initial version of coupler.

- The example designs of differential signal couplers which were simulated, practically realized, and measured in time and frequency domain. The models were implemented on various substrates (FR4 and RO4003C) and for various operating frequencies (1GHz and 5GHz).

- Preparation of the dedicated measurement setup for real chip-to-chip environment analysis. The usefulness of the proposed methodology and proximity coupler construction was proved. The tests performed for two data rates (200Mb/s and 333 Mb/s) confirmed that the improved version of coupler allows for transmission monitoring with better time resolution.

- Additional applications related to high speed data transmission technology were proposed, which are not strictly related to high speed data transmission monitoring. The possibility of use for mission critical systems, high speed multi-slave buses and implementation of ACCI technology without discrete capacitors was included.

- The obtained simulation and measurement results were analyzed and evaluated. Using this findings, the practical usefulness was evaluated and future works perspective was highlighted.

5.2 Recommendations for Future Work

The trends observed for several years shows ever-growing demand for new electronic devices like smartphones, tablets and ultrabooks. The increasing popularity of electronic devices which enter to each area of human life, creates the need for total device cost optimization. The elimination of unnecessary elements from the device is in line with this trends. In the following years, we can expect rapid development of new measurement technologies which will aim at reducing the cost of diagnostics. The newest trends of performing measurements with socket-less methodology [97] suggest that in the near future, the first commercial contact-less systems which are based on probes designed as couplers to realize contact-less probing can be expected.

The new generations of equipment is usually associated with increased chip-to-chip transmission rate. Still increasing transmission rates allow us to predict that the total length of differential signal coupler's for new systems will be steadily decreased because of increased coupler's branch resonant frequency. The coupler's total length reduction can significantly improve the convenience of measurements and will broaden the scope of applicability of technology of the relatively short transmission lines monitoring. The important thread of differential signal coupler length reduction can be related to coupler's branch shape optimization [133]. On the other hand, we can observe the rapid research progress on the new technologies related to millimeter waves [165, 166]. Observing MMIC technology development [167, 168] we can expect that in the future, the technologies of extremely high frequencies will be applied to interconnections.

Another aspect of research which is worth investigating is the possibility of coupler's branch compensation with external elements (capacitors) which can reduce the effective branch length. In the literature, the new coupler design techniques to minimize length are present [169]. Furthermore, the dynamic method of coupler tuning based on varactor diodes should be considered [170, 171]. This approach, in combination with appropriate algorithms, could enable the possibility of auto-adjusting the coupler to current measurement conditions.

The resonant length decrease can be obtained by the appropriate coupler's substrate selection. Commercially available discrete couplers for general purpose applications [172, 173, 174] prove that currently available technology offers great opportunities and proper materials selection gives the wide field for research. A related research issue which could be dealt with is the coupler's geometry modifications which would allow overhearing the transmission not only along the straight sections of lines but also on the bends. This is the next aspect which could increase the range of potential applications and use cases.

As the last step, the complete measurement head based on physical construction presented in Fig. 4.74 could be developed. The signal decoupled by the

differential signal coupled from the transmission line under test should be processed with an equalizer, and a detector realized in IC technology which should be placed on the top of the construction. The IC should additionally realize the coupler compensation function with an auto adjust algorithm, a limiter [175] and process the decoupled signal. Finally, the head should be equipped with the high speed link which will enable transferring the results to PC. The PC will host the application for visual presentation of the obtained results and an interface for device configuration.

Bibliography

[1] M. R. Wiliams. *What Does It Mean To Be The First Computer?* International Symposium on Modern Computing, Pages 3-9, JVA '06, 2006. [cite on page 1]

[2] B. Bridger. *An Earlier Kind of Computer.* IEEE Industry Applications Magazine, Vol. 13, No. 5, Pages 8-10, September/October 2007. [cite on page 1]

[3] R. G. Arns. *The Other Transistor: Early History of the Metal-Oxide-Semiconductor Field-Effect Transistor.* Engineering Science and Education Journal, Vol. 7, No. 5, Pages 233-240, October 1998. [cite on page 1]

[4] M. Mills. *Hearing Aids and the History of Electronics Miniaturization.* IEEE Annals to the History of Computing, Vol. 33, No. 2, Pages 24-45, 2011. [cite on page 1]

[5] A. B. Frazier, O. Warrington, C. Friedrich. *The Miniaturization Technologies: Past, Present and Future.* IEEE Transactions on Industrial Electronics, Vol. 42, No. 5, Pages 423-430, October 1995. [cite on page 1]

[6] B. T. Murphy, D. E. Haggan, W. W. Troutman. *From Circuit Miniaturization to the Scalable IC.* Proceedings of IEEE, Vol.88, No. 5, Pages 691-703, May 2000. [cite on page 1]

[7] E. Mollick. *Establishing Moore's Law.* IEEE Annals of the History of Computing, Vol. 28, No. 3, Pages 62-75, July/September 2006. [cite on page 1]

[8] C. A. Mack. *Fifty Years of Moore's Law.* IEEE Trasactions on Semiconductor Manufacturing, Vol. 24, No. 2, Pages 202-207, May 2011. [cite on page 1]

[9] K. Ahdoot, R. Alvarodiaz, L. Crawley. *IBM FSD Chip Design Methodology.* 20th Conference on Design Automation, Pages 39-45, 1983. [cite on page 1]

[10] C. P. Sandbank, P. J. A. McKeown. *New Interconnection Techniques for Multichip and Hybrid Integrated Circuits.* Proceedings of The IEEE, Vol. 52, No. 12, Pages 1655-1657, December 1964. [cite on page 1]

[11] J. Bargowski, S. G. Konsowski, G. D. Spencer. *Interconnection of Monolithic Integrated Circuits Through the Use of Advanced Materials and Techniques.* IEEE Transactions on Parts, Materials and Packaging, Vol. 2, No. 4, Pages 90-98, December 1966. [cite on page 1]

[12] A. R. Owens, K. A. Jaggers. *Pulse Response of Interconnections in Silicon Integrated Circuits.* Proceedings of The IEEE, Vol. 121, No. 7, Pages 541-547, July 1974. [cite on page 1]

[13] A. E. Ruehli. *Survey of Computer-Aided Electrical Analysis of Integrated Circuit Interconnections.* IBM Journal of Research and Development, Vol. 23, No. 6, Pages 626-639, November 1979. [cite on page 1]

[14] A. K. Sinha, J. A. Cooper, H. J. Levistein. *Speed limitations Due to Interconnect Time Constants in VLSI Integrated Circuits.* IEEE Electron Device Letters, Vol. 3, No. 4, Pages 90-92, April 1982. [cite on page 1]

[15] A. Tsuchiya, Y. Gotoh, M. Hashimoto, H. Onodera. *Performance Limitation of On-Chip Global Interconnects for High-Speed Signaling.* IEEE 2004 Custom Integrated Circuits Conference, Pages 489-492, 2004. [cite on page 1]

[16] C. Romero, P. Seungwook, M. Park Y. Kweon. *Advanced high density interconnection substrate for mobile platform application.* 6th International Microsystems, Packaging, Assembly and Circuits Technology Conference (IMPACT), Pages 214-217, 2011. [cite on page 1]

[17] E. T. Lewis. *High-Density High-Impedance Hybrid Circuit Technology for Gigahertz Logic.* IEEE Transactions on Components, Hybrids and Manufacturing Technology, Vol. CHMT-2, No. 4, 1979. [cite on page 2]

[18] H. L. Parks. *Batch-Fabricated Three-Dimensional Planar Coaxial Interconnections for Microelectronic Systems.* IEEE Transactions on Computers, Vol. C-20, No. 5, 1971. [cite on page 2]

[19] R. C. Swengel, T. A. Lemke, F. P. Villiard. *A Coaxial Interconnection System for High Speed Digital Processors.* IEEE Transactions on Parts, Hybrids and Packaging, Vol. PHP-10, No. 3, 1974. [cite on page 2]

[20] O. A. Horna. *Nonlinear Termination of Transmission Lines.* IEEE Transactions on Computers, Vol. C-21, No. 9, 1972. [cite on page 2]

[21] S. Rosłoniec. *Design of Coupled Microstrip Lines by Optimization Methods.* IEEE Transactions on Microwave Theory and Techniques, Vol. MTT-35, No. 11, 1987. [cite on page 2]

[22] R. Reitmeyer. *CAD For Military Systems, an Essential Link to LSI, VLSI and VHSIC Technology.* 18th Conference on Design Automation, Pages 3-12, 1981. [cite on page 2]

[23] N. Chandler, S. G. Tyler. *High Interconnection Density - Current Trends.* IEE Colegium on Advanced in Interconnection Technology, Pages 1-4, 1991. [cite on page 2]

[24] M. Honda, T. Hayashi. *A Technique of Automatic Engineering Change for Multilayer Printed-Circuit Boards.* IEEE Transactions on Manufacturing Technology, Vol. 3, No. 2, Pages 88-95, December 1974. [cite on page 2]

[25] R. Y. Tsui, R. J. Smith. *A High-Density Multilayer PCB Router Based on Necessary and Sufficient Conditions for Single Row Routing.* 18th Conference on Design Automation, Pages 372-381, 1981. [cite on page 2]

[26] H. Andou, I. Yamamoto, Y. Mori, Y. Koike, K. Shouji, K. Hirakawa. *Automatic Routing Algorithm for VLSI.* 22th Conference on Design Automation, Pages 785-788, 1985. [cite on page 2]

[27] A. Handkiewicz. *Automated DCT Layout Generation Using AMPLE Language.* MIXDES 2010, 17th International Conference Mixed Design of Integrated Circuits and Systems, 2010. [cite on page 2]

[28] A. Handkiewicz. *Silicon Compilers.* A Guide to CMOS Circuit Design Mixed-Signal Systems, 2002. [cite on page 2]

[29] P. Katarzynski, A. Handkiewicz, S. Szczesny, M. Melosik, M. Naumowicz. *Design of Elliptic Filters with Phase Correction by Using Genetic Algorithm.* MIXDES 2009, 16th International Conference Mixed Design of Integrated Circuits and Systems, 2009. [cite on page 2]

[30] J. Chramiec, B. Janiczak, J. Komisarczuk, K. J. Piotrowski, W. Gwarek. *CAD Models of Connectors and Transitions Used in Hybrid Microwave Integrated Circuits.* 28th European Microwave Conference, Vol. 1, 1998. [cite on page 2]

[31] A. Lamecki, M. Mrozowski. *Equivalent SPICE Circuits With Guaranteed Passivity From Nonpassive Models.* IEEE Transactions on Microwave Theory and Techniques, Vol. 55, No. 3, 2007. [cite on page 2]

[32] A. Dziekonski, P. Sypek, A. Lamecki, M. Mrozowski. *Accuracy, Memory, and Speed Strategies in GPU-Based Finite-Element Matrix-Generation.* IEEE Antennas and Wireless Propagation Letters, Vol. 11, Pages: 1346-1349, 2012. [cite on page 2]

[33] P. Kozakowski, M. Mrozowski, W.Zieniutycz. *Synthesis of Nonuniformly Spaced Arrays Using Genetic Algorithm.* Asia-Pacific Conference on Environmental Electromagnetics, CEEM 2003, Pages: 302-305, 2003. [cite on page 2]

[34] A. Kucharski. *Application of Equivalence Principle Domain-Decomposition Method to Electromagnetic Scattering by Complex Bodies-of-Revolution.* IEEE Antennas and Propagation Society International Symposium, Pages: 1-4, 2008. [cite on page 2]

[35] V. Ricciuti. *Power Bus Signal Integrity Improvement and EMI Mitigation on Multilayer Highh-Speed Digital PCBs with Embedded Capacitance.* IEEE Transactions on Mobile Computing, Vol. 2, No. 4, Pages 314-321, October/December 2003. [cite on page 2]

[36] K. Yamagishi, T. Ishibashi, H. Ohashi, S. Saito. *A Study on High-Speed Transmission Characteristics of Interconnections from PCB to Chip.* IEEE 9th VLSI Packaging Workshop of Japan, Pages 81-84, 2008. [cite on page 2]

[37] F. Gisin, Z. Pantic-Tanner. *Design Advances in PCB/Backplane Interconnects for the Propagation of High Speed Gb/s Digital Signals.* 6th International Conference on Telecommunications in Modern Satelite, Cable and Broadcasting Service, TELSIKS 2003, Vol. 1, Pages 184-191, October 2003. [cite on page 2]

[38] J. Jing, K. Lingwen. *Study of Signal Integrity for PCB Level.* 11th International Conference on Electronic Packaging Technology and High Density Packaging, Pages 828-833, 2010. [cite on page 2]

[39] A. Geczy, Z. Illyefalvi-Vitez. *Investigating PCB Traces for Fine Pitch Applications.* IEEE 16th International Symposium for Design and Technology in Electronic Packaging (SIITIME), Pages 147-152, 2010. [cite on page 2]

[40] D. Bem, M. Nawrocki, T. Wieckowski, R Zielinski. *Co-existance EMC Aspects of DECT Wireless Local Loops (WLL) and DECT Cordless Telephones.* Vehicular Technology Conference, Vol. 4, 2001. [cite on page 2]

[41] R. Nakatsu, C. Edirisinghe. *The Role of Movies and Telephony in the History of Communication Media.* Second International Conference on Culture and Computing, Pages 69-73, 2011. [cite on page 2]

[42] A. Oredope, V. Pham, B. Evans. *Deploying IP Multimedia Subsystem (IMS) Services in Future Mobile Networks.* National Conference on Communications (NCC), Pages 1-5, 2011. [cite on page 2]

[43] C. K. Shi, X. M. Hao, R. S. Sharma. *A Cross Market Study of Mobile Data Services and Devices.* 2010 IEEE International Conference on Management of Innovation and Technology (ICMIT), Pages 455-461, 2010. [cite on page 2]

[44] R. T. James. *High-speed information channels.* IEEE Spectrum, VOL. 3, No. 4, Pages 79-95, 1966. [cite on page 2]

[45] A. Righetti, F. Fontana, G. Delrosso, G. Grasso, M. Z. Iqbal, J. L. Gimlett, R. D. Standley, J. Young, N. K. Cheung, E. J. Tarbox. *11 Gbit/s, 260km Transmission Experiment Using a Directly-Modulated 1536nm DFB Laser With Two Er-Doped Fibre Amplifires and Clock Recovery.* Electronic Letters, VOL. 26, No. 5, Pages 330-332, 1990. [cite on page 2]

[46] W. Bandurski. *Metody analizy i symulacji połaczeń w szybkich układach cyfrowych.* Wydawnictwo Politechniki Poznańskiej, 2006. [cite on page 3]

[47] C. M. Albina, G. Hackl. *Layout Parasitic Interconnections Effects on High Frequency Circuits.* 6th IEEE Dallas Circuits and Systems Workshop on System-on-Chip (DCAS), Pages 1-4, 2007. [cite on page 3]

[48] C. A. Ridgeway, H. S. Sangha. *Making the move to serial buses.* EDN Magazine 3/2005, February 2005. [cite on page 4, 5, 128]

[49] G. Shiue, W. Guo, C. Lin, R. Wu. *Noise Reduction Using Compensation Capacitance for Bend Discontinuities of Differential Transmission Lines.* IEEE Transactions on Advanced Packaging, Vol. 29, No. 3, Pages 560-569, 2006. [cite on page 5]

[50] Y. Nishi, K. Abe, J. Ribo, B. Roederer, A. Gopalan, M. Benmansour, A. Ho, A. Bhoi, M. Kanishi, R. Mariizumi, V. Pathak, S. Gondi. *An ASIC-Ready 1.25-6.25Gb/s SerDes in 90nm CMOS with Multi-Standard Compatibility.* IEEE Asian Solid-State Circuits Conference, Pages 37-40, Japan, November 2008. [cite on page 5]

[51] P. Śniatała, J. Pierzchlewski, A. Handkiewicz, B. Nowakowski. *CPLD Based Development Board for Mixed Signal Chip Testing.* MIXDES 2007, 14th International Conference Mixed Design of Integrated Circuits and Systems, 2007. [cite on page 6]

[52] M. Zmuda, S. Szczepański. A new approach for high speed data transmission monitoring. *XI International PhD Workshop OWD 2009, Pages 60-63*, 17-20 October 2009. [cite on page 6, 36, 53]

[53] M. Zmuda, S. Szczepański, S. Kozieł. *The Contact-Less Method of Chip-To-Chip High Speed Data Transmission Monitoring.* XII Krajowa Konferencja Elektroniki, KKE, 2013. [cite on page 6, 56]

[54] M. Zmuda, S. Szczepański, S. Kozieł, S. Graczyk. *High Speed Chip-To-Chip Data Transmission Monitoring Using Microstrip Coupler.* Politechnika Gdańska, Wydział Elektroniki Telekomunikacji i Informatyki, Raport Badawczy Nr 6/2013, 2013. [cite on page 6, 36, 56]

[55] M. Zmuda, S. Szczepański, S. Kozieł. *Design of Novel Microstrip Directional Coupler for Differential Signal Decoupling.* IET Microwave, Antennas and Propagation, Vol. 6, No. 7, Pages 721-728, 2012. [cite on page 6, 36, 52]

[56] M. Zmuda, S. Szczepański, S. Kozieł. *A New Coupler Concept for Contactless High-Speed Data Transmission Monitoring.* IEEE Transactions on Instrumentation and Measurement, Vol. 62, No. 2, Pages 328-334, 2012. [cite on page 6, 36, 52, 53, 55, 132]

[57] M. Zmuda, S. Szczepański, S. Kozieł. *Microstrip differential signal coupler. Concept, design and applications.* XII Krajowa Konferencja Elektroniki, KKE, 2012. [cite on page 6, 52, 53, 55, 132]

[58] D. Derickson, M. Muller. *Digital Communications Test and Measurement: High-Speed Physical Layer Characterization.* Prentice Hall, 2007. [cite on page 9, 10, 11, 23, 28, 38]

[59] *PCI Express 2.0 Base Specification. Revision 0.9.* PCI-SIG, 2006. [cite on page 10, 70]

[60] S. H. Hall, H. L. Heck. *Advanced Signal Integrity for High-Speed Digital Designs.* Wiley-IEEE Press, 2009. [cite on page 11, 12, 21, 22, 23, 24, 25, 26, 32]

[61] B. Janiczak. *Behaviour of Guided Modes in Systems of Parallelly Located Transmission Lines on Dielectric Substrates.* Electronics Letters, Vol. 19, No. 19, Pages 778-779, 1983. [cite on page 12]

[62] B. J. Janiczak. *Accurate Hybrid-Mode Approach for Computing Modes in Three-Line Coupled Microstrip Structure in Overlaid Configuration.* Electronics Letters, Vol. 20, No. 20, Pages 825-826, 1984. [cite on page 12]

[63] B. J. Janiczak. *Phase Velocity Compensation in Three-Line Coupled Microstrip Structure by Using Stratified Dielectric Substrate.* Electronics Letters, Vol. 21, No. 4, Pages 145-146, 1985. [cite on page 12]

[64] B. J. Janiczak. *Phase Constant Characteristics of Generalized Asymmetric Three-Coupled Microstrip Lines.* IEE Proceedings H Microwave, Antennas and Propagation, Vol. 132, No. 1, Pages 23-26, 1985. [cite on page 12]

[65] B. P. Lathi. *Modern Digital and Analog Communication Systems.* CBS College Publishing, 1983. [cite on page 12]

[66] D. M. Pozar. *Microwave Engineering.* John Wiley and Sons Inc., 2005. [cite on page 13, 14, 16, 20, 22, 39, 40, 41, 44, 45]

[67] H. Johnson, M. Graham. *High-Speed Signal Propagation: Advanced Black Magic.* Prentice Hall, 2003. [cite on page 14]

[68] J. Carr. *Microwave & Wireless Communications Technology.* Newnes, 1996. [cite on page 15]

[69] T. Morawski, W. Gwarek. *Pola i Fale Elektromagnetyczne.* Wydawnictwo WNT, 2006. [cite on page 15]

[70] T. Williams. *The Circuit Designer's Companion, 2nd Edition.* Newnes, 2004. [cite on page 16]

[71] L. Maloratsky. *Passive RF & Microwave Integrated Circuits.* Newnes, 2003. [cite on page 18, 19, 41]

[72] E. O. Hammerstard. *Equations for Microstrip Circuit Design.* Proc. of the European Microwave Conference, Pages 268-272, September 1975. [cite on page 18, 157]

[73] I. J. Bahl, D. K. Trivedi. *A Designer's Guide to Microstrip Line.* Microwaves, May 1977. [cite on page 18, 157]

[74] M. D. Abouzahra, L. Lewin. *Radiation from Microstrip Discontinuities.* IEEE Transaction on Microwave Theory Tech., Vol. 27, No. 8, Pages 722-723, August 1979. [cite on page 18]

[75] H. A. Wheeler. *Transmission-Line Properties of a Strip Line Between Parallel Planes.* IEEE Transactions on Microwave Theory Tech., Vol. MTT-26, No. 11, Pages 866-876, November 1978. [cite on page 19, 159, 160]

[76] E. Sedek, P. Gajewski, A. Jeziorski. *Microstrip Monopulse Array Antenna.* 18th International Conference on Microwave Radar and Wireless Communications (MIKON), Pages: 1-3, 2010. [cite on page 20]

[77] Y. Yashchyshyn, J. Modelski. *A Reconfigurable Leaky-Wave Microstrip Antenna.* European Microwave Conference, Vol. 1, 2005. [cite on page 20]

[78] M. Pergol, W. Zieniutycz. *Mutual Coupling of Elliptical Microstrip Resonators.* 6th European Conference on Antennas and Propagation (EUCAP), Pages: 977-979, 2012. [cite on page 20]

[79] M. Pergol, W. Zieniutycz, M. Mazur. *Broadband Microstrip Patch Antenna with Reduced Transversal Size.* 18th International Conference on Microwave Radar and Wireless Communications (MIKON), Pages: 1-3, 2010. [cite on page 20]

[80] W. Zieniutycz. *Application of Hybrid Radiation Modes of Microstrip Line in Rectangular Patch Antennas Design.* 17th International Conference Radioelektronika, 2007, Pages: 1-7, 2007. [cite on page 20]

[81] M. Kitlinski, T. Borodo. *Improved compact low-profile quadband planar monopole antenna for mobile handsets.* International Conference on Microwaves, Radar & Wireless Communications, MIKON, Pages: 736-739, 2006. [cite on page 20]

[82] D. Bem, P. Kabacik. *Microstrip Phased Array for Mobile Satellite Terminals.* International Symposium of Antennas and Propagation Society , Vol. 3, Pages: 1446-1449, 1995. [cite on page 20]

[83] A. Kucharski. *Integral Equation Macromodel of a Slot-Excited Microstrip Antenna.* Proceedings of the Fourth European Conference on Antennas and Propagation (EuCAP), Pages: 1-4, 2010. [cite on page 20]

[84] D. Smolyansky. *Discussing the limitations and accuracies of time and frequency domain analysis of physical layer devices.* IEC DesignCon, Santa Clara, CA, 2007. [cite on page 20]

[85] R. Schaefer. *Discussing the limitations and accuracies of time and frequency domain analysis of physical layer devices.* IEC DesignCon, Santa Clara, CA, 2005. [cite on page 20]

[86] E. Bogatin. *Signal and Power Integrity—Simplified, Second Edition.* Prentice Hall, 2009. [cite on page 20, 26, 27, 28]

[87] K. S. Oh, X. C. Yuan. *High-Speed Signaling: Jitter Modeling, Analysis, and Budgeting.* Prentice Hall, 2011. [cite on page 20, 25, 26, 28, 32]

[88] TDA Systems. *TDR Technique for Characterization and Modeling of Electronic Packaging.* High-Density Interconnect Magazine, Pages 172-174, april 2001. [cite on page 23, 25]

[89] T. Stefański, B. J. Janiczak. *Experimental and Numerical Investigation of Crosstalk Effect in Coupled Coplanar Waveguides - Part I: Bi-Mode Coupled Line Representation.* IEEE Transactions on Electromagnetic Compatibility, Vol. 48, No. 4, 2006. [cite on page 26]

[90] T. Stefański, B. J. Janiczak. *Experimental and Numerical Investigation of Crosstalk Effect in Coupled Coplanar Waveguides - Part II: Multimode Coupled Line Representation.* IEEE Transactions on Electromagnetic Compatibility, Vol. 48, No. 4, 2006. [cite on page 26]

[91] A. S. Cimiński, B. J. Janiczak. *Cross-Talk Modeling in Coupled Transmission Lines Terminated with Nonlinear Load.* MIKON 2006, International Conference on Microwaves, Radar and Wireless Communications, Pages 390-393, 2006. [cite on page 26]

[92] B. J. Janiczak A. s. Cimiński. *Mixed Time/Frequency-Domain Modeling of Cross-Talk Phenomena in Coupled Microstrip Lines Terminated with Digital Circuit.* 18th International Zurich Symposium on Electromagnetic Compatibility, EMC Zurich 2007, Pages 115-118, 2007. [cite on page 26]

[93] T. Ciamulski, W. Gwarek. *A Study of Feeding Options Aimed at Canceling Crosstalk in Multiconductor Transmission Lines.* IEEE MTT-S International Microwave Symposium Digest, Vol. 3, 2004. [cite on page 27]

[94] T. Ciamulski, W. Gwarek. *On Eliminating Crosstalk Within Multiconductor Transmission Lines.* IEEE Microwave and Wireless Components Letters, Vol. 14, No. 6, 2004. [cite on page 27]

[95] W. Gwarek, C. Mroczkowski. *A Inhomogeneous Two-Dimensional Model for the Analysis of Microstrip Discontinuities.* IEEE Transactions on Microwave theory and Techniques, Vol. 39, No. 9, 1991. [cite on page 27]

[96] D. Brooks. *Signal Integrity Issues and Printed Circuit Boards.* Prentice Hall, 2003. [cite on page 29]

[97] G. Lawday, D. Ireland, G. Edlund. *A Signal Integrity Engineer's Companion. Real-Time Test and Measurement and Design Simulation.* Printice Hall Signal Integrity Library, 2008. [cite on page 30, 36, 37, 128, 129, 137]

[98] S. Vishram, W. H. Ryu, M. J. Choi. *Power Integrity for I/O Interfaces: With Signal Integrity/Power Integrity Co-Design.* Prentice Hall, 2010. [cite on page 31]

[99] Maximum Integrated. *Designing a sample, small, wide-band and low-power equalizer for FR4 copper link.* DesignCon, 2003. [cite on page 32]

[100] A. Palaniappan, S. Palermo. *A Design Methodology for Power Efficiency Optimization of High-Speed Equalized-Electrical I/O Architectures.* IEEE Transactions on Very Large Scale Integration (VLSI) Systems, 2012. [cite on page 33]

[101] K. Balasubramanian, S. S. Agili, A. Morales. *Encoding and Compensation Schemes Using Improved Pre-Equalization for the 64B/66B Encoder.* IEEE International Conference on Consumer Electronics (ICCE), Pages 361-363, 2012. [cite on page 33]

[102] C. H. Lee, M. T. Mustaffa, K. H. Chan. *Comparison of Receiver Equalization Using First-Order and Second-Order Continuous-Time Linear Equalizer in 45nm Process Technology.* 4th International Conference on Intelligent and Advanced Systems (ICIAS2012), Vol. 2, Pages 795-800, 2012. [cite on page 33]

[103] J. Wilson, L. Luo, S. Mick, E. Erickson, H. Su, B. Chan, H. Lin, P. Franyon. *AC Coupled Interconnect using Buried Bumps for Laminated Organic Packages.* Electronic Components and Technology Conference, Pages 41-48, 2006. [cite on page 33, 34]

[104] Z. Wang, M. Hsieh, Z. Wu, C. Liu, H. Chiu, B. Lin, C. Chen. *A 12 Gb-2 Chip-to-Chip AC Coupled Transceiver.* IEEE International Symposium on Circuits and Systems (ISCAS), Pages 1692-1695, 2011. [cite on page 33, 34, 38]

[105] R. Ho, R. Drost. *Coupled Data Communication Techniques for High-Performance and Low-Power Computing.* Springer Science-Business Media, 2010. [cite on page 34]

[106] D. Ihuchi, Y. Akiyama, T. Ito, K. Otsuka. *Proximity Interconnect Technology Utilizing Transmission Line Coupling for Stacked VLSI Chips.* IEEE EPEP Electrical Performance of Electronic Packaging, Pages 291-294, 2008. [cite on page 34, 35]

[107] M. Saito, Y. Yoshida, N. Miura, H. Ishikuro, T. Kuroda. *47 % Power Reduction and 91% Area Reduction in Inductive-Coupling Programable Bus for NAND Flash Memory Stacking.* IEEE Transactions on Circuits and Systems I, Vol. 57, No. 9, Pages 449-452, 2010. [cite on page 34, 38]

[108] D. Iguchi, Y. Akiyama, F. Fujii, K. Otsuka. *A Feasibility Study of Proximity Interconnect Technology Utilizing Transmission Line Coupling.* IEEE CONT Symposium, Japan, Pages 1-4, 2010. [cite on page 34, 38, 51, 52, 132]

[109] T. Takeya, L. Nan, S. Nakano, N. Miura, H. Ishikuro, T. Kuroda. *A 12-Gb/s Non-Contact Interface With Coupled Transmission Lines.* IEEE Journal Solid-State Circuits, Vol. 48, No. 3, Pages 790-800, 2013. [cite on page 34, 132]

[110] X. Ye. *Intentional and Un-Intentional Far End Crosstalk Cancellation in High Speed Differential Link.* IEEE International Symposium on Electromagnetic Compatibility (EMC), Pages 791-796, 2011. [cite on page 35]

[111] C. Huang, C. Wu, C. Shih. *Phase Redress for the Bend on Differential Microstrip Lines.* XXXth General Assembly and Scientific Symposium URSI, Pages 1-4, 2011. [cite on page 35]

[112] G. Schiue, W. Guo, C. Lin, R. Wu. *Noise Reduction Using Compensation Capacitance for Bend Discontinuities of Differential Transmission Lines.* IEEE Transactions on Advanced Packaging, Vol. 29, No. 3, Pages 560-569, 2006. [cite on page 36]

[113] L. Wang, Y. Chang, K. Cheng. *Electronic Design Automation.* Morgan Kaufmann, 2009. [cite on page 36]

[114] M. Hosman. *High-Speed Bus Debug and Validation Test Challenges.* IEEE/SEMI International Electronics Manufacturing Technology Symposium, Pages 218-222, 2004. [cite on page 36, 128]

[115] Y. Fan, Z. Zilic. *A Versatile Scheme for the Validation, Testing and Debugging of High Speed Serial Interfaces.* IEEE International High Level Design Validation and Testing Workshop, Pages 114-121, 2009. [cite on page 36, 128]

[116] R. McLaughlin, S. Venkataraman, C. Lim. *Automated Debug of Speed Path Failures Using Functional Tests.* 27th IEEE VLSI Test Symposium, Pages 91-96, 2009. [cite on page 36, 128]

[117] W. Redman-White, M. Bugbee, S. Dobbs, X. Wu, R. Balmford, J. Nuttgens, U. S. Kiani, R. Clegg, G. W. den Besten. *A Robust High Speed Serial PHY Architecture With Feed-Forward Correction Clock and Data Recovery.* IEEE Journal of Solid-State Circuits, Vol.44, No. 7, Pages 1914-1926, 2009. [cite on page 38]

[118] R. Mongia, I. Bahl, P. Bhartia. *RF and Microwave Coupled-Line Circuits.* Artech House Microwave Library, 1999. [cite on page 39, 40, 41, 42, 43, 44, 45, 46, 55]

[119] B. Janiczak, J. Chramiec, M. Kitlinski. *On the Design of Planar High Directivity Proximity Couplers in the MM-Wave Range.* International Conference on Microwaves, Radar & Wireless Communications, MIKON, Pages: 350-353, 2006. [cite on page 39]

[120] S. Gruszczynski, K. Wincza, K. Sachse. *Design of Compensated Coupled-Stripline 3-dB Directional Couplers, Phase Shifters and Magic-T —*

Part I: Single-Section Coupled-Line Circuits. IEEE Transactions on Microwave Theory and Techniques, Vol. 54, No. 11, Pages: 3994-3507, 2006. [cite on page 39]

[121] S. Gruszczynski, K. Wincza, K. Sachse. *Design of Compensated Coupled-Stripline 3-dB Directional Couplers, Phase Shifters, and Magic-T—Part II: Broadband Coupled-Line Circuits.* IEEE Transactions on Microwave Theory and Techniques, Vol. 54, No. 9, Pages: 3501-3507, 2006. [cite on page 39]

[122] J. A. Dobrowolski. *Technika Wielkich Czestotliwości.* Wydawnictwo Politechniki Warszawskiej, 2001. [cite on page 39]

[123] J. Mazur, M. Solecka, M. Mazur, R. Poltorak, E. Sedek. *Design and measurement of gyrator and isolator using ferrite coupled microstrip lines.* IEEE Proceedings on Microwaves, Antennas and Propagation, Vol. 152, No. 1, Pages: 43-46, 2005. [cite on page 47]

[124] J. Michalski, M. Mazur, J. Mazur. *Scattering in a section of ferrite-coupled microstrip lines: theory and application in nonreciprocal devices.* IEEE Proceedings Microwaves, Antennas and Propagation, Vol. 149 , No. 56, Pages: 286-290, 2002. [cite on page 47]

[125] J. Mazur, M. Solecka, M. Mazur. *Theoretical and experimental treatment of a microstrip coupled ferrite line circulator.* IEEE Proceedings Microwaves, Antennas and Propagation, Vol. 151, No. 6, Pages: 477-480, 2004. [cite on page 47]

[126] A. Eroglu, J. K .Lee. *The Complete Design of Microstrip Directional Couplers Using the Synthesis Technique.* IEEE Transactions on Instrumentation and Measurements, Vol. 57. No. 12, Pages 2756-2761, 2008. [cite on page 47]

[127] G. Vandersteen, A. Barel, Y. Rolain. *Broadband High Frequency Differential Coupler.* IEEE Instrumentation and Measurement Technology Conference, Vol. 3, Pages 1879-1902, 2001. [cite on page 50]

[128] S. B. Sanders, Motorola Inc. *Method and Apparatus for Coupling a Differential Signal to an Unbalanced Port.* United States Patent, 1998. [cite on page 51]

[129] C. Hwan, Y. Jae-Ho, K. Hyeong-Seok, P. Jun-Seok, L. Jeong-Hae, J. Hyun-Kyo. *Optimization of A Microstrip Directional Coupler with High Performance Using Evolution Strategy.* 32nd European Microwave conference, Pages: 1-4, 2002. [cite on page 55]

[130] K. Yamamoto, H. Kurusu, S. Suzuki, M. Miyashita. *High-Directivity Enhancement With Passive and Active Bypass Circuit Techniques for GaAs MMIC Micristrip Directional Couplers.* IEEE Transactions on Microwave Theory and Techniques, Vol. 59, No. 12, Pages 3095-3107, 2011. [cite on page 55]

[131] S. Lee, Y. Lee. *A Design Method for Microstrip Directional Couplers Loaded With Shunt Inductors for Directivity Enhancement.* IEEE Transactions on Microwave Theory and Techniques, Vol. 58, No. 4, 2010. [cite on page 55]

[132] Y. Wu, W. Sun, W. Leung, Y. Diao, K. Chan, Y. Siu. *Single-Layer Microstrip High-Directivity Coupled-Line Coupler With Tight Coupling.* IEEE Transactions on Microwave Theory and Techniques, Vol. 61, No. 2, 2013. [cite on page 55]

[133] J. Muller, C. Friesicke, A. Jacob. *Stepped Impedance Microstrip Couplers with Improved Directivity.* IEEE MTT-S International Microwave Symposium Digest, Pages 621-624, 2009. [cite on page 55, 56, 96, 97, 137]

[134] S. L. March. *Phase Velocity Compensation in Parallel-Coupled Microstrip Line.* IEEE MTT-S Int. Microwave Sump. Dig., 1982. [cite on page 55, 97, 100]

[135] B. J. Janiczak. *Phase Velocity Compenstaion in Three-Line Coupled Microstrip Structure by Using Stratified Dielectric Substrate.* Electronic Letters, Vol. 21, No. 4, 1985. [cite on page 55]

[136] S. Rehnmark. *High Directivity CTL-Couplers and a New Technique for the Measurement of CTL-Coupler Parameters.* IEEE MTT-S International Microwave Symposium Digest, Pages: 495-498, 1977. [cite on page 55, 56]

[137] *Agilent EEsof EDA E8921A/AN Momentum. Product Overview.* Agilent Technologies, 2009. [cite on page 58]

[138] *RO4000 Series. High Frequency Circuit Materials.* Roggers Corporation, 2011. [cite on page 74]

[139] S. Rosłoniec. *Design of Stepped Transmission Line Matching Circuits by Optimization Methods.* IEEE Transactions on Microwave Theory and Techniques, Vol. 42, No. 12, 1994. [cite on page 74]

[140] *N5224A and N5225A 2-Port and 4-port PNA Microwave Network Analyzers. User manual.* Tektronix Inc., 1993. [cite on page 74]

[141] *HFSS v10. High Frequency Structure Simulator.* Ansoft Corporation, 2005. [cite on page 79]

[142] M. Zmuda, S. Szczepański, S. Kozieł. *A Design and EM Full-Wave Simulation of Novel Microstrip Directional Coupler for Differential Signal Decoupling.* 27th Applied Computational Electromagnetics Society Conference, Pages: 1-5, 2012. [cite on page 79]

[143] *Agilent E5071C ENA Network Analyzer.* Agilent Technologies, 2011. [cite on page 85, 103]

[144] *FR-4 Printed Circuits Datasheet.* Leiton, 2012. [cite on page 85]

[145] *FR-4 Glass/Epoxy Laminates. Datasheet.* Plastic International, 2012. [cite on page 85]

[146] *Tuning, Optimization and Statistical Design. Agilent ADS User Guide.* Agilent Corporation, 2009. [cite on page 100]

[147] J. W. Bandler, H. C. Shao. *Circuit Optimization: The State of the Art.* IEEE Transactions on Microwave Theory and Techniques, Vol. 36, No. 2, Pages: 424-443, 1988. [cite on page 100]

[148] *ML605 Hardware User Guide.* Xilinx Inc., 2012. [cite on page 122]

[149] *Agilent InfiniiVision 7000B Series Osciloscopes. User's Guide.* Agilent Technologies, 2010. [cite on page 122]

[150] *Agilent X-Series Signal Analyzer. Spectrum Analyzer Mode User's and Programmer's Reference.* Agilent Technologies, 2012. [cite on page 122]

[151] *Pushing the Limits of PCI-Express: A PCIe Applications within an IBM Supercomputing Environment.* Electronic Componens and Technology Conference, 2008. [cite on page 128]

[152] A. Rysin, P. Livshits, S. Sofer, O. Mantel, Y. Shapira, Y. Fefer. *Inter-Symbol Interference (ISI) in on-die transmission lines.* IEEE International Conference on Microwaves, Communications, Antennas and Electronics Systems, Pages: 1-5, 2009. [cite on page 128]

[153] E. A. Daoud, N. Nicolici. *Real-Time Lossless Compression for Silicon Debug.* IEEE Transactions on Computer-Aided Design of Integrated Circuits and Systems, Vol. 28, No. 9, Pages: 1387-1400, 2009. [cite on page 128]

[154] B. Chia, R. Kollipara, D. Oh, C. Yuan, L. Boluna. *Study of PCB Trace Crosstalk in Backplane Connector Pin Field.* IEEE Conference on Electrical Performance of Electronic Packaging, Pages: 281-284, 2006. [cite on page 130]

[155] J. Fun, J. L. Drewniak, J. L Knighten, N. W. Smith, A. Orlandi, T. P. Van Doren, T. H. Hubing, R. E. DuBroff. *Quantifying SMT Decoupling Capacitor Placement in DC Power-Bus Design for Multilayer PCBs.* IEEE Transactions on Electromagnetic Compatibility, Vol. 43, No. 4, Pages: 588-599, 2001. [cite on page 130]

[156] P. Pathmanathan, C. M. Jones, S. G. Pytel, D. L. Edgar, P. G. Huray. *Power Loss due to Periodic Structures in High-Speed Packages and Printed Circuit Boards.* 18th European Conference on Microelectronics and Packaging (EMPC), Pages: 1-8, 2011. [cite on page 130]

[157] M. Kotzev, R. Rimolo-Donadio, Y. H. Kwark, C. W. Baks, X. Gu, C. Schuster. *Electrical Performance of the Recessed Probe Launch Technique for Measurement of Embedded Multilayer Structures.* IEEE Transactions on Instrumentation and Measurement, Vol. 61, No. 12, Pages: 3198-3206, 2012. [cite on page 130]

[158] K. C. Gupta, R. Garg, R. Chadha. *Computer-Aided Design of Microwave Circuits.* Artech House INC., 1981. [cite on page 131, 161, 163]

[159] J. Wysocki, R. Debouk, K. Nouri. *Shared Redundancy as a Means of Producing Reliable Mission Critical Systems.* Annual Symposium on Reliability and Maintainability RAMS, Pages: 376-381, 2004. [cite on page 131]

[160] C. Raghavendra, A. Varma. *Fault-Tolerant Microprocessors with Redundant-Path Interconnection Networks.* IEEE Transactions on Computers, Vol. C-35, No. 4, Pages: 307-316, 1986. [cite on page 131]

[161] S. Miura, T. Okomoto, T. Boku, T. Hanawa, M. Sato. *RI2N: High-Bandwidth and Fault-Tolerant Network with Multi-link Ethernet for PC Cluster.* IEEE International Conference on Cluster Computing, Pages: 274-279, 2008. [cite on page 131]

[162] *A Revolutionary Approach: Quad Redundancy Control.* GE Intelligent Platforms, Inc., 2012. [cite on page 131]

[163] P. Patre, S. Joshi. *Decentralized Adaptive Control of Systems with Uncertain Interconnections, Plant-Model Mismatch and Actuator Failures.* American Control Conference (ACC), Pages: 4201-4206, 2011. [cite on page 131]

[164] P. Livshits, A. Rysin, S. Sergey, Y. Fefer. *Assessment of Influence of Impedance Mismatch in ULSI Devices on Electromigration of Copper Interconnection Lines.* IEEE Transactions on Device and Materials Reliability, Vol. 13, No. 1, 2013. [cite on page 131]

[165] T. Kurabayashi, P. Plotka, J. Nishizawa, M. Watenabe. *Continuous millimeter-wave TUNNETT diode system for microanalytical applications.* Joint 32nd International Conference on Infrared and Millimeter Waves and the 15th International Conference on Terahertz Electronics. IRMMW-THz., Pages: 287-288, 2007. [cite on page 137]

[166] J. Nishizawa, T. Kurabayashi, P. Plotka, H. Makabe. *Continuous millimeter-wave TUNNETT diode system for inspection applications.* Joint 31st International Conference on Infrared Millimeter Waves and 14th International Conference on Teraherz Electronics, Pages: 414, 2006. [cite on page 137]

[167] J. A. Dobrowolski. *Uklady scalone CMOS na czestotliwości radiowe i mikrofalowe.* Wydawnictwo EXIT, 2008. [cite on page 137]

[168] J. A. Dobrowolski. *Monolityczne Mikrofalowe Układy Scalone.* Wydawnictwo WNT, 1999. [cite on page 137]

[169] W. Gwarek. *A New Approach to Design of Directional Couplers.* MIKON 2012, 19th International Conference on Microwaves, Radar and Wireless Communications, Vol. 2, 2012. [cite on page 137]

[170] M. Bury, S. Kozlowski, T. Morawski, J. Zborowska, D. Gryglewski, E. Sedek. *Phased Array Antenna with Varactor Phase Shifters.* 17th International Conference on Microwaves, Radar and Wireless Communications, MIKON, Pages: 1-4, 2008. [cite on page 137]

[171] D. Gryglewski, T. Morawski, E. Sedek, J. Zborowska. *Microwave Phase Shifters for Radar Applications.* International Conference on Microwaves, Radar and Wireless Communications, MIKON, Pages: 309-312, 2006. [cite on page 137]

[172] *DC08-73, DC08-73LF: Directional Coupler 0.3–2.7 GHz. Datasheet.* Skyworks Solutions Inc., 2012. [cite on page 137]

[173] *CP0805 SMD Thin-Film Directional Couplers. Datasheet.* AVX RF, 2012. [cite on page 137]

[174] J. Modelski, Y. Yashchyshyn. *Semiconductor and Ferroelectric Antennas.* Proceedings of Asia-Pacific Microwave Conference, Pages: 1052-1059, 2006. [cite on page 137]

[175] Z. Szczepaniak, A. Arvaniti, K. Sawicka-Szczepaniak, E. Sedek. *Nonlinear Resonant Circuits for Microwave Low Power Limiters.* IEEE Microwave and Wireless Components Letters, Vol. 17, No. 12, Pages: 870-872, 2007. [cite on page 138]

[176] R. A. Pucel, D. J. Masse, C. P. Hartwig. *Losses in Microstrip.* IEEE Transactions on Microwave Theory Tech., Vol.16, No. 8, Pages 342-350, December 1968. [cite on page 157, 158]

[177] M. V. Schneider. *Dielectric Loss in Integrated Microwave Circuits.* Bell System Technical Journal, October 2002. [cite on page 158]

Appendices

Appendix A

Microstrip lines

The characteristic impedance of the microstrip line (Fig. A.1) $Z_0[\Omega]$ can be calculated from the equations proposed in [72, 73]:

$$Z_0 = \frac{60}{\sqrt{\epsilon}} \ln\left(\frac{8h}{w} + \frac{w}{4h}\right) \qquad \text{for} \quad w/h \leq 1 \tag{A.1}$$

$$Z_0 = \frac{120\pi}{\sqrt{\epsilon}[w/h + 1.393 + 0.667\ln\left(w/h + 1.444\right)]} \qquad \text{for} \quad w/h > 1 \tag{A.2}$$

Wheller recommended to take into account the finite conductor thickness, it is necessary to define effective strip width w_{eff}:

$$w_{eff} = w + \Delta w \tag{A.3}$$

where

$$\Delta w = \frac{1}{\pi}\left(\ln\frac{2h}{T} + 1\right) \qquad \text{for} \quad w/h \geq 2\pi \tag{A.4}$$

$$\Delta w = \frac{1}{\pi}\left(\ln\frac{2h}{T} + 1\right) \qquad \text{for} \quad \frac{2T}{h} < w/h \leq \frac{1}{2\pi} \tag{A.5}$$

The conductor loss α_c[dB/unit length] for microstrip for range $1/2\pi < w/h < 2$ is expressed by equation [176]:

$$\alpha_c = \frac{8.68R_s}{2\pi Z_0 h}\left[1 - \left(\frac{w}{4h}\right)^2\right]\left[1 + \frac{h}{w} + \frac{h}{\pi w}\left(\ln\frac{2h}{T} - \frac{T}{h}\right)\right] \tag{A.6}$$

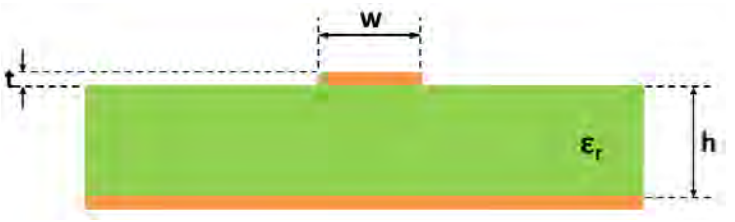

Figure A.1: Microstrip line

where R_s is conductor resistance. For cases when $w/h \leq 1/2\pi$ conductor losses α_c[dB/unit length] are:

$$\alpha_c = \frac{8.68 R_s}{2\pi Z_0 h}\left[1-\left(\frac{w}{4h}\right)^2\right]\left[1+\frac{h}{w}+\frac{h}{\pi w}\left(\ln\frac{4\pi w}{T}+\frac{T}{w}\right)\right] \tag{A.7}$$

The dielectric losses α_d [dB/unit length] can be calculated by equations presented in [176, 177]:

$$\alpha_d = 27.3\left(\frac{q\epsilon_r}{\epsilon_{eff}}\right)\frac{\tan\delta}{\lambda_0} \tag{A.8}$$

where q is a filling factor and is defined as:

$$q = \frac{\epsilon_{eff}-1}{\epsilon_r - 1} \tag{A.9}$$

Appendix B

Striplines

The characteristic impedance $Z_0[\Omega]$ of a stripline (Fig. B.1) can be calculated by [75]:

$$Z_0 = \frac{\eta}{2\pi\sqrt{\epsilon}} \ln\left\{1 + \frac{4(b-T)}{\pi w_{eff}}\left[\frac{8(b-T)}{\pi w_{eff}}\sqrt{\left(\frac{8(b-T)}{\pi w_{eff}}\right)^2 + 6.27}\right]\right\} \tag{B.1}$$

where

$$\eta = 120\pi \tag{B.2}$$

$$w_{eff} = w + \Delta w \tag{B.3}$$

$$\Delta w = \frac{T \cdot \ln\left[\frac{5(b-T)}{T}\right]}{3.2} \tag{B.4}$$

where T is the center conductor thickness. The total power losses of the stripline per length α[db/unit length] is described by a sum of substrate α_d and conductor α_c losses:

$$\alpha = \alpha_d + \alpha_c \tag{B.5}$$

The dielectric substrate loss α_d[db/unit length] depends on the substrate permittivity ϵ, substrate loss tangent $tan\delta$, frequency and thus wavelength λ:

$$\alpha_d = \frac{27.3\sqrt{\epsilon}\tan\delta}{\lambda} \tag{B.6}$$

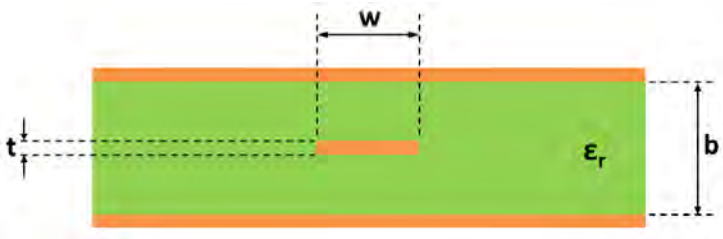

Figure B.1: Stripline

The conductor losses α_c[dB/unit length] depends on metal conductivity, magnetic permeability of the metal μ and the surface roughness. This parameter can be calculated by Wheller's incremental inductance rule [75]:

$$\alpha_c = \frac{23.4 \cdot 10^{-3} R_s \epsilon Z_0}{30\pi(b-T)} O \qquad \text{for } \sqrt{\epsilon} Z_0 < 120\Omega \tag{B.7}$$

$$\alpha_c = \frac{1.39 R_s}{Z_0 b} F \qquad \text{for } \sqrt{\epsilon} Z_0 \geq 120\Omega \tag{B.8}$$

where

$$O = 1 + \frac{2w}{b-T} + \frac{1}{\pi}\frac{b+T}{b-T}\ln\left(\frac{2b-T}{T}\right) \tag{B.9}$$

$$F = 1 + \frac{b}{0.5w + 0.7T}\left(0.5 + \frac{0.414T}{w} + \frac{1}{2\pi}\ln\frac{4\pi w}{T}\right) \tag{B.10}$$

$$R_s = \sqrt{\frac{\pi f \mu}{\sigma}} \tag{B.11}$$

Appendix C

Coupled Microstrip Lines

The even and odd mode characteristic impedances for a pair if coupled microstrip lines can be calculated as follow (Fig. C.1) [158]:

$$Z_{oe} = Z_0 \sqrt{\frac{1 + 10^{(M/20)}}{1 - 10^{(M/20)}}} \tag{C.1}$$

$$Z_{oo} = Z_0 \sqrt{\frac{1 - 10^{(M/20)}}{1 + 10^{(M/20)}}} \tag{C.2}$$

where M is the coupling factor [dB] and Z_0 is characteristic impedance [Ω]. The (s/h) can be calculation from relations:

$$s/h = \frac{2}{\pi} \cosh^{-1}(X) \tag{C.3}$$

$$X = \frac{\cosh\left[\frac{\pi}{2}\left(\frac{w}{h}\right)'_{so}\right] + \cosh\left[\frac{\pi}{2}\left(\frac{w}{h}\right)_{se}\right] - 2}{\cosh\left[\frac{\pi}{2}\left(\frac{w}{h}\right)'_{so}\right] - \cosh\left[\frac{\pi}{2}\left(\frac{w}{h}\right)_{se}\right]} \tag{C.4}$$

where h is a PCB substrate height, $(w/h)_{se}$ and $(w/h)_{so}$ are auxiliary parameters for even and odd modes respectively. The $(w/h)'_{so}$ is expressed as a sum of $(w/h)_{so}$ and $(w/h)_{se}$ with constant factors:

$$\left(\frac{w}{h}\right)'_{so} = 0.78\left(\frac{w}{h}\right)_{so} + 0.1\left(\frac{w}{h}\right)_{se} \tag{C.5}$$

Auxiliary parameters $(w/h)_{se}$ and $(w/h)_{so}$ are calculated by changing auxiliary parameter P to $(Z_{0o}/2)$ for $(w/h)_{so}$ and $(Z_{0e}/2)$ for $(w/h)_{se}$ in equation:

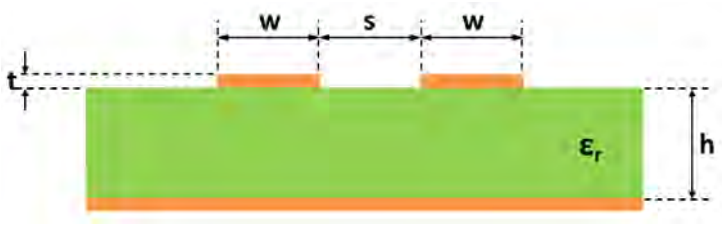

Figure C.1: Coupled microstrip lines

$$(w/h)_{se,so} = \frac{8\sqrt{\left[e^{\frac{P}{42.4}\sqrt{(\epsilon_r+1)}}-1\right]\frac{7+(4/\epsilon_r)}{11}+\frac{1+(1/\epsilon_r)}{0.81}}}{\left[e^{\frac{P}{42.4}\sqrt{(\epsilon_r+1)}}-1\right]} \tag{C.6}$$

where ϵ_r is a dielectric constant of substrate. Finally, the (w/h) ratio can be specified as:

$$(w/h) = \frac{1}{\pi}\cosh^{-1}(m) - \frac{1}{2}\left(\frac{s}{h}\right) \tag{C.7}$$

$$m = \frac{\cosh\left[\frac{\pi}{2}\left(\frac{w}{h}\right)_{se}\right](g+1)+g-1}{2} \tag{C.8}$$

$$g = \cosh\left[\frac{\pi}{2}\left(\frac{s}{h}\right)\right] \tag{C.9}$$

Appendix D

Coupled Striplines

For zero thickness coupled striplines (T=0) the even and odd mode impedances can be calculated with use of the conformal mapping procedure (Fig.D.1) [158]:

$$Z_{0e} = \frac{30\pi}{\sqrt{\epsilon_r}} \frac{K(k'_e)}{K(k_e)} \tag{D.1}$$

$$Z_{0o} = \frac{30\pi}{\sqrt{\epsilon_r}} \frac{K(k'_o)}{K(k_o)} \tag{D.2}$$

The coefficients k_e, k_o, k'_e and k'_o are defined as follow:

$$k_e = \tanh\left(\frac{\pi}{2}\frac{w}{b}\right)\tanh\left(\frac{\pi}{2}\frac{s+w}{b}\right), \quad k'_e = \sqrt{1-k_e^2} \tag{D.3}$$

$$k_o = \tanh\left(\frac{\pi}{2}\frac{w}{b}\right)\tanh\left(\frac{\pi}{2}\frac{s+w}{b}\right), \quad k'_o = \sqrt{1-k_o^2} \tag{D.4}$$

The quotients (w/b) and (s/b) can be calculated using the following relations:

$$(w/h) = \frac{2}{\pi}\tanh^{-1}\sqrt{k_e k_o} \tag{D.5}$$

$$(s/h) = \frac{2}{\pi}\tanh^{-1}\left[\frac{1-k_o}{1-k_e}\sqrt{\frac{k_e}{k_o}}\right] \tag{D.6}$$

where

$$k_{e,o} = \sqrt{1-\left(\frac{e^{\pi x}-2}{e^{\pi x}+2}\right)^4}, \quad \text{for} \quad 1 \le x \le \infty \tag{D.7}$$

$$k_{e,o} = \left(\frac{e^{\pi x}-2}{e^{\pi x}+2}\right)^2 \quad , \quad \text{for} \quad 0 \le x < 1 \tag{D.8}$$

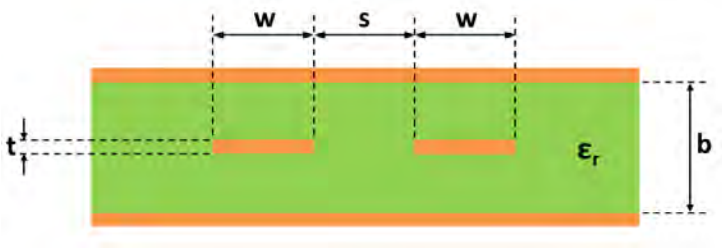

Figure D.1: Coupled striplines

$$x_e = \frac{Z_{0e}\sqrt{\epsilon_r}}{30\pi} \tag{D.9}$$

$$x_o = \frac{Z_{0o}\sqrt{\epsilon_r}}{30\pi} \tag{D.10}$$

To take into account non zero strip thickness for assumption that $(T/b) < 0.1$ and $(w/b) \geq 0.35$ the impedances for even and odd modes can be calculated with equations:

$$Z_{0e} = \frac{30\pi(b-T)}{\sqrt{\epsilon_r}\left(w + \frac{bC_f}{2\pi}A_e\right)} \tag{D.11}$$

$$Z_{0o} = \frac{30\pi(b-T)}{\sqrt{\epsilon_r}\left(w + \frac{bC_f}{2\pi}A_o\right)} \tag{D.12}$$

where

$$A_e = 1 + \frac{\ln(1+\tanh\theta)}{\ln 2} \tag{D.13}$$

$$A_o = 1 + \frac{\ln(1+\coth\theta)}{\ln 2} \tag{D.14}$$

$$\theta = \frac{\pi s}{2b} \tag{D.15}$$

$$C_f(T/b) = 2\ln\left(\frac{2b-T}{b-T}\right) - \frac{T}{b}\ln\left[\frac{T(2b-T)}{(b-T)^2}\right] \tag{D.16}$$

The losses in a pair of coupled striplines are composed of two elements: dielectric loss α_d and conductor loss α_c:

$$\alpha_d^e = \alpha_d^o = \frac{27.3\sqrt{\epsilon_r}\tan\delta}{\lambda_0} \quad [\text{dB/m}] \tag{D.17}$$

$$\alpha_c^e = \frac{0.0231 R_s \sqrt{\epsilon_r}}{30\pi(b-t)} \left\{ 60\pi + Z_{0e}\sqrt{\epsilon_r}\,[1- \right.$$

$$\left. -\frac{A_e}{\pi}\left(\ln\frac{2b-T}{b-T} + \frac{1}{2}\ln\frac{T(2b-T)}{(b-T)^2}\right) + C_f \frac{1+s/b}{4\ln 2}\frac{\mathrm{cosech}^2\theta}{1+\coth\theta}\right]\right\} [\mathrm{dB/m}] \tag{D.18}$$

$$\alpha_c^o = \frac{0.0231 R_s \sqrt{\epsilon_r}}{30\pi(b-t)} \left\{ 60\pi + Z_{0o}\sqrt{\epsilon_r}\,[1- \right.$$

$$\left. -\frac{A_o}{\pi}\left(\ln\frac{2b-T}{b-T} + \frac{1}{2}\ln\frac{T(2b-T)}{(b-T)^2}\right) + C_f \frac{1+s/b}{4\ln 2}\frac{\mathrm{cosech}^2\theta}{1+\coth\theta}\right]\right\} [\mathrm{dB/m}] \tag{D.19}$$